# Functional connectivity is preserved but reorganized across several anesthetic regimes

Guillaume Jean-Paul Claude Becq, Tarik Habet, Nora Collomb, Margaux Faucher, Chantal Delon-Martin, Véronique Coizet, Sophie Achard, Emmanuel L Barbier

NeuroImage 219 (2020) 116945

Contents lists available at ScienceDirect

NeuroImage

journal homepage: www.elsevier.com/locate/neuroimage

# Functional connectivity is preserved but reorganized across several anesthetic regimes

Guillaume J.-P. C. Becq [a,1,*], Tarik Habet [b], Nora Collomb [b,c], Margaux Faucher [a,b], Chantal Delon-Martin [b], Véronique Coizet [b], Sophie Achard [a,d,1], Emmanuel L. Barbier [b,c,1]

[a] Univ. Grenoble Alpes, CNRS, Gipsa-lab, F-38000, Grenoble, France
[b] Univ. Grenoble Alpes, Inserm, U1216, Grenoble Institut Neurosciences, GIN, F-38000, Grenoble, France
[c] Univ. Grenoble Alpes, Inserm, UMS017, CNRS, US3552, CHU Grenoble Alpes, IRMaGe, F-38000, Grenoble, France
[d] Univ. Grenoble Alpes, Inria, CNRS, Grenoble INP, LJK, 38000, Grenoble, France

ARTICLE INFO

*Keywords:*
Anesthesia
Cerebral blood flow (CBF)
Functional connectivity (FC)
Rat
Resting state functional magnetic resonance imaging (rs-fMRI)
Systemic variables

ABSTRACT

Under anesthesia, systemic variables and CBF are modified. How does this alter the connectivity measures obtained with rs-fMRI? To tackle this question, we explored the effect of four different anesthetics on Long Evans and Wistar rats with multimodal recordings of rs-fMRI, systemic variables and CBF. After multimodal signal processing, we show that the blood-oxygen-level-dependent (BOLD) variations and functional connectivity (FC) evaluated at low frequencies (0.031–0.25 Hz) do not depend on systemic variables and are preserved across a large interval of baseline CBF values. Based on these findings, we found that most brain areas remain functionally active under any anesthetics, i.e. connected to at least one other brain area, as shown by the connectivity graphs. In addition, we quantified the influence of nodes by a measure of functional connectivity strength to show the specific areas targeted by anesthetics and compare correlation values of edges at different levels. These measures enable us to highlight the specific network alterations induced by anesthetics. Altogether, this suggests that changes in connectivity could be evaluated under anesthesia, routinely used in the control of neurological injury.

## 1. Introduction

Resting state fMRI (rs-fMRI) is an elegant way to evaluate brain functional connectivity (FC) across species especially on Long Evans, Sprague Dawley or Wistar rats frequently used in the laboratory (Chen et al., 2011; Zhang et al., 2010; Jonckers et al., 2011; Grandjean et al., 2014; Bettinardi et al., 2015; Paasonen et al., 2018). While it is easy to ask a human subject to stay still, animals are either trained or anesthetized to limit motion artifacts (King et al., 2005; Zhang et al., 2010) (see also Appendix A). Training animals may however be too time consuming to be used in routine analysis and the stress from being restrained in a noisy environment could alter FC. The drawbacks of anesthesia are also well-known: it may change systemic variables (SV) such as temperature (Temp), heart rate (HR), respiration rate (RR) and at the brain level, it may alter neural activity, brain metabolism, baseline cerebral blood flow (CBF), and neurovascular coupling (Hendrich et al., 2001; Drew et al., 2011; Schroeter et al., 2014; Schlegel et al., 2015). A change in any of these variables may alter the FC mapped by rs-fMRI. This is why preclinical rs-fMRI data, obtained mostly under anesthesia, have been considered with some suspicion. This is related to two main questions: How can this apparent FC estimated from correlations between regional time series, reflect true brain connectivity? Is it possible, using standard methods, to evaluate whether brain connectivity is modified by the anesthetic? In order to map the impact of anesthesia on brain activity and metabolism, we want to evaluate potential biases on FC caused by confounding factors, SV and baseline CBF. Regarding SV, for a given data acquisition and processing protocol, changes in HR or RR may lead to change in the way the BOLD signal is contaminated by

*Abbreviations:* BOLD, blood-oxygen-level dependent; $<C>$, average correlation between signals of brain areas, or systemic signals; CBF, cerebral blood flow; FC, functional connectivity assessed by correlations between signals of brain areas in this study; FCS, functional connectivity strength, average correlation for one brain area; rs-fMRI, resting state functional magnetic resonance imaging; SV, systemic variables; HR, heart rate; RR, respiratory rate; Temp, temperature.

* Corresponding author.
*E-mail addresses:* guillaume.becq@grenoble-inp.fr (G.J.-P.C. Becq), sophie.achard@univ-grenoble-alpes.fr (S. Achard), emmanuel.barbier@univ-grenoble-alpes.fr (E.L. Barbier).

[1] These authors contributed equally to this work.

https://doi.org/10.1016/j.neuroimage.2020.116945
Received 11 September 2019; Received in revised form 21 April 2020; Accepted 11 May 2020
Available online 1 June 2020

physiological noise (Biswal et al., 1995; Kalthoff et al., 2011; King et al., 2005; Williams et al., 2010). Anesthesia might change the frequency of microvascular oscillations, thus requiring an adaptation of the frequency band at which FC should be observed (Franceschini et al., 2010; Grandjean et al., 2014; Thompson et al., 2014); The effect of anesthesia on the regulation of Temp is also complex and results generally in an important cooling of the animal (Cirone et al., 2004). Baseline CBF is expected to alter the amplitude of the BOLD response induced by neural activity (Cohen et al., 2002). It has also been reported that changes in CBF may lead to changes in FC. Petrinovic et al. (2016) acknowledged that an increase in baseline CBF could limit neurovascular reactivity and Jann et al. (2015) observed positive correlations in human subjects between regional CBF and FC in all resting brain networks. Furthermore, Jonckers et al. (2014) suggested that an increase in the variance of the BOLD signal could result in correlations that are less localized. A change in baseline CBF might thus modify the variance of the BOLD signal, the derived correlation coefficients, and thereby the apparent FC.

In this study, we explore large ranges of SV and baseline CBF using four different anesthetics and compare FC derived from long-run rs-fMRI recorded during 30 min with fast acquisition at 2 Hz. A processing pipeline to pick up the appropriate frequency bands to map FC is proposed. We show that FC is modified but preserved under anesthesia. Graphs of FC show different patterns and areas targeted by anesthetics.

## 2. Materials and methods

### 2.1. Animals

All experiments were approved by the local ethics committee and were performed in full compliance with the guidelines of the European community (EUVD 86/609/EEC) for the care and use of the laboratory animals, under permits from the French Ministry of Agriculture (number 380820 for EB and B3851610008 for experimental and animal care facilities). Experiments were conducted in the animal research facility of the Grenoble Institute of Neurosciences, a Specific Pathogen Free (SPF) housing facility, and comply with the ARRIVE guidelines (Kilkenny et al., 2010). Male rats were housed in enriched cages with 3 animals per cage and access to food and water ad libitum. Acquisitions dedicated to one anesthetic were conducted one after the other, with animals ascribed to the group upon arrival order, with no other randomization. Once all anesthetics were tested, about half the data was collected. A second run of acquisitions was then performed to obtain the full dataset with a population target of at least 6 fMRI recordings per anesthetized group.

### 2.2. Experimental protocol

Four anesthetics are evaluated on Long Evans rats: Etomidate (Eto-L), Isoflurane (Iso-L), Medetomidine (Med-L) and Urethane (Ure-L), with standard dosages. After an induction of anesthesia with a gaseous mixture of isoflurane, air and oxygen, the anesthetics of the four groups are the following during rs-fMRI: Isoflurane (Iso): the level of the isoflurane is set to 1%. - Etomidate (Eto): continuous intravenous infusion at 0.5 mg/kg/min. - Medetomidine (Med): bolus then continuous infusion at 0.05 mg/kg/h. - Urethane (Ure): bolus of 1.25 g/kg injected intraperitoneally. To evaluate whether animal strain biased this comparison, Isoflurane was also administered to Wistar rats (Iso-W). A group of dead rats (Dead) was also created by sacrificing 4 animals. Overall, six groups were evaluated. The number of animals per group is given in Table 1. Each Animal (n = 34) was included in only one anesthetic group and was recorded only one time, sacrificed if assigned to the Ure group or reused and sacrificed when randomly assigned to the Dead group (n = 4 with 1 Med-L, 2 Ure-L and 1 Iso-W). In this last group, recordings begin 1 h after sacrifice. Some recordings in CBF and SV were not available because of technical, measurements or artifacts problems and were excluded from the study (cf. Table 1).

During rs-fMRI sessions, systemic variables are monitored and recorded: from a pulse oximeter with a rat sensor clipped on the right posterior paw of the animal; a device measuring temperature with a rectal probe and respiration rate from a small pneumatic pillow sensor. Measurements from the two systems are sampled at 1 Hz. During the experiments a warm circulating water positioned below the animal is regulated to maintain the body temperature to a target level of 37 °C inside the MRI device. More technical and supplementary descriptions are given in Appendix B.

**Table 1**
Systemic variables and baseline CBF.

| | Eto-L | Iso-L | Iso-W | Med-L | Ure-L | Dead |
|---|---|---|---|---|---|---|
| N | 7 | 6 (*5*) | 7 | 7 | 7 (*5*) | 4 |
| W. | 191 ± 7 | 254 ± 55 | 316 ± 86 | 295 ± 23 | 289 ± 29 | 333 ± 51 |
| Temp. | 36 ± 2 | *38 ± 0* | 37 ± 1 | 37 ± 0 | *38 ± 1* | – |
| HR | 343 ± 51 | *444 ± 26* | 350 ± 34 | 219 ± 16 | *383 ± 83* | – |
| RR | 67 ± 11 | *67 ± 11* | 70 ± 3 | 73 ± 25 | *108 ± 18* | – |
| SpO2 | 99 ± 1 | *96 ± 5* | 99 ± 0 | 98 ± 1 | *75 ± 40* | – |
| N | 7 | 6 | 6 | 6 | 7 | – |
| CBF | 25 ± 6 | 67 ± 10 | 101 ± 27 | 19 ± 2 | 41 ± 9 | – |

Notations: N - number of rats, *italic indicates missing physiological measures for some individuals*; W. weight (g); Temp. - temperature ($^{o}$C); HR - heart rate in beats per minute (bpm), RR - respiration rate in cycles per minute (cpm); SpO2 - peripheral oxygen saturation (%) measured on the paw; CBF - baseline CBF (ml/100 g/min).

### 2.3. MRI acquisitions at 9.4 T and data processing

CBF is mapped using pseudo continuous arterial spin labeling (pCASL) following inter-pulse phase optimization as proposed in (Hirschler et al., 2018) with a spatial resolution 0.47 by 0.47 by 1.00 mm, gap 0.1 mm, 9 slices. rs-fMRI was performed with a single shot echo-planar imaging with TR / TE = 500 / 20 ms, the same spatial resolution as CBF, and 3600 repetitions (30 min). fMRI BOLD signals were first extracted on N = 51 brain areas from a home-made atlas based on published ones (Valdes Hernandez et al., 2011; Papp et al., 2014) after normalization of anatomical images and co-registration of fMRIs (Appendix B) and signal extraction for each area with weighted averaging on voxels (Appendix D). SV and BOLD signals are decomposed with wavelet transforms (Appendix B) with exclusion of samples contaminated by movements (Appendix E). Correlations are performed on these signals to evaluate FC (Appendix G).

### 2.4. Statistical analysis

To test for the difference of values between groups with unknown distributions, two-sided Wilcoxon rank-sum tests, with an appropriate hypothesis for paired samples or independence of samples are applied. The *p*-value is computed, and the hypothesis $H_0$ of the same mean of populations is accepted or rejected at different levels: no reject (−), reject at 5% (+), reject at 1% ( × ), reject at 0.1% (†). Pairwise comparisons are realized for different groups and a sequential notation is given for each group as compared to the other. A small circle (∘) is used to indicate the position of the current variable. Not available comparisons are indicated by small bullets (·). For example, a comparison of the mean of three populations G1, G2, G3, with: G1 and G2 significantly different at 1e-3; G2, G3 at 5e-2; and G1, G3 not significantly different, will be noted with the three sequences: (∘, †, -) for G1, (†, ∘, +) for G2, and (-, +, ∘) for G3. When linear regressions are estimated on bivariate samples, the null hypothesis that the slope of the regression is 0 is tested with a Wald test using *t*-values. Significant correlation coefficients are obtained by computing *p*-values based on ad-hoc hypothesis tests for correlations and wavelets (Whitcher et al., 2000; Achard et al., 2006) and adjusting for multiple corrections. (see also Appendix G).

### 2.5. Data availability

Data and codes are available at DOI 10.5281/zenodo.2452871.

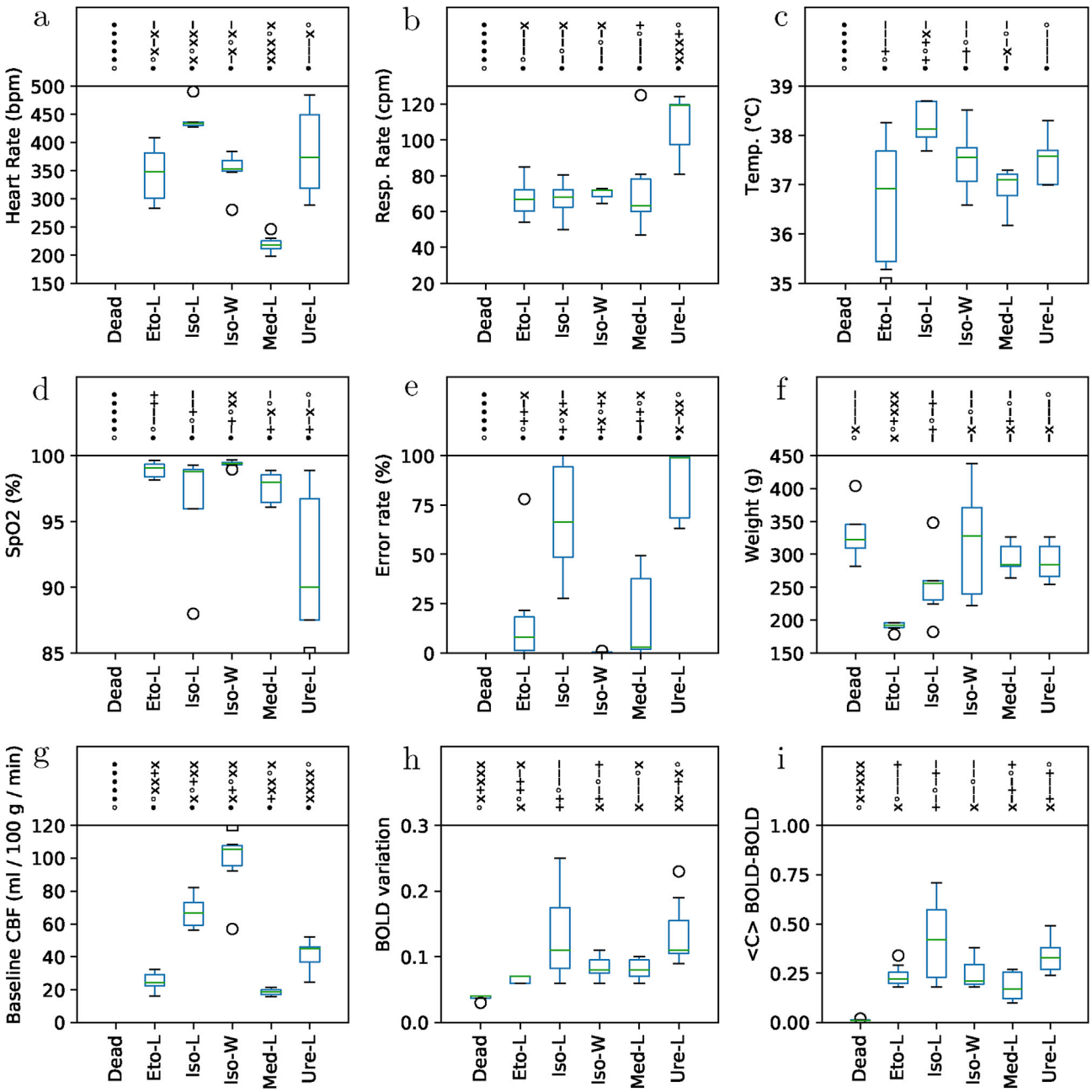


**Fig. 1.** Distributions of variables per group with box plots. The distributions are represented by boxes and whiskers: green bars indicate median values, upper and lower sides of the boxes indicate the 1st and 3rd quartiles, whisker bars are given for values under 1.5 times the interquartile limits and circle markers indicate outlier values outside this interval. Square markers indicate outlier values out of the plot range. Above each whisker plot, the *p*-value of the test of comparison of distributions with the other groups (unpaired Wilcoxon tests). Markers indicate the level of significance of the *p*-values: - > 0.05 > + > 0.01 > × > 0.001 > †. The position of the reference group is indicated by ◦ and unavailable comparison by •.

## 3. Results

### 3.1. Effects of anesthesia on SV and baseline CBF

Number of animals per group, means (m.) and standard deviations (sd.) of SV measured during the fMRI protocol are given in Table 1 and distributions of values with box plots are given in Fig. 1.

SV have usual ranges observed during anesthesia on rats, with high HR for Iso-L, unstable HR for Eto-L and Ure-L (sd. > 15% m.), high RR for Ure-L, and difficulty to measure peripheral oxygen saturation as a consequence of the cooling of peripheral limbs for Ure-L (missing values and one individual with low values, see Fig. 1d). Homogeneous values of variables are observed within groups (scatter plots of pairs of SV given in Fig. I.20, Fig. I.21 and Fig. I.22). There is a relationship between HR and Temp ($R = 0.56$, $p < 0.01$). Baseline CBF is significantly different between groups (Fig. 1g). The highest baseline CBF is observed under isoflurane (Iso-L: 67, Iso-W: 101 ml/100 g/min), with an influence of the rat strain. The lowest baseline CBF is obtained for Med-L (19 ml/100 g/min), in line with previous reports (Liu et al., 2012; Ganjoo et al., 1998; Weber et al., 2006). Relationships between baseline CBF and SV are only significant for HR ($R = 0.56$, Fig. I.20) and Temp ($R = 0.49$, Fig. I.22). Overall, anesthetics change SV and baseline CBF values with induced steady states for each group.

### 3.2. SV, BOLD signals and FC across frequency bands

fMRI BOLD signals were first extracted on $N = 51$ brain areas from a

home-made atlas based on published ones (Valdes Hernandez et al., 2011; Papp et al., 2014) (see materials and methods and Appendix C for details). As BOLD signals and SV were simultaneously recorded, we evaluated the relationship between BOLD signals with themselves (BOLD-BOLD) and with SV (BOLD-HR, BOLD-RR and BOLD-Temp) for different frequency bands after motion filtering (see materials and methods Appendix E for details). Frequency bands are obtained using dyadic wavelet transforms. The decomposition is done on rs-fMRI raw signals (raw) to yield signals corresponding to detail coefficients at different scales (cD1 - cD7) and one signal corresponding to approximation coefficients (cA7). The frequency bands are, in Hz: cA7 $<$ 0.008 $<$ cD7 $<$ 0.016 $<$ cD6 $<$ 0.031 $<$ cD5 $<$ 0.063 $<$ cD4 $<$ 0.125 $<$ cD3 $<$ 0.25 $<$ cD2 $<$ 0.5 $<$ cD1 $<$ 1. Let $C_{ij}$ be the BOLD-BOLD correlation coefficient between signal from area $i$ and signal from area $j$. The functional connectivity strength (FCS)[2] for node $i$ is defined as $FCS_i = 1/(N-1)\sum_{j,j\neq i}C_{ij}$. The mean FCS is then defined as $\langle C\rangle$ BOLD $-$ BOLD $= 1/N\sum_i FCS_i$. For SV signals, we defined $\langle C\rangle$ BOLD $-$SV $= 1/N\sum_j C_{SVj}$ where $C_{SVj}$ is the BOLD-SV correlation between SV signal and signal from area $j$. Each of these quantities are computed for each frequency band using the corresponding wavelet coefficients.

Fig. 2a represents the distributions of $\langle C\rangle$ BOLD-BOLD in function of frequency bands over all animals. $\langle C\rangle$ BOLD-BOLD increases with the frequency bands with significant differences from cD1 to cD3 with other scales, and median close to 0 for cD1 - cD2. Significant BOLD-BOLD correlation coefficients are obtained by computing $p$-values based on ad-hoc hypothesis tests for correlations and wavelets (Whitcher et al., 2000; Achard et al., 2006) and adjusting for multiple corrections (see Appendix G for details). Fig. 2b and c shows a maximum of significant correlations for the frequency band cD4, where mean $\pm$ standard error of the mean (M $\pm$ SEM) are represented for each anesthetic in Fig. 2c. To validate our method, a group of dead rats (Dead) was created by sacrificing 4 animals. Almost no significant BOLD-BOLD correlations are obtained on this group. Fig. 2d–f shows that the variance of $\langle C\rangle$ BOLD-HR, $\langle C\rangle$ BOLD-RR and $\langle C\rangle$ BOLD-Temp increases with the observed frequency band. Interestingly, as frequency band increases, the median $\langle C\rangle$ BOLD-BOLD increases faster than the variance of $\langle C\rangle$ BOLD-SV. This suggests that there is a frequency band for which the ratio between the median $\langle C\rangle$ BOLD-BOLD and the variance of $\langle C\rangle$ BOLD-SV is optimal. This band corresponds to a maximum in edges detection based on signal and not noise, as confirmed by the number of significant BOLD-BOLD correlation coefficients per animal given in Fig. 2c cD4 seems a good compromise for all groups, even though for some anesthetics the same number of significant correlations can be found for cD3 to cD5 (0.031–0.25 Hz). The cD4 band (0.063–0.125 Hz) is thus retained to compute BOLD-BOLD correlations. In the remainder of this paper, BOLD signal corresponds to the BOLD signal filtered in this band.

### 3.3. BOLD variations and FCS are independent of baseline CBF

To evaluate the impact of baseline CBF on BOLD signals, we computed the standard deviation of the BOLD signal for each brain area, denoted as BOLD variation. Fig. 3a shows the BOLD variation as a function of baseline CBF, binned per CBF intervals of 10 ml/100 g/min and averaged across rats per group, with values given in M $\pm$ SEM. Despite the broad range of baseline CBF values, almost flat curves are observed for each anesthetic over a large range of CBF values. Similar results are obtained for different frequency bands (see Fig. I.31). Fig. 3b shows similar almost flat curves obtained for FCS as a function of baseline CBF. This indicates that average values of BOLD variation and FCS do not depend on the average baseline CBF values. There is no significant relationship between baseline CBF and BOLD variation or $\langle C\rangle$ BOLD-BOLD (Fig. I.26), but there is a significant relationship between BOLD variation and $\langle C\rangle$ BOLD-BOLD ($R = 0.87$, $p < 0.001$) (Fig. I.27). Fig. 3c shows, per group, a coronal view of baseline CBF, BOLD variation and FCS in the brain. It further suggests that CBF, BOLD variation and FCS are not tightly linked. For example, even if CBF is high for Iso-W, BOLD variation is low. For high baseline CBF values observed in the Iso groups, the measures in BOLD are high for Iso-L and medium for Iso-W. Eto-L and Med-L produces similar patterns, with low values for all three variables. Altogether, the FCS patterns seem similar across all anesthetics, not sensitive to either CBF or BOLD variation.

### 3.4. Anesthetics target specific brain areas and reshape distribution of connections

For each group of rats, average correlation matrices are computed. Based on our results in Fig. 2c, edges not significantly different to zero correlations are removed. FCS per group and area are presented in Fig. 4a with FCS computed here using $FCS_i = \frac{1}{N_i}\sum_{j\in S_i} C_{ij}$ with $S_i$ the set of significant correlations for area $i$ and $N_i$ the number of elements in $S_i$. This approach is validated on the group of dead rats where no connections remain. When computing the average correlation matrices for the other groups of rats, 9 areas only are not significantly different from noise. This means that at most 9 (/51) brain areas, or 6 (/26) by grouping bilateral areas can not be differentiated from random signals, whatever the anesthetic. Hence, we can not conclude on their specific connections with other areas. On average, sensory (S1, S1BF, S2), motor (M1, M2) and cingulate cortex (ACC) areas have the highest correlation values. This is emphasized by Fig. 4b where areas are ranked from the most connected area to the least one. Depending on the anesthetic, some areas are more connected in some groups (e.g. V1 in Iso-L, Ins in Iso-W, Th in Eto-L) or less connected (e.g. Acc in Ure-L, S2 and AU r in Eto-L). Asymmetries between left and right areas may also be observed (e.g. Ins and AU in Eto-L, M2 in Iso-L and Ure-L). These observations should be mitigated by the fact that FCS values show a moderate but significant relationship with the area location in the MRI device ($R = -0.68$, $p < 0.001$), and, at a lesser level, with the area size ($R = 0.56$, $p < 0.01$) (Appendix H), with low values of FCS obtained for small and far from the coil areas, such as TeA. After verifying that correlations did not originate from spurious neighboring signal contamination by evaluating the presence of significant long-range correlations in each group (Fig. H.16), graphs were constructed per group to highlight local differences in connectivity.

Fig. 5 displays the thresholded correlations with a density[3] $\rho = 0.1$. Nodes communities detected by clustering are given in color (details in Appendix B). The graphs of anesthetized groups are structured with the anterior cingulate cortex (ACC) taking a central place in connectivity. Among the acquired nodes, nodes with low FCS seem less connected for some groups (H, BF, BG, APir, pag). There is also an obvious loss of the inter-hemispheric connections in the Ure-L group and a loss of the cortical-subcortical connections in the Med-L group. This is further confirmed by individual graphs and other representations proposed in Fig. I.32 to Fig. I.37 and Fig. I.38.

Finally, we summarized the impact of anesthetics from graphs of Fig. 5 by representing the ratio of connections between ACC, cortical (c), subcortical (s), interhemispheric (inter) or intrahemispheric (intra) areas. Fig. 6 shows the spatial reorganization of the 10% strongest correlations, given by graphs at density $\rho = 0.1$. We observe low ACC FC for Ure-L, very low inter FC for Ure-L, low inter FC for Eto-L, and low c-s FC for Iso-L, Med-L and Iso-W (see Appendix H for values and comparison with other densities).

In summary, depending on the anesthetic and the animal strain, 25–60% of the total possible connections are significant with at least 80% of areas connected to at least one other area, with reordering of the strongest connections.

[2] This definition is related to the one proposed in (Liang et al., 2013a) or the normalized version of vertex (node) strength or weighted degree proposed in (Barrat et al., 2004; Rubinov and Sporns, 2010).

[3] The number of retained edges over the number of all possible edges.

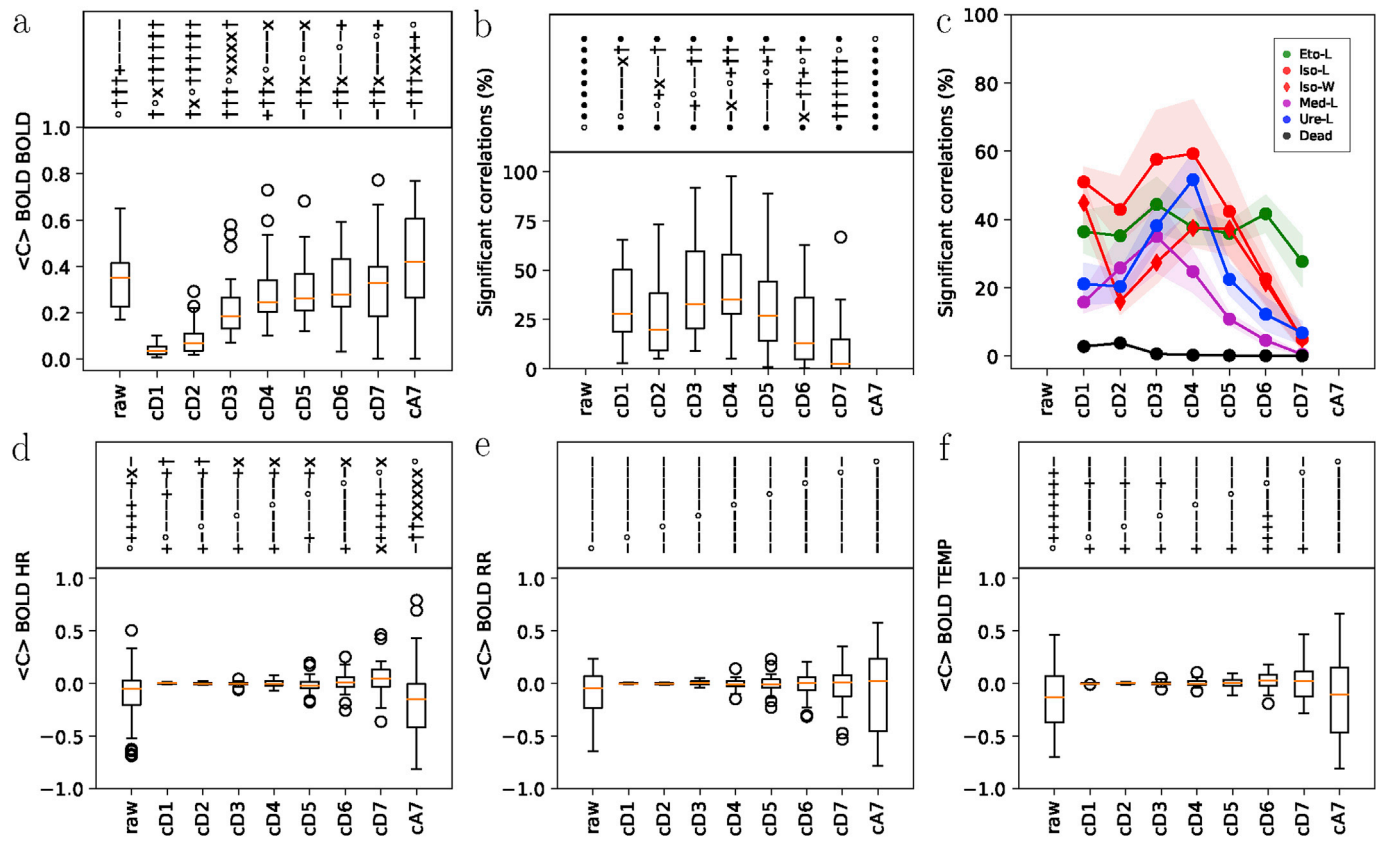


**Fig. 2.** Distributions of correlations by frequency bands. a) Whisker plots of ⟨*C*⟩ BOLD-BOLD, the mean functional connectivity between BOLD signal pairs at a given frequency band for all 51 brain areas, averaged across all animals, as a function of frequency band. b-c) Global and per group distributions of the percentage of significant correlations per frequency band. d-f) Whiskers plots for ⟨*C*⟩ BOLD-HR ⟨*C*⟩ BOLD-RR and ⟨*C*⟩ BOLD-Temp, the average correlation between heart rate (HR), respiratory rate (RR) and temperature (Temp.) signal, and BOLD signals, at a given frequency band.

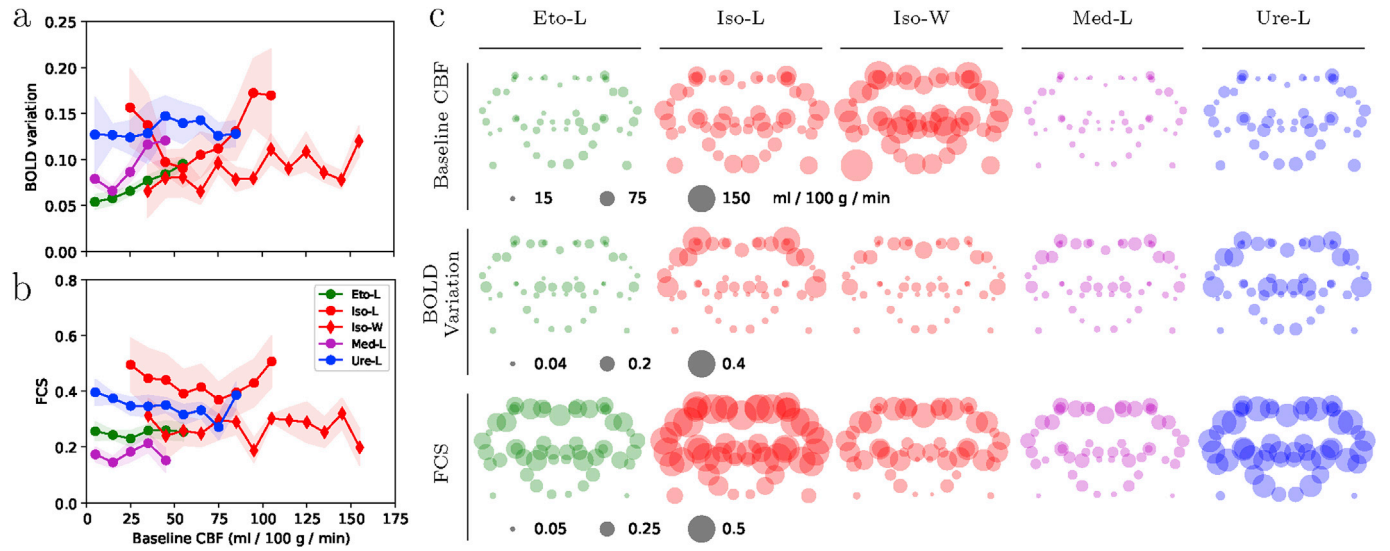


**Fig. 3.** Relationships between baseline CBF, BOLD variation and FCS. a) Average values of BOLD variation per CBF bin and per group with at least 4 animals. b) Functional connectivity strength (FCS) per CBF bin and per group with at least 4 animals. c) Comparison per group on each node for baseline CBF, BOLD variation and FCS. Each area is represented by a node located at its center of gravity on a coronal projection. Node diameter is related to parameter value.

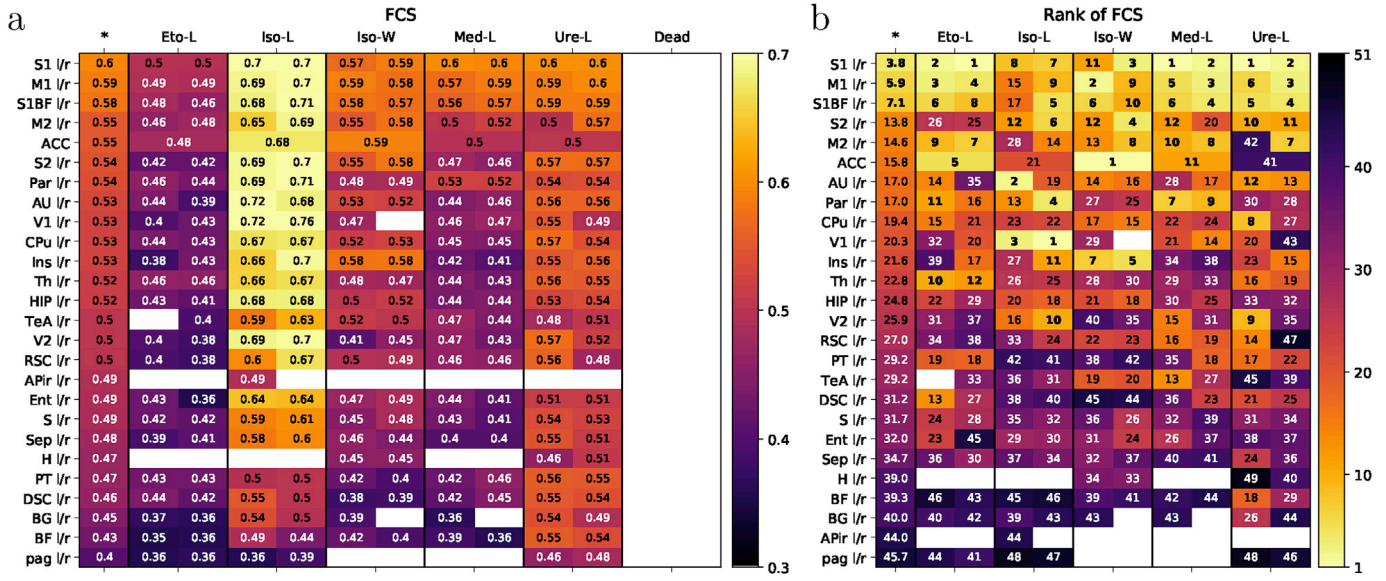


**Fig. 4.** Graph measures and representations per group of average matrices. Average was performed on significant correlations at a symmetrical level $\alpha = 5\%$ (Bonferroni corrections $p =$ 2e-5) and if present in a minimum of 4 animals per group. (a) FCS. Each area is represented by two columns (left and right hemispheres), except for ACC which is central and for column * which is the average of anesthetized groups. Areas are sorted from this column. Unavailable FCS from areas with no detected edges are not plotted (white). (b) FCS rank per group, sorted from highest to lowest. A rank of 1 indicates that the area has the highest FCS in its group. Areas showing the lowest ranks (first quartile) are in bold. The first column * is the average of anesthetized groups. Areas are sorted from this column. Notations: l: left, r: right, ACC: anterior cingulate cortex, APir: amygdalopiriform transition area, AU: auditory cortex, BF: basal forebrain region, BG: basal ganglia, CPu: caudate-putamen striatum, DSC: superior colliculus, Ent: entorhinal area, Ins: insular cortex H: hypothalamic region, HIP: hippocampus, M1: primary motor cortex, M2: supplementary motor cortex, pag: periaqueductal gray, Par: parietal association cortex, PT: pretectal region, RSC: retrosplenial cortex, S: subiculum S1: somatosensory 1, S1BF: somatosensory 1 barrel field, S2: somatosensory 2, Sep: septal region, TeA: temporal cortex association area, Th: thalamus, V1: primary visual cortex, V2: secondary visual cortex.

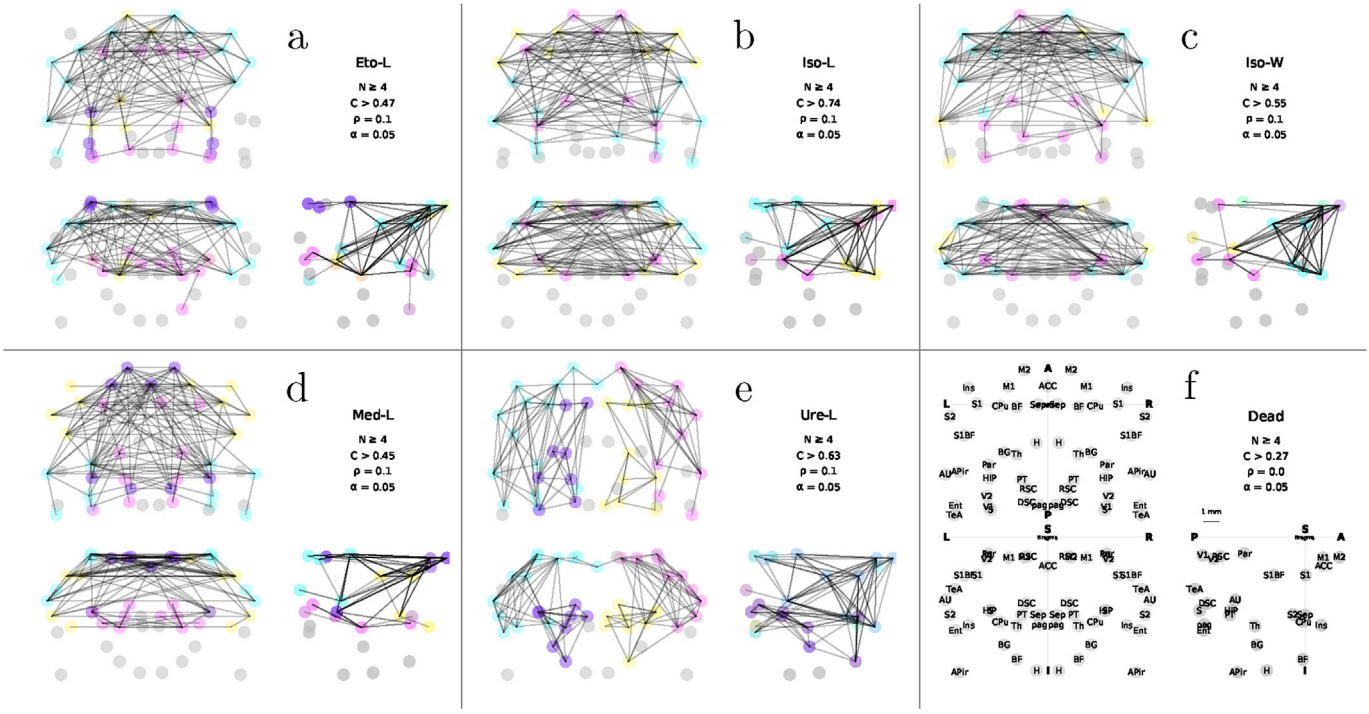


**Fig. 5.** Graph representations of average matrices per group. Average was performed as in Fig. 4. (a)–(f) Graphs based on the average correlation matrices obtained with the frequency band cD4 for all groups. The 127 most correlated values (density $\rho = 0.1$) are plotted. Gray nodes represent unconnected nodes and nodes with the same arbitrary color belong to the same community. For each group, the number of animals, the lowest correlation value used in the graph, and the correlation significance threshold are mentioned. (f) The Dead group shows no significant connections. Notations same as Fig. 4 with L–R: left-right axis, A–P: antero-posterior axis, I–S: inferior-superior axis.

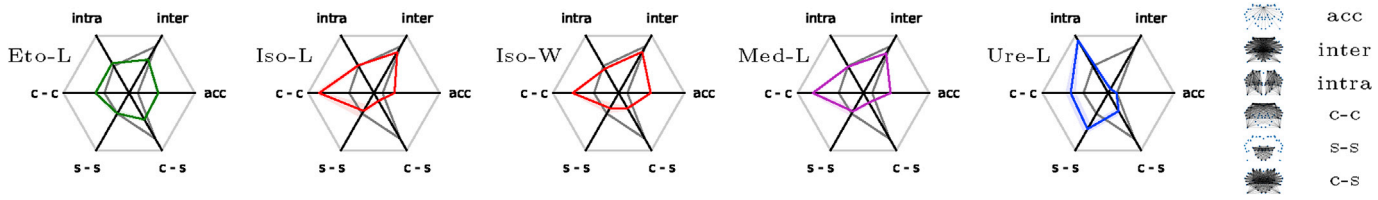


**Fig. 6.** Radar representations of average matrices per group. Average was performed as in Fig. 4. Radar plots represent the distributions of connections for the graphs presented in Fig. 5, obtained at a density $\rho = 0.1$. Gray curve represents percentages for the fully connected graph. Notations: acc: anterior cingulate cortex, inter: interhemispheric, intra: intrahemispheric, c: cortical, s: subcortical.

## 4. Discussion

### 4.1. Summary of findings

After observing that SV and CBF under anesthesia were stable, we introduced an approach based on wavelet decomposition to identify the optimal frequency bands to analyse FC and the number of significant correlations between areas. This approach limits the interaction with SV and improves the signal to noise ratio for the detection of significant graph edges. Using this method, and data including baseline CBF and rs-fMRI acquired in rats under several anesthetic conditions, we observed that, in the low frequency band 0.06–0.12 Hz, BOLD variation and FCS are independent of baseline CBF. Overall, the vast majority of brain areas are connected together with anesthetic dependent connectivity patterns.

### 4.2. Impact of anesthetics on SV, choice of BOLD frequency bands and FC

SV values reported in this study are inline with previous reports using comparable anesthetics and preparations (De Wildt et al., 1983; Sinclair, 2003; Jonckers et al., 2011; Masamoto and Kanno, 2012; Grandjean et al., 2014). Fig. 2d–f indicate that, whatever the baseline SV, fluctuations of SV in some frequency bands (cD3 - cD5: 0.031–0.25 Hz) do not correlate with spontaneous BOLD signals during the 30 min acquisition. We also evaluated whether the SV averaged across the acquisition duration and the BOLD variation averaged in the same way were correlated when considering all animals. With this approach, correlations were observed between average SV and average BOLD variations (Fig. 3; e.g. Temp. vs BOLD variation), possibly resulting from the increased variability of SV fluctuations at frequencies below 0.031 Hz. Altogether, despite the broad range of SV conditions produced by the use of different anesthetics, SV fluctuations did not contaminate BOLD signal in the 0.031–0.25 Hz band for a 30 min acquisition.

Modifications on signals may also be related to movements of the animals. Since animals were restrained with teeth and ear bars, the contamination of the BOLD signal is less probable than in human studies. Nevertheless, motions can occur and a classical scrubbing method with boxcar filtering (Yan et al., 2013) has been applied, taking into account HRF and wavelet support at different scales (see Appendix E). Alternative methods to filter out SV and movements exist and are recommended by other studies (Grandjean et al., 2020), but they lead to complex modifications of signal that may prevent a quantitative analysis of correlation coefficients and lead to controversial results, as for example with global signal regression (GSR) (Murphy and Fox, 2017). Transformations of correlations are also complex to interpret when working with non-Gaussian processes and lead to distributions of correlations that are difficult to compare (Bettinardi et al., 2015; D'Souza et al., 2014; Gass et al., 2014; Liska et al., 2015; Paasonen et al., 2018). Without any transformations, the distributions of correlations (Fig. I.29) are comparable with the ones presented in (Sforazzini et al., 2014; Liu et al., 2013a; Oh et al., 2014) and show influences of anesthetics on $\langle C \rangle$. It would however be of interest to further investigate and compare these different transformations.

The study of the number of significant correlations as a function of the frequency band seems a useful step to optimize and validate the FC processing pipeline. We advocate the use of both dead rats (Grandjean et al., 2014) and random simulations (Achard et al., 2006; Zalesky et al., 2012). Indeed, empty graphs may be obtained when the signal to noise ratio is too low (Fig. 5), and thereby enhance contrast for specific communities and networks. The selected frequency band (cD4: 0.062–0.125 Hz), determined by experimental constraints and mathematical framework, was narrower than previous experimental reports but included, like most reports, frequencies below 0.1 Hz (see Appendix F). Bandwidths could be further adjusted for example by merging some of them, also based on observations of the power spectrum of signals (Appendix F) as given in (Grandjean et al., 2014; Liu et al., 2013a; Thompson et al., 2014). Since the velocity of the hemodynamic response depends on baseline CBF (Cohen et al., 2002), the optimal frequency band could depend on the type of anesthetic or on the animal strain (Franceschini et al., 2010; Grandjean et al., 2014; Thompson et al., 2014). Since no correlations between baseline CBF and BOLD variations in the cD4 band were observed, our data do not demonstrate this point, in line with a previous report showing that spontaneous sinusoidal oscillations may exist over a range of anesthesia depths (Golanov et al., 1994). This is also inline with BOLD variations caused by arteriole vasomotor variations (Mateo et al., 2017) under the control of locally regulated vasoactive substances (Akata, 2007; Devor et al., 2007). The method we propose could be adjusted to explore narrower frequency bands and thereby smaller change in hemodynamic response function, based on longer rs-fMRI acquisitions.

### 4.3. Impact of anesthetics on baseline CBF, BOLD variations, and $<C>$ BOLD-BOLD

The choice of anesthetic and of animal strain changed the baseline CBF, a parameter correlated to mean HR and mean Temp (Fig. I.30). Baseline CBF was however independent of BOLD variations and of FCS (Fig. 3). This is in line with (Maximilian et al., 1980) but seems in contradiction with previous reports, which demonstrated that an increase in baseline CBF decreases the BOLD signal amplitude, comparable to the BOLD variation in our study (Cohen et al., 2002). The difference with (Cohen et al., 2002) is that a change is observed in one given brain area, whereas all brain areas with the same CBF are averaged in our study. Mean $\langle C \rangle$ BOLD-BOLD were however dependent on HR and Temp, suggesting that this parameter is not fully independent of baseline physiology. Mean arterial pressure could also modulate the BOLD variation (Hudetz et al., 1992) but was not evaluated in this study. Altogether, extreme care should be taken to maintain normal and stable physiological conditions while performing rs-fMRI.

### 4.4. Impact of anesthetics on brain connectivity

Our proposed pipeline using anesthetics extracts connectivity matrices of brain rats with 25–60% significant connections (Fig. 2c), containing 42/51 (80%) areas significantly connected with at least one other area (Fig. 4). This range of 25%–60% of significant connections is consistent with density observations in the macaque monkey (up to 66%, 29 areas), using a retrograde tracer analysis (Markov et al., 2013), and in mice (up to 36%, 213 areas), using an anterograde tracer (Oh et al.,

2014). By acquiring good quality data and using robust methods, it seems therefore possible to observe fMRI graphs in which most brain areas remain functionally active, even when the rats are anesthetized. The few apparent not significantly connected areas (H, BF, BG, APir, pag) are located far from the receive surface coil (decrease of FCS in function of distances from Bregma given in Appendix H) and close to large vessels or cerebro-spinal fluid, two sources of noise. The lower signal to noise ratios for these areas could contribute to the absence of significant FCS in some areas such as TeA or APir. The position of the left and right areas near the ears with potential distortions (see Fig. B.8) can also add noise in these areas, but no correlations were observed between FCS and medio-lateral locations of areas (Appendix H). The graph approach provides a global view of the FC and characteristic patterns, with differences in the global organization of the brain connectivity. This is in line with previous studies (Grandjean et al., 2014; Hutchison et al., 2014; Jonckers et al., 2011, 2014; Paasonen et al., 2018; Sforazzini et al., 2014) where the authors used seed based analysis or independent component analysis (ICA). In this work, the impact of anesthetics is visible at the regional level with communities (Fig. 5) partially related to networks such as the default mode network (DMN) or the resting-state network (RSN) (Lu et al., 2012; Sforazzini et al., 2014; Grandjean et al., 2020). Compared to ICA approaches, which highlight the most orthogonal networks, the graph approach used in this study rather seeks for all potential connections (Ribeiro de Paula et al., 2017; Lv et al., 2018). Seed Based Analysis (SBA) also promotes a limited number of connections due to the limited number of seeds. Graphs may be seen as an SBA approach in which every region is a seed, with FCS giving the strength of the seed (Fig. 4). In contrast to graph analysis, ICA or SBA approaches usually distinguish segregated networks. Our results may not appear in agreement with these approaches, and a study using the same data but with different analysis methods is required to conclude whether they lead to similar or complementary conclusions concerning biological processes. The impact of Urethane and Isoflurane on M1, S1 and CPu (Jonckers et al., 2014) is shown at the regional level, but also at an intermediate level where balance of connections between cortico-cortical areas, cortico-subcortical areas, or intrahemispheric and interhemispheric areas are modified depending on anesthetics. The study of the effects of anesthesia on bilateral connectivities in rodents is an active field of research (Nasrallah et al., 2014), with Medetomidine, which may reduce thalamocortical transmission (Sinclair, 2003) (Fig. 6, Table H.3 also observed for Isoflurane in this study), but also bilateral connectivity (Jonckers et al., 2011; Nasrallah et al., 2014) (not observed here), and Urethane, which may decrease the strength of bilateral connections (Grandjean et al., 2014; Jonckers et al., 2014) (Fig. 6, Table H.3 in this study) or even induce fluctuating connectivity states with periods on the order of a few minutes to tens of minutes as reported in (Zhurakovskaya et al., 2019). The influence of anesthetic dose, rodent strain, animal state and details of the analysis method on bilateral connectivity under anesthesia requires further investigation. Concerning these observations, our results are consistent with literature. However, the different communities extracted with our method are not easily comparable with those obtained with commonly used GSR or ICA. One could expect that our method would show communities comparable to previously reported functional networks such as DMN (including ACC, RSC, and TeA[4]) with stability observed across different anesthetics regimes (Grandjean et al., 2020). Here, we observe that there might be connections between ICA-reported networks. For example, ACC is part of the DMN. It is also known to be involved in several processes such as the balanced between behaviors, autonomous functions or nociception, and known to have a lot of connections with other areas including sensory and motor areas (Vogt and Miller, 1983; Paus, 2001; Vogt, 2005). ACC, as defined in our study, can therefore be involved in different networks. Some comparisons between graph-based analyses and the effect of GSR and ICA are given in (Liu et al., 2013a), but it would be of interest to perform an entire study on the same dataset to compare and enhance the complementarities of the different methods.

### 4.5. Main limitations

To overcome the limited brain coverage (10 mm that excluded the cerebellum and the olfactory bulb), simultaneous multislice MRI should be developed at the preclinical level. The number of animals per group is limited (n = 6 or 7) and some groups exhibit heterogeneity. Main findings are however related to all live animals (n = 34) and the impact of physiological variations was carefully analysed. The anesthetic dose in this study were standard ones but not optimal ones related to anesthesia depth, leading to comparisons between drugs that should be mitigated. It is indeed expected that the anesthetic dose also leads to different functional connectivity patterns, as observed with isoflurane (Williams et al., 2010; Jonckers et al., 2011, 2014; Liu et al., 2013a), and should be evaluated in other studies in association to the search of an optimal dose. Besides, further studies are required to account for the contribution of the metabolic effects such as oxygen and glucose consumption and electrical activity (Hoffman et al., 1991; Sloan et al., 2010; Masamoto and Kanno, 2012). Lastly, nothing can be interpreted from the remaining 20% of the areas that are not significantly connected.

## 5. Conclusions

In summary, this study introduces a methodological approach to evaluate the influence of different anesthetics on rats during anesthesia. Using a rigorous mathematical framework based on wavelets-based spectral filtering, we have shown that systemic variables and the baseline CBF, in the range evaluated in this study, have no influence on the slow fluctuations of BOLD signals and on FC. Moreover, most brain areas remained functionally active under the anesthetics used in this study with density of the graphs in the range between 25% and 60%. This demonstrated, we have proposed measures that highlight the influence of the different anesthetics on FC, at the level of brain areas or between them. Future work could use the proposed methodological framework with increased populations, adjusted anesthetics concentrations or refined spectral bands to better tune the effects of anesthetics on the whole brain, on functional connectivities or on specific target areas.

## Funding

The MRI facility IRMaGe is partly funded by the French program *Investissement d'Avenir* run by the French National Research Agency, grant *Infrastructure d'avenir en Biologie Santé* [ANR-11-INBS-0006]. This project was partly funded by NeuroCoG IDEX UGA in the framework of the *Investissements d'avenir* program [ANR-15-IDEX-02].

## Declaration of competing interest

The authors have no conflict of interests.

## CRediT authorship contribution statement

**Guillaume J.-P. C. Becq:** Conceptualization, Methodology, Software, Validation, Formal analysis, Investigation, Data curation, Writing - original draft, Writing - review & editing, Visualization. **Tarik Habet:** Data curation, Investigation. **Nora Collomb:** Investigation, Resources. **Margaux Faucher:** Software, Investigation. **Chantal Delon-Martin:** Formal analysis. **Véronique Coizet:** Methodology, Formal analysis, Investigation. **Sophie Achard:** Conceptualization, Methodology, Software, Validation, Formal analysis, Writing - original draft, Writing - review & editing, Visualization, Supervision, Project administration, Funding acquisition. **Emmanuel L. Barbier:** Conceptualization,

[4] with prefrontal cortex area (PFC) not included in the study because this area was not available in several recordings

Methodology, Software, Validation, Formal analysis, Investigation, Resources, Writing - original draft, Writing - review & editing, Visualization, Supervision, Project administration, Funding acquisition.

**Acknowledgments**

The authors want to thank the reviewers for their detailed comments and suggestions that have improved the presentation of this work. The authors are very grateful to Sarah E. Morgan for her careful and meticulous reading of the paper.

## Appendix A. Anesthetics used in rodents

A list of the anesthetics evaluated on rodents is given here with associated references:

- α-chloralose (Baek et al., 2016; Franceschini et al., 2010; Guilfoyle et al., 2013; Jonckers et al., 2014; Lu et al., 2007; Paasonen et al., 2018; Shim et al., 2012; Williams et al., 2010),
- diazepam (benzodiazepine) (Ogawa et al., 1990),
- etomidate (Petrinovic et al., 2016),
- fentanyl (Hendrich et al., 2001),
- halogeneous derivates (Ciobanu et al., 2012; Chan et al., 2014; Franceschini et al., 2010; Grandjean et al., 2014; Hendrich et al., 2001; Hoffman et al., 1991; Jonckers et al., 2014; Kalthoff et al., 2013; Liang et al., 2013b, 2015; Liska et al., 2015; Liu et al., 2013a) (Magnuson et al., 2010, 2014; Masamoto et al., 2009; Ogawa et al., 1990; Paasonen et al., 2018; Pan et al., 2013; Sforazzini et al., 2014; Sicard et al., 2003; Sloan et al., 2010; Smith et al., 2017; Stafford et al., 2014; Thompson et al., 2014; Williams et al., 2010),
- ketamine (Bettinardi et al., 2015; Ciobanu et al., 2012; Gass et al., 2014),
- medetomidine (Bettinardi et al., 2015; Ciobanu et al., 2012; D'Souza et al., 2014; Gass et al., 2014; Grandjean et al., 2014; Jonckers et al., 2011; Kalthoff et al., 2011; Kalthoff et al., 2013; Lu et al., 2012; Magnuson et al., 2014; Mechling et al., 2014; Nasrallah et al., 2014; Paasonen et al., 2018; Pan et al., 2013; Pawela et al., 2008; Pawela et al., 2009; Schwarz et al., 2013; Thompson et al., 2014; Williams et al., 2010; Zerbi et al., 2015),
- MPEP (mGluR5 antagonist 2-methyl-6-(phenylethynyl)-pyridine (Sloan et al., 2010),
- pentobarbital (Hendrich et al., 2001; Otte et al., 2014),
- propofol (Grandjean et al., 2014; Liu et al., 2013b; Paasonen et al., 2018),
- urethane (carbamate) (Grandjean et al., 2014; Jonckers et al., 2014; Ogawa et al., 1990; Paasonen et al., 2018).

Animals can also received curare (pancuronium bromide) infusion (Liu et al., 2013a, 2013b; Pawela et al., 2008; Shim et al., 2012; Zerbi et al., 2015) to relax muscle and avoid movements or paralyzing agent (gallamine triethiodide) (Sforazzini et al., 2014).

Elements on what is known about the effects on brain functions, neurons interactions, ionic channels affinities and physiological interactions can be found for example in (Akata, 2007).

## Appendix B. Supplementary Materials

### *Appendix B.1. Experimental protocol*

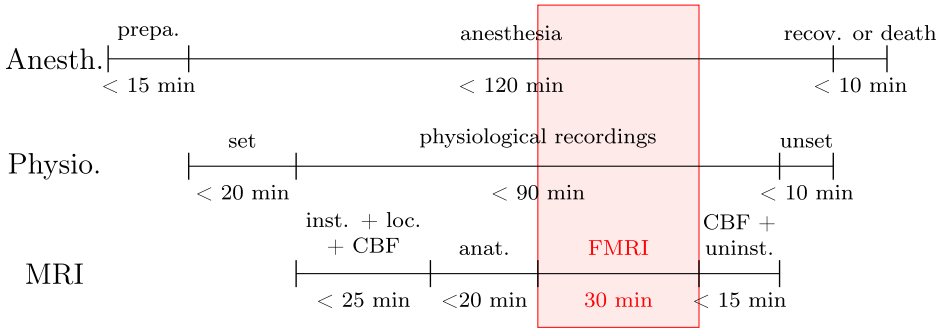


**Fig. B.7.** Experimental protocol. Notations: Anesthesia (Anesth.), SV (Physio.), Magnetic resonance imaging (MRI), preparation of the animal (prepa.), installation of the animal in the scanner (inst.), position verification with a localizer sequence (loc.), cerebral blood flow sequence (CBF), anatomical sequence (anat.), rs-fMRI sequence (FMRI), uninstallation of the animal (uninst.), recovery or death of the animal (recov. or death).

A scheme of the experimental setup used to record data from anesthetized rats is proposed Fig. B.7 and can be summarized as follows. For the anesthesia, a preparation of the animal is realized in an induction room. Anesthesia generally lasted less than 2 h. At the end of the protocol the animal is kept alive for another study or euthanized, if in the Ure group or randomly assigned to the Dead group. For the systemic variables, also denoted SV, sensors are set and unset before and after the recordings. For magnetic resonance imaging, the animal is installed in the scanner and positions are verified with localizer sequences. A perfusion sequence (CBF) and an anatomical sequence are acquired before the fMRI sequence which lasts 30 min. Then, another perfusion sequence is acquired, followed by the uninstallation of the animal.

*Appendix B.2. Anesthesia*

At the beginning of the experiment, animals receive a gaseous mixture, composed of isoflurane and a mixture of 80% air and 20% oxygen, inhaled through a funnel. A level of 5% isoflurane is given during 2 min followed by a level of 2% during 10 min (Fig. B.7). During the animal preparation, ears are filled with a mix of gel (ocry-gel) and wax, to limit air-related susceptibility artifacts in the images. After this common induction, four anesthetics are evaluated:

- Isoflurane (Iso): the level of isoflurane is set to 1% to be in a regime showing persistent behavior of spontaneous BOLD fluctuations (Wang et al., 2011). To evaluate the impact of strain, this anesthetic was evaluated in both Long-Evans and Wistar rats.
- Etomidate (Eto) (B. Braun, Melsungen, Germany): An administration in two stages is performed with a bolus of 10 mg/kg/min (3 min) injected in association with isoflurane at 4% during initiation, followed by a continuous intravenous infusion at 0.5 mg/kg/min.
- Medetomidine (Med) (Domitor, medetomidine hydrochloride; Orion Corporation, Espoo, Finland): An administration in two stages is performed with a bolus of 0.24 mg/kg injected subcutaneously in association with isoflurane at 4% during initiation, followed by a continuous infusion at 0.05 mg/kg/h.
- Urethane (Ure): A bolus of 1.25 g/kg is injected intraperitoneally (Rolland et al., 2013). The use of this anesthesia is well regulated and rats are euthanized at the end of the experiment because of the carcinogenic toxicity of this agent.
- A group of dead rats (Dead) was created by sacrificing 4 animals just before the experiment.

Overall, 6 groups were evaluated: Eto-L (n = 7), Iso-L (n = 6), Iso-W (n = 7), Med-L (n = 7), Ure-L (n = 7), Dead (n = 4).

*Appendix B.3. Systemic variables*

Two devices are used to monitor and record systemic variables (SV):

- A MouseOx Pulse oximeter (STARR Life Sciences Corp., Oakmont, PA, USA) with a rat sensor clipped on the right posterior paw of the animal. The system provides different measures: the peripheral arterial oxygen saturation (SpO2), the heart rate (heart rate). An error measure is also recorded to validate the measures recorded by the device. Only SV samples recorded by the oximeter and marked without errors are retained for the study;
- A SAII Trend (Small Animal Instruments Inc., Stony Brook, NY, USA) system is also used to record the temperature (Temp) from a rectal probe and the respiratory rate (resp. rate) from a small pneumatic pillow sensor. The error rate is computed as the ratio of the number of values recorded with code different from 0 (no error) on the oximeter to 3600, the number of samples during the whole rs-fMRI session. Clocks of the recording systems are verified at the beginning and at the end of the recordings, to follow a universal clock, noted, and eventually corrected. Measurements from the two systems are sampled at 1 Hz. No offline adjustments were necessary with the 1 s precision. During the experiments, a warm circulating water positioned below the animal is regulated to maintain the body temperature to a target level of 37$^{o}$C. Dead animals were not monitored, not regulated, and were imaged 1 h after sacrifice.

*Appendix B.4. MRI acquisitions*

Rats brains are scanned at 9.4 T with a volume transmit, 4-channel surface receive cross coil configuration (Paravision 6.0.1, Bruker, Ettlingen, Germany). After an anatomical T2w scan, cerebral blood flow (CBF) is mapped using pseudo continuous arterial spin labeling (pCASL; labeling duration 3000 ms, post-labeling delay 300 ms; TR = 3500 ms; TE = 9.7 ms; 20 averages; spin-echo 2D echo-planar readout with a spatial resolution 0.47 × 0.47 × 1.00 mm, gap 0.1 mm, 9 slices) following inter-pulse phase optimization as proposed in (Hirschler et al., 2018). Then, rs-fMRI was performed with a single shot echo-planar imaging with parameters set to: TR/TE = 500/20 ms, spatial resolution 0.47 × 0.47 × 1.00 mm, gap 0.1 mm, 9 slices, 3600 repetitions, duration 30 min. The volume of interest stands between 0 and -10 mm with respect to bregma and results in a volume of 64 × 64 x 9 voxels. Eventually, a second CBF map is acquired and averaged with the first CBF acquisition to obtain a mean CBF during the rs-fMRI experiment. Rats were strapped to the MRI insertion table with the head maintained with ear bars and a bite bar to prevent movements.

*Appendix B.5. Data processing*

Notations: LR: left right axis; IS: inferior superior axis; PA: posterior anterior axis., T: Temp, RR: resp. rate, HR: heart rate.

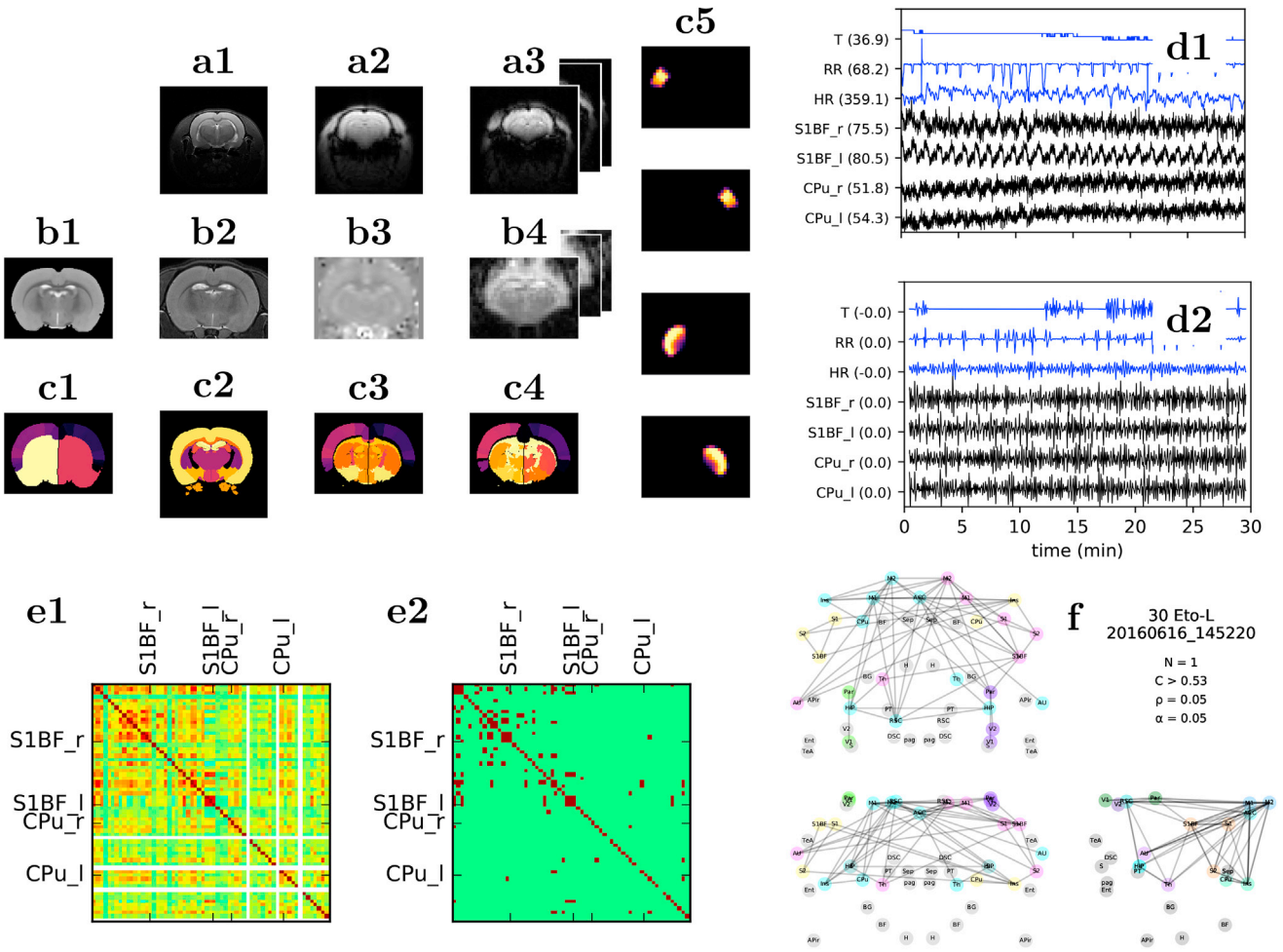


Notations: LR: left right axis; IS: inferior superior axis; PA: posterior anterior axis., T: Temp, RR: resp.rate, HR: heart rate.

**Fig. B.8.** Overview of the data processing to obtain FC graphs between brain areas on one rat: a-b) image transformations with reference on the Tohoku anatomic template (b1): raw (a1) and normalized (b2) anatomic MRI, raw (a2) and norm. (b3) perfusion MRI, raw (a3) and norm. (b4) fMRI; c) Atlas construction with reference on the Tohoku anatomic template (b1): Tohoku atlas (c1), WHS atlas (c2), merged atlas (c3), with left and right labeling (c4), low resolution area weights (c5) from top to bottom S1BF l, S1BF r, CPu l, CPu r; d) SV and fMRI signals extraction and wavelet decomposition: raw signals (d1) extracted from (b3) and (c5) and wavelet decomposition cD4 (d2); e) correlation matrix (e1) and thresholded one (e2) at density $\rho = 5$ %; f) FC graph corresponding to (e2). In this graph, locations of nodes correspond to the centers of gravity of brain areas. Edges indicate the connectivity between two areas. The graph is projected on the three standard projections LR-IS, PA-IS, and PA-LR (LR: left right axis; IS: inferior superior axis; PA: posterior anterior axis).

An overview of the data processing is given in Fig. B.8 Fig. B.8 for one individual, from the MR images to the graph representations of the brain activity and can be summarized as follows: fMRI BOLD signals are first extracted on N = 51 brain areas from a home-made atlas (Appendix C) based on published ones (Valdes Hernandez et al., 2011; Papp et al., 2014) after normalization of anatomical images and co-registration of fMRIs; Physiological and BOLD signals are motion corrected (Appendix E) and decomposed into different frequency bands with wavelet transforms described in the main text (see also Appendix F); Correlations are performed on these signals to evaluate FC.

*Appendix B.5.1. Atlas creation, co-registration and normalization of MRI*

The WHS atlas (Papp et al., 2014), focusing on subcortical areas is merged into the Tohoku atlas (Valdes Hernandez et al., 2011), focusing on cortical areas, to obtain our own atlas containing both cortical and subcortical areas (see Appendix C). All MRI recordings are aligned to the Tohoku template. Dimensions of voxels in the different spaces are: in the Tohoku space, 0.125 mm × 0.125 mm × 0.125 mm (0.002 $mm^3$), 136 × 102 × 180 voxels; in the WHS space, 0.0391 mm × 0.0391 mm × 0.0391 mm, 512 × 1024 × 512 voxels; for anatomical MRI, 0.117 mm × 0.117 mm × 0.8 mm, 256 × 256 × 27; for fMRI, 0.469 mm × 0.469 mm × 1.1 mm. Dimensions of anatomical images and rs-fMRI are multiplied by 10 to fit the dimension of the Tohoku atlas made to be compatible with algorithms of the Statistical Parametric Mapping software (SPM12) (Ashburner et al., 2014) defined for human images. The origin is manually set to match the origin of the Tohoku template i.e. to the bregma zero coordinate, at the apex of the most forward crossing fibers of the anterior commissure. A segmentation of the tissue of the anatomical image is computed and used to normalize the anatomical image to the Tohoku space. rs-fMRIs are realigned and resliced to the first image of the fMRI sequence. The coregistration variables are used to filter movements by analysing framewise displacements (Power et al., 2012) (Appendix E). A coregistration of the fMRIs on the anatomical image is computed and applied to all fMRIs while keeping the fMRI voxel size. For all these operations, a 4th degree B-spline interpolation is set. More precisely, these operations are realized using SPM 12 (Ashburner et al., 2014) with adaptation of rodents volumes to parameters of algorithms based on human volumes, following: **1** -

change of origin to the Bregma site and modification of a size of a factor of 10 for anatomical and fMRI volumes. (batch 'Reorient Images' with scaling parameters set to 10); **2** - Normalization of anatomical images to template. (batch 'Old Segment' with Gray matter, White matter and cerbro-Spinal Fluid in the native space and tissue probability maps taken from Tohoku space. Gaussian per class [2 2 2 4] / Affine regularisation: average sized template, Warping regularisation: 1, warp frequency cutoff: 25, bias regularisation: light regularisation (0.001), bias FWHM 60 mm cutoff; sampling distance: 3); **3** - Correction of acquisition offset and coregister fMRI volumes to the anatomical volume (batch Realign: Estimate & Reslice / quality: 0.9, separation: 4, smoothing (FWHM): 5, Num passes: register to first, interpolation: 2nd Degree B-Spline, Wrapping: no wrap, weighting: 0 files, resliced images: mean image only, interpolation: 4th degree B-spline, wrapping: no wrap, masking: mask images) (batch + Coregister: Estimate: Objective function: Normalized mutual information, separation: [4, 2], smoothing fwhm: [7,7], interp: 0, wrap: [0, 0, 0], mask: 0); **4** - Normalize fMRI images to template using transformation obtained in 2 (batch Old Normalize: Write/Bounding box: [[nan, nan, nan], [nan, nan, nan]], Voxel sizes [1.25, 1.25, 1.25], Interpolation: 0, Wrapping: [0, 0, 0]). At the end of the process, all CBF and all rs-fMRI images are in a volume of dimension 36 × 27 × 21, with voxel size 0.469 × 0.469 × 1.1 mm ($0.242\ mm^3$), the same resolution of the original fMRI but aligned and normalized to the Tohoku space.

*Appendix B.5.2. Cerebral blood flow maps*

CBF maps are obtained using homemade Matlab routines based on (Alsop et al., 2015; Hirschler et al., 2018). CBF values and rs-fMRI time courses are computed for each of the 51 areas of the atlas. If available, mean CBF values are extracted by averaging the values obtained before and after the rs-fMRI acquisition: $(\mathrm{CBF}_{\mathrm{before}} + \mathrm{CBF}_{\mathrm{after}})/2$.

*Appendix B.5.3. Signal extraction per area and wavelet decomposition*

The processing of fMRI images to extract signals from atlas areas is done with Python using the Nipy package (Gorgolewski et al., 2011) and home-made algorithms. The signal of an area is computed as the weighted summation of signals across all the voxels from that area (see Appendix D for details). rs-fMRI time course of an area (raw signal), is decomposed with a maximal overlap discrete wavelet transform (modwt) at different scales and Daubechies orthonormal compactly supported wavelets of length L = 8, using the wavedec package (Achard et al., 2006). Details coefficients cD1 to cD7, and an approximation coefficient cA7 that captures the polynomial trends contained in the signal are extracted. This last is generally a source of noise in observations. The limits of the frequency band $j$ is obtained by dividing the sampling frequency (2 Hz), by $2^{j+1}$ and $2^{j}$. In our study, $j$ varies from 1 to 7 leading to discard details <0.008 Hz where spectrums become flat (see Appendix F).

*Appendix B.5.4. Correlation of signals, graph creation and clustering*

The functional connectivity is obtained by computing the pairwise correlation $C_{ij}$ between area $i$ and $j$ of the BOLD signals filtered at different frequency bands (Achard et al., 2006) denoted $x_i$ and $x_j$. It is given by:

$$C(i,j) = \frac{\frac{1}{N}\sum_{k=1}^{N} x_{ci}(k)\, x_{cj}(k)}{\left(\frac{1}{N}\sum_{k=1}^{N} x_{ci}^2(k)\ \frac{1}{N}\sum_{k=1}^{N} x_{cj}^2(k)\right)^{1/2}} \tag{B.1}$$

with $x_{ci}$ the centered variable i. e. the variable with its sample mean subtracted $x_{ci} = x_i - \bar{x}_i$ for area $i$ over $N$ temporal samples. Graphs are then obtained:

- by finding a threshold for which the number of retained correlation values over the total number of possible connections represents the target density;
- by selecting areas as nodes and defining edges with correlation values over the retained threshold. The selection is made on significant correlations values (see also Appendix G).

The community detection algorithm is a greedy optimization of the modularity measure, from the default method of the igraph package (Csardi and Nepusz, 2006), igraph.Graph.community_fastgreedy (Clauset et al., 2004).

## Appendix C. Merging Tohoku and Waxholm atlases

Brain areas are obtained from the fusion of areas in the Tohoku atlas (Valdes Hernandez et al., 2011) and areas in the Waxholm Space atlas (WHS) (Papp et al., 2014). The first contains cortical areas, the second focuses on subcortical ones. Nomenclatures from Tohoku atlas are: agranular insular area dorsal (AID), posterior (AIP), ventral (AIV); amygdalopiriform transition area (APir); primary auditory area (Au1); secondary auditory cortex, dorsal area (AUD); secondary auditory cortex, ventral area (AuV); cingulate cortex, area 1 (Cg1); cingulate cortex, area 2 (Cg2); dysgranular insular cortex (DI); Entorhinal area (DIEnt); Entorhinal area (DLEnt); dorsolateral orbital cortex (DLO); ectorhinal cortex (Ect); frontal association cortex (Fr3); granular insular cortex (GI); granular insular cortex dysgranular insular cortex (GIDI); lateral parietal association cortex (LPtA); primary motor cortex (M1); supplementary motor cortex (M2); entorhinal cortex, medial part (MEnt); medial parietal association cortex (MPtA); perirhinal cortex (PRh); Parietal association cortex (PtPC), (PtPD), (PtPR); retrosplenial cortex (RSD), (RSGb), (RSGc); primary somatosensory cortex (S1), barrel field (S1BF), dysgranular zone (S1DZ), dysgranular zone (S1DZ0), forelimb region (S1FL), hindlimb region (S1HL), jaw region (S1J), (S1Sh), trunk region (S1Tr), upper limb (S1ULp); second somatosensory cortex (S2); temporal cortex, association area (TeA); primary visual cortex (V1), binocular region (V1B), monocular region (V1M); secondary visual cortex, lateral part (V2L), mediolateral part (V2ML), mediomedial part (V2MM); Entorhinal area (VIEnt) Nomenclatures from WHS atlas are: Clear Label (0); descending corticofugal pathways (cfp); substantia nigra (SN); subthalamic nucleus (STh); molecular layer of the cerebellum (Cb m); granule cell level of the cerebellum (Cb g); alveus of the hippocampus (alv); inferior cerebellar peduncle (icp); striatum (CPu); globus pallidus (GP); entopeduncular nucleus (EP); ventricular system (VS); medial lemniscus (Ml); facial nerve (7n); anterior commissure, anterior part (aca); anterior commissure, posterior part (acp); ventral hippocampal commissure (vhc); thalamus (Th); septal region (Sep); optic nerve (2n); optic tract and optic chiasm (opt); pineal gland (Pi); inner ear (IE); commissure of the superior colliculus (csc); brainstem (BS); hypothalamic region (H); inferior colliculus (IC); superficial gray layer of the superior colliculus (SuG); periaqueductal gray (pag); fornix (f);

mammillothalamic tract (mt); commissural stria terminalis (cst); deeper layers of the superior colliculus (DpG); periventricular gray (PVG); genu of the facial nerve (g7); pontine nuclei (Pn); fimbria of the hippocampus (fi); fasciculus retroflexus (fr); stria medullaris of the thalamus (sm); stria terminalis (st); posterior commissure (pc); glomerular layer of the accessory olfactory bulb (GlA); glomerular layer of the olfactory bulb (Gl); olfactory bulb (OB); corpus callosum and associated subcortical white matter (cc); brachium of the superior colliculus (bsc); commissure of the inferior colliculus (cic); interpeduncular nucleus (IP); ascending fibers of the facial nerve (asc7); anterior commissure (ac); spinal trigeminal nuclus (SPN); spinal trigeminal tract (sp5); frontal association cortex (FrA); middle cerebellar peduncle (mcp); transverse fibers of the pons (tfp); habenular commissure (hbc); nucleus of the stria medullaris (SM); basal forebrain region (BF); supraoptic decussation (sox); bed nucleus of the stria terminalis (BST); pretectal region (PT); cornu ammonis 3 (CA3); dentate gyrus (DG); cornu ammonis 2 (CA2); cornu ammonis 1 (CA1); fasciola cinereum (FC); subiculum (S); postrhinal cortex (PrCx); presubiculum (PrS); parasubiculum (PaS); perirhinal area 35 (Per35); perirhinal area 36 (Per36); entorhinal cortex (Ent); lateral entorhinal cortex (LEnt); parabrachial nucleus (PB); Some areas are both atlases and are merged in the final one. Fusions of areas for left and right hemisphere are as follows, with the name of the resulting areas given in Table C.2 followed by the list of the regrouped areas: 0: {0}; ACC: {Cg1 r, Cg2 r, Cg1 l, Cg2 l}; Ins: {AID, AIP, AIV, DI, GI, GIDI}; APir: {APir}; AU: {AU1, AUD, AUV}; Ent: {DIEnt, DLEnt, Ect, MEnt, PRh, VIEnt, PrCx, Per35, Per36, Ent, LEnt}; Par: {LPtA, MPtA, PtPC, PtPD, PtPR}; M1: {M1}; M2: {M2}; RSC: {RSD, RSGb, RSGC}; S1: {S1, S1DZ, S1DZ, S1FL, S1HL, S1J, S1Sh, S1Tr, S1ULp}; S1BF: {S1BF}; S2: {S2}; TeA: {TeA}; V1: {V1, V1B, V1M}; V2: {V2L, V2ML, V2MM}; CPu: {CPu}; BG: {SN, STh, GP, EP}; Th: {Th}; Sep: {Sep}; H: {H}; DSC: {SuG, DpG, bsc}; pag: {pag}; BF: {BF}; PT: {PT}; HIP: {CA3, DG, CA2, CA1}; S: {S, PrS, PaS}; f: {cfp, MI, 7n, aca, acp, vhc, 2n, opt, csc, f, mt, cst, g7, fi, fr, sm, st, pc, cc, cic, asc7, ac, sp5, mcp, tfp, hbc, sox, FC, BST}; n: {IC, Cb m, Cb g, alv, icp, VS, Pi, IE, BS, PVG, Pn, GlA, Gl, IP, SPN, SM, Fr3, FrA, DLO, OB, PB}; Note that 0 (clear label), fibers (f) and not available areas (n) are not taken into account in the study.

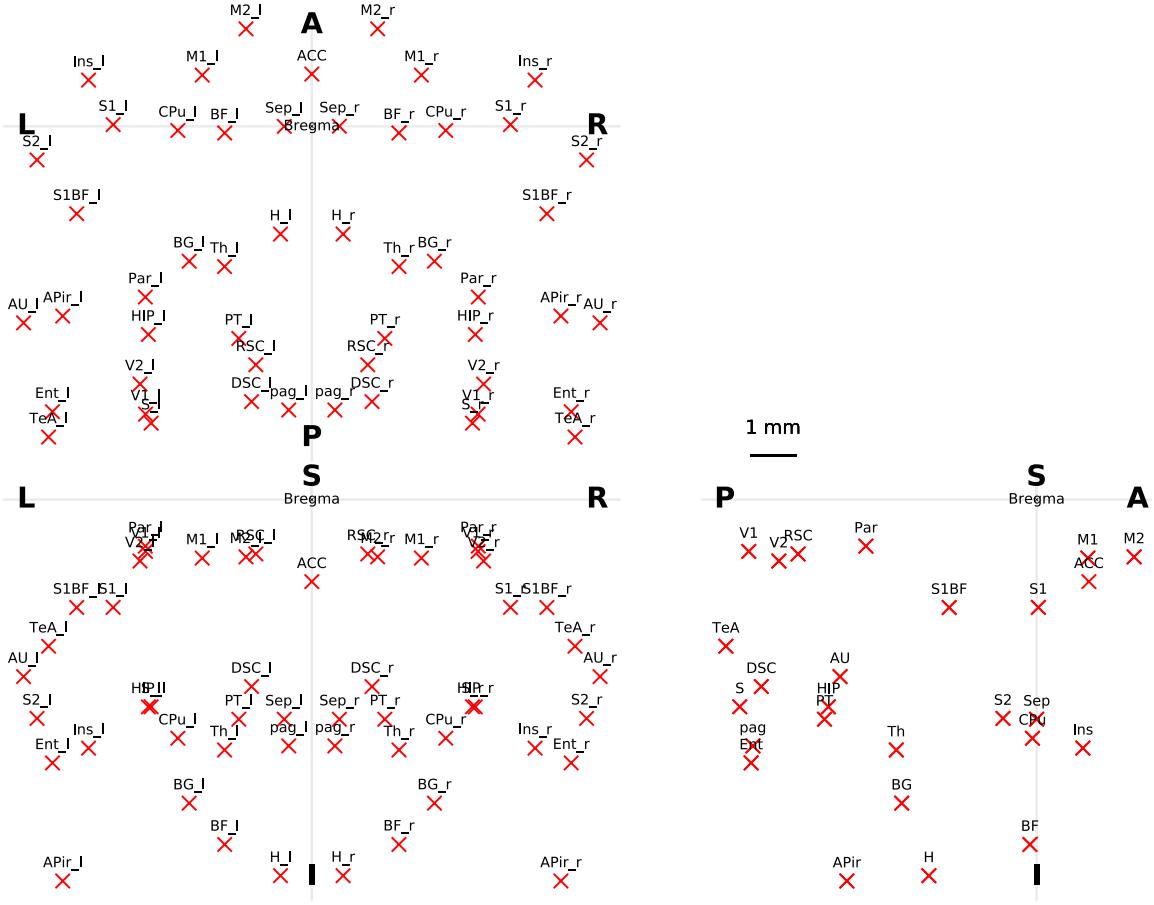


**Fig. C.9.** Locations of the centers of gravity of the areas retained in this study on the three projections LR-IS, PA-IS, and PA-LR. Notations: left to right axis (LR), inferior to superior axis (IS), posterior to anterior axis (PA).

Centers are projected on the left and right (LR) axis, inferior-superior (IS) axis and on the posterior-anterior (PA) with the origin at (0, 0, 0) given by the position of bregma at the apex of the most forward crossing fibers of the anterior commissure (Fig. C.9). Coordinates are given in millimeters. For sake of symmetry, the average left-right center of gravity is considered. The position of ACC is set to 0 on the LR axis, even if a small shift is present in the template.

**Table C.2**
Brain areas in the atlas

| # | Name | label | x | y | z | N | h. | w. a. |
|---|---|---|---|---|---|---|---|---|
| *0* | Clear Label | *0* | *0.2* | *−4.6* | *−4.5* | 1718587 | | |
| 1 | anterior cingulate cortex | ACC | 0.2 | −1.9 | 1.2 | 16670 | | acc |
| 2 | insular cortex right | Ins r | 5.2 | −5.7 | 0.9 | 11026 | r | c |
| 3 | amygdalopiriform transition area right | APir r | 5.7 | −8.8 | −4.3 | 3264 | r | c |
| 4 | auditory cortex right | AU r | 6.6 | −4.2 | −4.5 | 8781 | r | c |
| 5 | entorhinal area right | Ent r | 5.9 | −6.1 | −6.4 | 18392 | r | c |
| 6 | parietal association cortex right | Par r | 4.0 | −1.2 | −3.9 | 4557 | r | c |
| 7 | primary motor cortex right | M1 r | 2.7 | −1.4 | 1.1 | 11027 | r | c |
| 8 | supplementary motor cortex right | M2 r | 1.7 | −1.3 | 2.2 | 6619 | r | c |
| 9 | retrosplenial cortex right | RSC r | 1.5 | −1.3 | −5.5 | 8222 | r | c |
| 10 | somatosensory 1 right | S1 r | 4.6 | −2.6 | −0.0 | 20647 | r | c |
| 11 | somatosensory 1 right, barrel field | S1BF r | 5.5 | −2.6 | −2.0 | 9249 | r | c |
| 12 | somatosensory 2 right | S2 r | 6.2 | −5.1 | −0.8 | 2365 | r | c |
| 13 | temporal cortex right, association area | TeA r | 6.1 | −3.5 | −7.1 | 1572 | r | c |
| 14 | primary visual cortex right | V1 r | 4.0 | −1.3 | −6.5 | 9100 | r | c |
| 15 | secondary visual cortex right | V2 r | 4.1 | −1.5 | −5.9 | 4350 | r | c |
| 16 | insular cortex left | Ins l | −5.0 | −5.6 | 1.2 | 9002 | l | c |
| 17 | amygdalopiriform transition area left | APir l | −5.7 | −8.6 | −4.3 | 3411 | l | c |
| 18 | auditory cortex left | AU l | −6.5 | −3.9 | −4.5 | 9338 | l | c |
| 19 | entorhinal area left | Ent l | −5.9 | −5.8 | −6.6 | 17859 | l | c |
| 20 | parietal association cortex left | Par l | −3.6 | −0.9 | −3.9 | 4557 | l | c |
| 21 | primary motor cortex left | M1 l | −2.3 | −1.3 | 1.3 | 11160 | l | c |
| 22 | supplementary motor cortex left | M2 l | −1.3 | −1.3 | 2.2 | 5708 | l | c |
| 23 | retrosplenial cortex left | RSC l | −1.1 | −1.2 | −5.3 | 7527 | l | c |
| 24 | somatosensory 1 left | S1 l | −4.4 | −2.3 | 0.1 | 21813 | l | c |
| 25 | somatosensory 1 left, barrel field | S1BF l | −5.2 | −2.3 | −2.0 | 9578 | l | c |
| 26 | somatosensory 2 left | S2 l | −6.3 | −4.8 | −0.8 | 2547 | l | c |
| 27 | temporal cortex left, association area | TeA l | −5.9 | −3.2 | −7.1 | 1731 | l | c |
| 28 | primary visual cortex left | V1 l | −3.6 | −1.1 | −6.6 | 9439 | l | c |
| 29 | secondary visual cortex left | V2 l | −3.7 | −1.3 | −5.9 | 4276 | l | c |
| 30 | caudate-putamen striatum right | CPu r | 3.0 | −5.6 | −0.1 | 23113 | r | s |
| 31 | basal ganglia right | BG r | 2.6 | −7.1 | −3.1 | 3548 | r | s |
| 32 | thalamus right | Th r | 2.0 | −5.8 | −3.2 | 16544 | r | s |
| 33 | septal region right | Sep r | 0.6 | −5.0 | 0.0 | 2167 | r | s |
| 34 | hypothalamic region right | H r | 0.6 | −8.6 | −2.5 | 2613 | r | s |
| 35 | superior colliculus right | DSC r | 1.4 | −4.4 | −6.3 | 6253 | r | s |
| 36 | periaqueductal gray right | pag r | 0.5 | −5.5 | −6.6 | 2745 | r | s |
| 37 | basal forebrain region right | BF r | 1.8 | −8.0 | −0.3 | 13759 | r | s |
| 38 | pretectal region right | PT r | 1.6 | −5.1 | −4.8 | 1805 | r | s |
| 39 | hippocampus right | HIP r | 3.7 | −4.9 | −4.7 | 19137 | r | s |
| 40 | subiculum right | S r | 3.6 | −4.8 | −6.8 | 5671 | r | s |
| 41 | caudate-putamen striatum left | CPu l | −3.1 | −5.2 | −0.1 | 22803 | l | s |
| 42 | basal ganglia left | BG l | −3.0 | −6.7 | −3.1 | 3238 | l | s |
| 43 | thalamus left | Th l | −2.0 | −5.6 | −3.2 | 18218 | l | s |
| 44 | septal region left | Sep l | −0.6 | −5.0 | −0.0 | 2733 | l | s |
| 45 | hypothalamic region left | H l | −0.8 | −8.5 | −2.4 | 4246 | l | s |
| 46 | superior colliculus left | DSC l | −1.3 | −4.2 | −6.3 | 6465 | l | s |
| 47 | periaqueductal gray left | pag l | −0.5 | −5.7 | −6.3 | 3794 | l | s |
| 48 | basal forebrain region left | BF l | −2.1 | −7.7 | −0.0 | 17694 | l | s |
| 49 | pretectal region left | PT l | −1.7 | −4.9 | −4.8 | 1706 | l | s |
| 50 | hippocampus left | HIP l | −3.8 | −4.5 | −4.8 | 18981 | l | s |
| 51 | subiculum left | S l | −3.7 | −4.6 | −6.7 | 5962 | l | s |
| *52* | fasciculum | f | *−0.0* | −4.8 | *−3.1* | 59834 | | |
| *53* | not available | *n* | *−0.1* | −5.8 | *−7.7* | 261557 | | |

For each area: name of the area (name); label (label); the coordinates of the center of gravity (x, y, z), in mm, in the referential LR, IS, PA, with the origin centered at bregma location; N, the number of voxels in the area with a voxel size of 0.125 mm by 0.125 mm by 0.125 mm, in a cube of 136 by 102 by 180 voxels; the hemisphere (hemi.), left (l.) or right (r.); and the name of the wider area (w. a.), anterior cingulate cortex (acc), cortical (c) or subcortical (s). Rows in italic correspond to areas containing unlabeled subareas, undefined or unspecific residuals components not used in the study.

The smallest area TeA r has a volume of 3.070 $mm^3$ (1572 voxels at 0.002 $mm^3$ or 12 voxels at 0.242 $mm^3$), the largest one CPu r, has a volume of 45.143 $mm^3$ (23113 or 186 voxels, respectively).

## Appendix D. Extraction of signals from fMRI and atlas

The simple way to compute the signals in areas defined in the atlas is to transform the data from the fMRI low resolution volume to data in the high resolution volume where the atlas is defined. The signal in one fMRI area is obtained as the sum of all voxels of this area in the atlas. This process implies to transform large voxels into small ones. The extraction of signals from the low resolution volume fMRI is possible if one can compute the proportion of each area contained in voxels of the fMRI. The processing of signals from the low resolution volume fMRI can then be seen as a weighted summation of voxel data for each area or a source separation problem. This enables to reduce the size of the processed images and reduce the computation times, while obtaining the same result as if working in the high resolution volume of the atlas. The mathematical framework for this operation is described here.

*Appendix D.1. Equivalence of operations for processing low resolution volumes and high ones*

Let $V_1$ and $V_2$ be two volumes containing MRI values at different resolutions. $V_1$ and $V_2$ contains respectively $N_1$ and $N_2$ voxels. We consider here that: each voxel $i_1$ in $V_1$ is associated to one label of one area of the atlas; $V_1$ contains more voxels than $V_2$, or $N_1 \geq N_2$. This is generally the case when $V_1$ is the anatomical volume and $V_2$ is the fMRI volume with a lower resolution. Voxels in $V_2$ intersect voxels in $V_1$ at different locations. An example in two dimensions is given in Fig. D.10. Let $K$ be the number of areas in the atlas and $k$ the area label with index $k$. Let $s(k,t)$ be the signal of area $k$ at time $t$. Let $s_1(k,t)$ and $s_2(k,t)$ be the signals computed from $V_1$ and $V_2$. The problem here is to obtain $s_2(k,t) = s_1(k,t) = s(k,t)$.

If the fMRI is obtained from $V_2$, values $x_2(i_2,t)$ of voxels $i_2$ are transformed into $V_1$ such that $i_1$ contains values $x_1(i_1,t)$ by applying:

$$\begin{aligned} &x_1(i_1,t) = \sum_{i_2} \rho(i_1,i_2)\, x_2(i_2,t) \\ &\text{or} \quad X_1(t) = R\, X_2(t) \quad \text{in matrix notation} \end{aligned} \tag{D.1}$$

where $\rho(i_1,i_2)$ contains the fraction of $i_2$ in $i_1$. $s_1(k,t)$ can be computed by taking the voxels labeled with area $k$, or when taking $\omega(i_1)$, the label of the area related to the voxel $i_1$ in the atlas, by:

$$\begin{aligned} &s_1(k,t) = \sum_{i_1 | \omega(i_1)=k} x_1(i_1,t) \\ &\text{or} \quad s_1(k,t) = \sum_{i_1} w_1(k,i_1)\, x_1(i_1,t) \\ &\text{or} \quad S_1(t) = W_1\, X_1(t) \quad \text{in matrix notation} \end{aligned} \tag{D.2}$$

Where $w_1$ is an indicator function giving $w_1(k,i_1) = 1$ if $\omega(i_1) = k$ and 0 otherwise. This leads to:

$$\begin{aligned} &s_1(k,t) = \sum_{i_1} w_1(k,i_1) \sum_{i_2} \rho(i_1,i_2)\, x_2(i_2,t) \\ &S_1(t) = W_1\, R\, X_2(t) \end{aligned} \tag{D.3}$$

By taking $w_2(k,i_2) = \sum_{i_1} w_1(k,i_1)\, \rho(i_1,i_2)$ or $W_2 = W_1\, R$ in matrix notation this leads to:

$$\begin{aligned} &s_1(k,t) = \sum_{i_2} w_2(k,i_2)\, x_2(i_2,t) \\ &S_1(t) = W_2\, X_2(t) = S_2(t) \end{aligned} \tag{D.4}$$

This implies that $s_1(t)$ computed in this way does not rely on the computation of $x_1$ and can be noted $s_2(t)$.

Now, suppose that the signal recorded in $V_2$, $x_2(t)$ is a combination of $s(k,t)$ such that:

$$X_2(t) = M\, S(t) \tag{D.5}$$

With $M$ a mixing matrix of size $(N_2, K)$. The resolution of this equation is given by the pseudo inverse and leads to:

$$S(t) = (M^t\, M)^{-1}\, M^t\, X_2(t) \tag{D.6}$$

with $.^t$ the notation for the transpose operator. This implies that one admissible solution for $S_2(t) = S(t)$ is obtained if $W_2 = (\widehat{M}^t\, \widehat{M})^{-1}\, \widehat{M}^t$ or $W_2\, \widehat{M} = I$. $\widehat{M}$ is then a pseudo inverse of $W_2$ and can be chosen this way. Thus, the matrix $W_2$ is obtained from $R$ and $W_1$ computed on our configuration, with the atlas in high resolution and the fMRI in low resolution. This last has been used to compute the signals of each area from the signals in the fMRI volumes in 3D.

*Appendix D.2. Example of the equivalence of operations for processing low resolution volumes and high ones*

An example of equivalence of operations for extracting brain areas signals from volume $V_1$ (in blue) and $V_2$ (in red) is given in Fig. D.10.

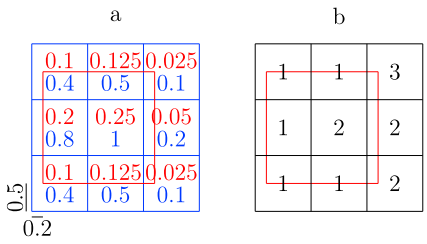


**Fig. D.10.** Example of: a) the transformation from volume $V_1$ to volume $V_2$ and in blue the fraction $\rho(i_1,i_2)$ and the proportion of components from $s(i,t)$ in red (see text for details); b) the label contained in $V_1$ and the intersection with $V_2$.

In the 2D example, there are three labels $\{1, 2, 3\}$, nine voxels in $V_1$ and one in $V_2$. If voxels are viewed rowwise, one can make the hypothesis that $x_2$ is obtained from:

$$x_2(1,t) = M\ (s(1,t), s(2,t), s(3,t))^t$$

with $M$ being a 3 by 1 matrix here. Taking the red proportions, obtained by computing the ratio of the areas of the intersections of the blue voxels over the area of the red voxel, and summing them for each labeled area leads to:

$$\begin{aligned} M &= (0.1 + 0.125 + 0.2 + 0.1 + 0.125, 0.25 + 0.05 + 0.025, 0.025) \\ M &= (0.65, 0.325, 0.025) \end{aligned} \tag{D.7}$$

The signal recorded in the red voxel is a composition of the signal in the three areas with a mixture according to M. In simple words, the signal recorded in the red voxel is made of 65% of signal from area 1, 32.5% of signal from area 2 and 2.5% of signal from area 3.

All blue voxels are represented in a flat vector of dimension 9 in rowwise reading, from the top left to the bottom right. Taking the blue proportions, obtained by computing the ratio of the intersections of the red voxel with the areas of each blue voxel, gives $R$, the weights of voxels from $V_2$ in $V_1$:

$$R = (0.4, 0.5, 0.1, 0.8, 1, 0.2, 0.4, 0.5, 0.1)^t$$

The mixture matrix in $V_1$ from the 9 voxels to the 3 signals is given by $W_1$:

$$W_1 = \begin{pmatrix} 1 & 1 & 0 & 1 & 0 & 0 & 1 & 1 & 0 \\ 0 & 0 & 0 & 0 & 1 & 1 & 0 & 0 & 1 \\ 0 & 0 & 1 & 0 & 0 & 0 & 0 & 0 & 0 \end{pmatrix}$$

This leads to:

$$W_2 = W_1\ R = (2.6, 1.3, 0.1)^t$$

$$\widehat{M} \approx (0.31, 0.15, 0.01)$$

$\widehat{M}$ and $M$ are related with a factor equals to $\sum_k \widehat{m}_k \approx 0.47$. Thus, signals at low resolution and high resolution just differ by a scaling factor.

## Appendix E. Movement filtering with framewise displacement

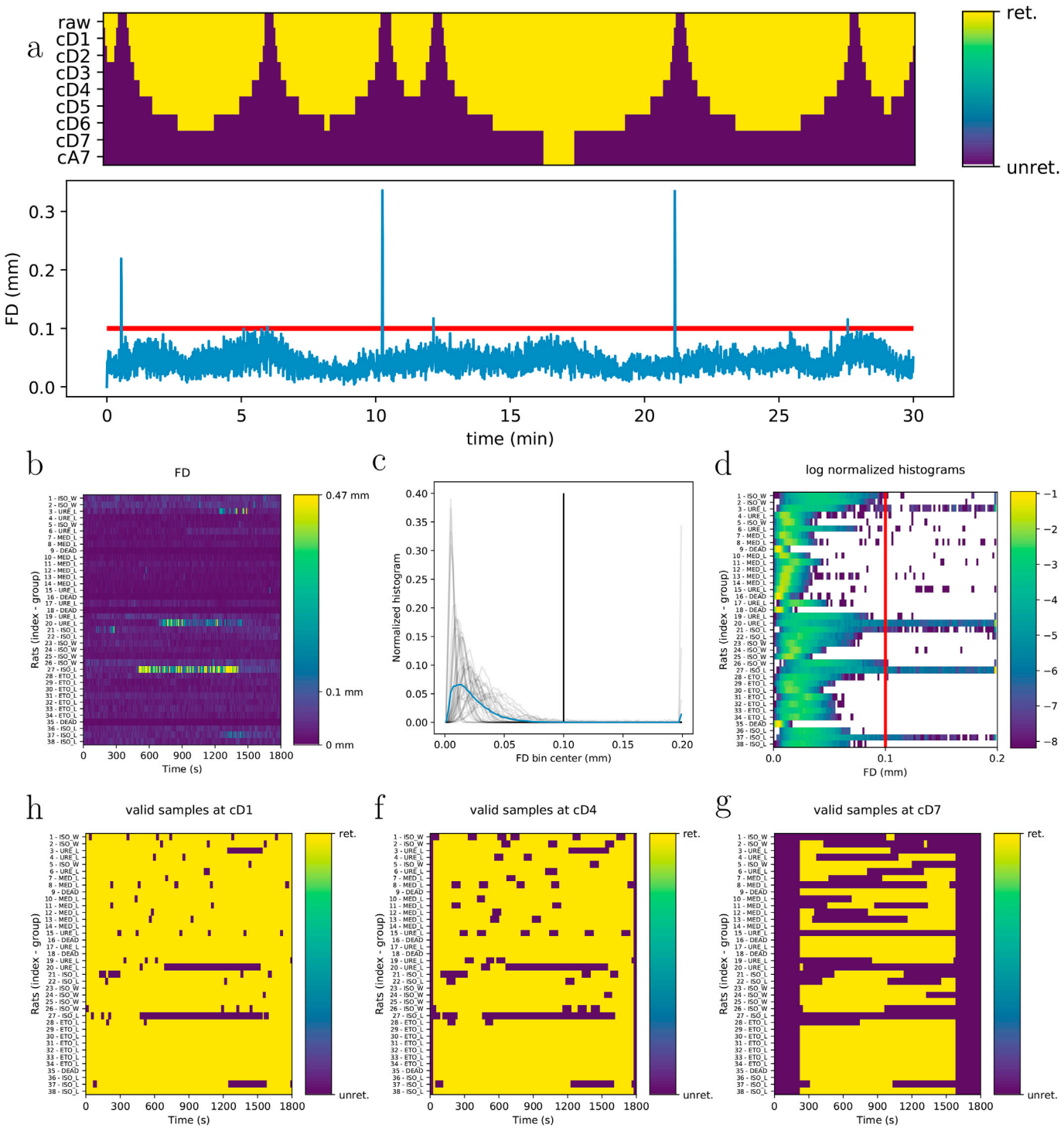


**Fig. E.11.** Selection of retained rs-fMRI based on framewise displacement (FD). a) FD and impact on the raw signal and signals at different frequency bands. b) Overview of the FD for all rats. 0.47 mm represents the lowest dimension of voxels. 0.1 is the threshold used in the study. c) Normalized histograms of FD: rat histograms are proposed in gray. Values of FD over 0.2 are set to 0.2. Values in bins are normalized by dividing samples in bins with the total number of samples. The average histogram computed with all individuals is given in blue. d) Overview of histograms for each rat: a logarithmic version is proposed to enhance details and put in evidence that some values over the threshold are observed in several rats. h-f) Examples of the retained (ret.) and unretained (unret.) samples for the signal at cD1 (h), cD4 (f) and cD7 (g). The number of rejected samples increases as the frequency decreases because of the impact of the wavelet support.

Following observations in (Power et al., 2012), we examined carefully the potential influence of motions on the obtained signals. In order to obtain the best estimates of FC during resting state, a selection of the parts of signals not contaminated potentially by movement is performed. Samples with a framewise displacement (FD) (Power et al., 2012) over an experimental threshold are discarded from the study. The threshold is set manually to 0.1 mm, based on observations, see infra., and corresponding to approximately 1/4 of the smaller voxel dimension (0.47 mm) and 1/9 of the larger voxel dimension (0.9 mm). All samples following a sample with FD over this threshold are also marked as movement and discarded for the study. This is done to take into account the effect of an hemodynamic response function (HRF). The maximal duration of this HRF is set to 20 s based on values proposed in literature (see (Ashburner et al., 2014) for example and references). The border effects of the signals at different scales are then taken into account. To summarize, with technical terms of the field, we applied a scrubbing method with boxcar filtering (Yan et al., 2013) taking into account HRF and wavelet support at different scales. An example of the FD obtained for one rat is given in Fig. E.11a with the impact on the signals at the different frequency bands. An overview of the FD obtained for all rats is given in Fig. E.11. Three rats showed major displacements (FD over 0.47 mm). Distributions of FD are proposed in Fig. E.11 c-d with the proposed threshold for this study. The impact of the selection of the unretained samples on the signals at the different frequency bands is presented in Fig. E.11h-g for all rats. The impact on signals at low frequencies (Fig. E.11g - cD7) is important, as a consequence of the width of the wavelet support at this scale, leading to few or no available samples to estimate FC.

## Appendix F. Spectral analysis of fMRI signals and frequency bands

To evaluate which part of the BOLD raw signal is filtered at each frequency band, the power spectral densities (PSD) by groups are given in Fig. F.12. PSD are estimated using a Welch averaging method (frequency precision 3.9e-3 Hz, duration of segments 128 s, overlap: 50%). PSD per area and per rat are superimposed in black with a transparency factor. The median PSD for each rat is computed and the average value is given in color for each group with a margin corresponding to the standard error of the mean. An acquisition artifact, visible in all groups including the dead animal, may be seen close to the cD2 upper frequency (0.5 Hz).

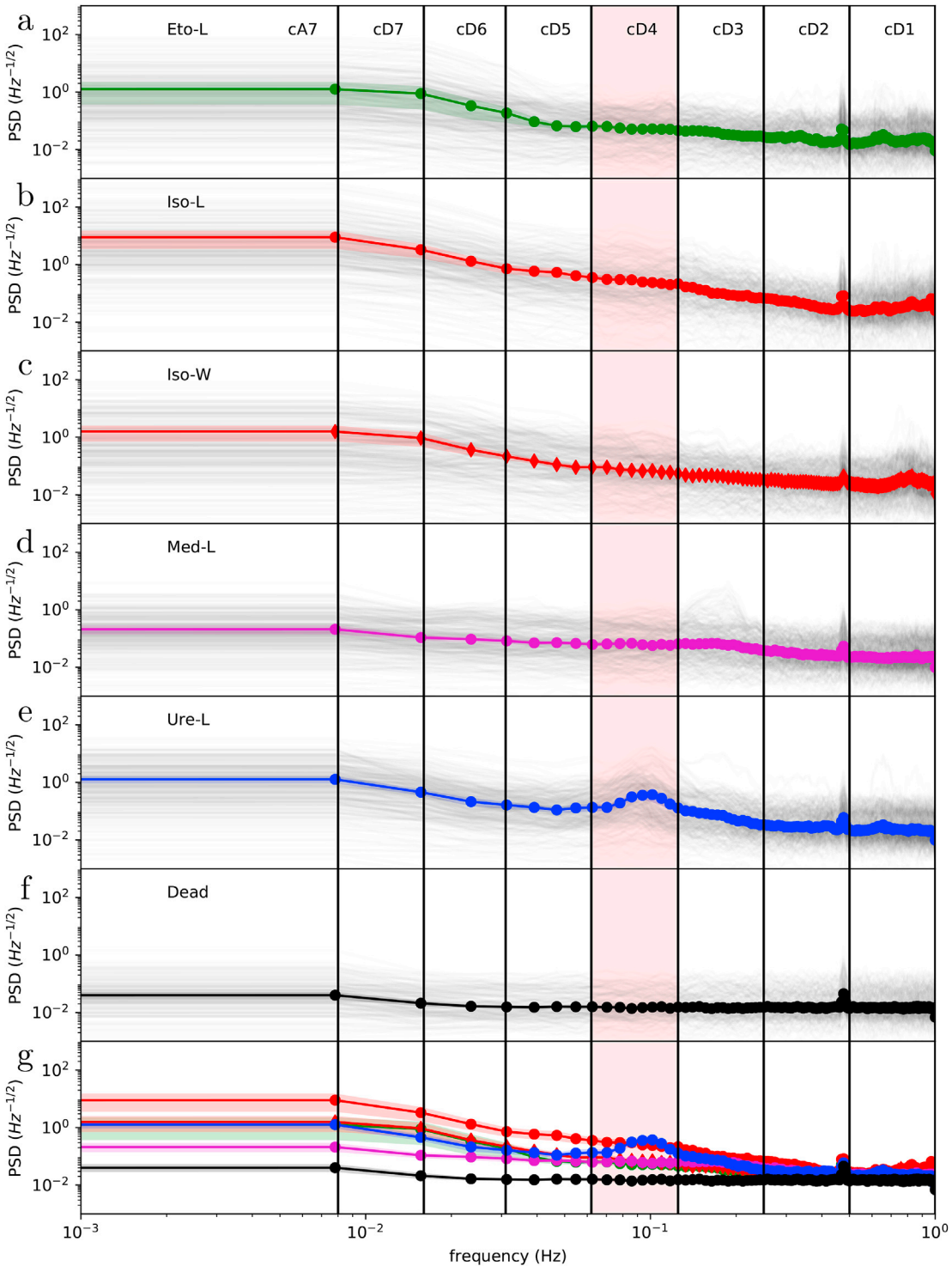


**Fig. F.12.** Power spectral density (PSD) of BOLD raw signals by group. a-f) For each group, the 51 PSD of each animal are superimposed in black with a transparency factor. The median values per frequency is computed for each animal. Means and standard errors of the mean are given in colors. The cD4 band, retained in this study and called BOLD signal, is colored in red. g) Average PSD for the different groups.

*Appendix F.1. Frequency bands used in other FC studies*

For comparison purpose, a graphical representation of the different frequency bands retained in other rat studies is proposed in Fig. F.13 (see also (Masamoto and Kanno, 2012)).

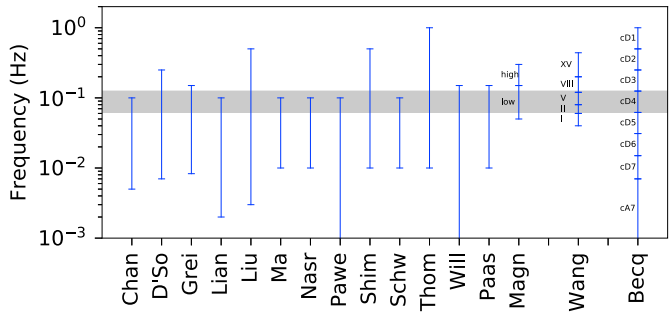


**Fig. F.13.** Frequency bands retained in different rat rs-fMRI studies and all the frequency bands available in this study. The cD4 band (i.e. the BOLD signal) is filled in gray. Frequency cuts in Hz are given in parenthesis. The repetition time TR is also provided. (Chan et al., 2014) (0.005, 0.1) TR = 1.5 s; (D'Souza et al., 2014) (0.007, 0.25) TR = 2 s; (Greicius et al., 2003) (0.0083, 0.15) TR = 2 s; (Liang et al., 2015) (0.002, 0.1) TR = 1 s; (Liu et al., 2013a) (0.003, 0.5) TR = 0.612 s; (Ma et al., 2016) (0.01, 0.1) TR = 1 s; (Nasrallah et al., 2014) (0.01, 0.1) TR = 2 s; (Pawela et al., 2008) (0, 0.1) TR = 2 s; (Shim et al., 2012) (0.01, 0.5), and detrended to the second order, TR = 1 s; (Schwarz et al., 2013) (0.01, 0.1) TR = 1.7 s; (Thompson et al., 2014) (0.01, 1), and linear detrend, TR = 0.5 s; (Williams et al., 2010) (0, 0.15), and normalization, TR = 0.1 s; (Paasonen et al., 2018) (0.01, 0.15), TR = 2 s; (Magnuson et al., 2014) (0.05, 0.15, 0.30) and normalization TR = 0.5 s; (Wang et al., 2014) (0.04, 0.06, 0.08, 0.12, 0.2, 0.44) simulated TR = 2 s; Becq et al., this study, (0, 0.007, 0.015, 0.031, 0.062, 0.125, 0.25, 0.5, 1) TR = 0.5 s.

## Appendix G. Construction of FC graphs from band filtered signals taking into account significant correlations

Two important points must be considered during the construction of FC graphs:

- Spurious correlations depend of the number of samples used to compute correlations. This number is function of the frequency band of interest. For a lower frequency of interest, fewer samples are needed, and spurious correlations are less likely.
- Spurious correlations are obtained when comparing multiple values of correlations as a consequence of multiple connections between brain areas. This implies to adjust level for multiple corrections.

First, we evaluate whether there are enough signals in the graphs to get a sufficient number of edges by counting the number of significant edges different from zero. This number is computed using the results from (Whitcher et al., 2000) where it is shown that the Fisher transform $z$ of the empirical correlation $\widehat{\rho}$ follows a Gaussian law with mean the Fisher transform of the true value and variance depending on the number of available wavelet coefficients at scale $j$, denoted $N_j$ here. The confidence interval $[\rho_m, \rho_M]$ for the correlation of two random signals is given in (Whitcher, 1998; Whitcher et al., 2000) at a given scale $j$ with a Daubechies wavelet filter of length $L$.

$$\rho_{m,M} = \tanh\left(h(\rho) \pm \frac{\Phi^{-1}(1-p)}{\sqrt{(\widehat{N}_j - 3)}}\right) \tag{G.1}$$

$$\widehat{N}_j = \frac{N}{2^j} - L_j \tag{G.2}$$

$$L_j = (L-2)\left(1-2^{-j}\right) \tag{G.3}$$

where $\widehat{N}_j$ is the number of wavelet coefficients associated with scale $\lambda_j$, $h(\rho) = \tanh^{-1}(\rho)$ and $\Phi^{-1}(p)$ is the $p$th quantile of the standard normal distribution. A Bonferroni procedure is applied to the $p$ value to take into account $ne = nv\,(nv-1)/2 = 51 \times 50/2 = 1275$ repetitions of the $nv = 51$ brain areas to obtain a level with $p_{bf} = p/ne$.

A model of uncorrelated random noises, with $\rho = 0$, is used to obtain significant thresholds at an initial symmetrical confidence interval set to 95% leading, after Bonferroni correction, to a level $p_{bf} = 0.025/1275 = 1.96e-5 = 0.002$ %. 51 signals with 3600 samples with i.i.d. samples following a Gaussian distribution $N(0,1)$ are simulated. The same wavelet decomposition than the one used for the BOLD signals is applied and the $ne$ correlations are estimated for each wavelet coefficients. Examples of distributions of the correlations at different wavelet levels are given in Fig. G.14a.

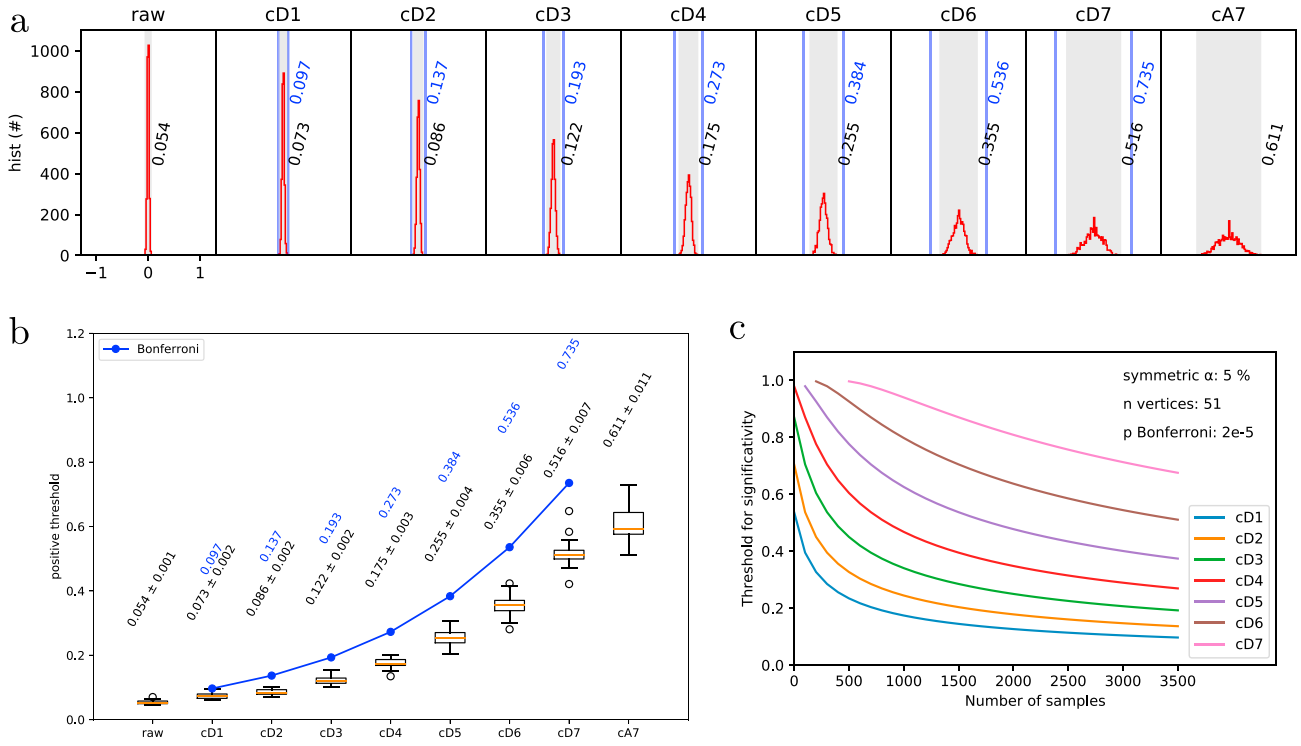


**Fig. G.14.** Distributions of correlations at different scales for one drawing of random signals and the empirical upper limit threshold of the segment containing 99.998% (95% Whitcher + Bonferroni procedure) of the values. a) Histograms estimated on 100 bins between [-1, 1]; b) Boxplot of the thresholds containing 99.998% of the distributions at different wavelet levels. Values from the Bonferroni procedure with a an initial symmetrical confidence interval at 95% are in blue. Values from empirical distributions of the simulated noises are given in black. c) Threshold for significant correlations in function of the number of samples per frequency bands. Plots are obtained with Eq.G.4 setting p = 2e-5 for taking into account Bonferroni corrections on a symmetric test at level $\alpha = 5\%$ with 51 areas.

Values are ranked and the correlation value of the $i_{th} = ne\,(1 - p_{bf}) = 1275 \times (1 - 1.96e - 5) = 1275$ th (max) is retained as the threshold level for which 99.998% of abs(C) is contained. Theoretical values given by Whitcher and the Bonferroni procedure are given in blue. Distributions and values of these thresholds at different wavelet levels are given in Fig. G.14b with the segment containing 99.998% of the values represented in gray.

Differences between theoretical thresholds and experimental ones increase with scale indices. Unfortunately, there is no result about the theoretical distribution of the correlation coefficients to the best of our knowledge and it seems not easy to obtain.

Because of the scrubbing based on FD, signals obtained on different rats do not have the same size. Besides, nonsuccessive samples are retained and in this condition, Eqn G.1 can not be applied properly. But since the retained samples are already taking into account the influence of the wavelet support, the following formula is used to obtain the limits of significant correlations:

$$\rho_{m,M} = \tanh\left(h(\rho) \pm \frac{\Phi^{-1}(1-p)}{\sqrt{\left(\frac{N_r}{2^j} - 3\right)}}\right) \tag{G.4}$$

with $N_r$ the number of retained samples. The limits of significant correlations at different scales in function of the number of retained samples is proposed in Fig. G.14c putting in evidence the importance of the number of samples for obtaining significant correlations at low frequencies (cD7).

This allows the computation of a confidence interval to remove the correlations that are below the significance level. For examples, the theoretical Bonferroni threshold is 0.273 for the cD4 band, if all samples are retained with $N = 3600$ for Eqn G.1 and $N_r = 3495$ for Eqn G.4 with a Daubechies wavelet of size $L = 8$. This is illustrated on the dead rats data where no signal is detected in the graphs. Following this first step, the idea to use graphs is to be able to compare them. The comparison of graphs with different number of edges is difficult because graph metrics are directly impacted by this factor. We choose here to force the graphs to have the same number of edges, selected from the significant ones. Because dead rats have a too small number of significant edges, it is not possible to construct a graph with a constant number of edges for these animals.

## Appendix H. Supplementary Analyses

### *Appendix H.1. Scatter plots*

Scatter plots of SV, baseline CBF, BOLD variation and $\langle C \rangle$ BOLD-BOLD (Fig. I.20 to Fig. I.28) can be further analysed here. Most of the individuals in each group remain close to each other indicating an homeostatic state specific to each anesthetic. The effect of the strain can be evaluated on the Iso-L

and Iso-W groups that show separated clouds. There are some outliers: One individual with Temp <35 °C in the Eto group but this is caused by problems with the temperature sensors (regular values between 35 and 37 °C); One individual with SpO2 < 80% in the Ure group. Estimation of regression parameters and correlation coefficients are given in each figure, with outliers discarded for the regression. There are some statistically significant correlations:

- weak correlations ($|R| < 0.5$): BOLD variation with (RR, Temp, Error rate, raw BOLD); $\langle C \rangle$ BOLD-BOLD with (HR, Error rate, raw BOLD); HR with Error rate; RR with SpO2; Temp with Error rate; Weight with raw BOLD.
- medium correlations ($0.5 \leq |R| < 0.75$): BOLD variation with ($\langle C \rangle$ BOLD-BOLD, Error rate); $\langle C \rangle$ BOLD-BOLD with Temp; baseline CBF with (HR, Temp); HR with Temp; RR with Error rate; SpO2 with Error rate.
- one strong correlation ($|R| \geq 0.75$): BOLD variation with $\langle C \rangle$ BOLD-BOLD.

The error rate is correlated with several variables. This can be explained by the fact that when the signal is lost on the oximeter, either the animal is not stable during the anesthesia creating some artifacts measures, either the animal is in a state in which he needs to regulate himself. If the animal is suffering, reactions can induce error rates, and these reactions are observed and can be related to the activity in BOLD signals. These reactions can also be related to an increase in <C> BOLD-BOLD with answers to the same conditional stimuli, e.g. pain, suffering, wake up. The temperature is related to different variables especially, HR, baseline CBF, BOLD variation and <C> BOLD-BOLD. This potentially indicates that 'hot rats' are better perfused, have stronger neural activities and stronger FCS between areas. BOLD variation has a strong correlation with <C> BOLD-BOLD indicating that rats with high BOLD variations show high correlations values even after taking into account the motions correctly.

*Appendix H.2. Influence of area size on FCS*

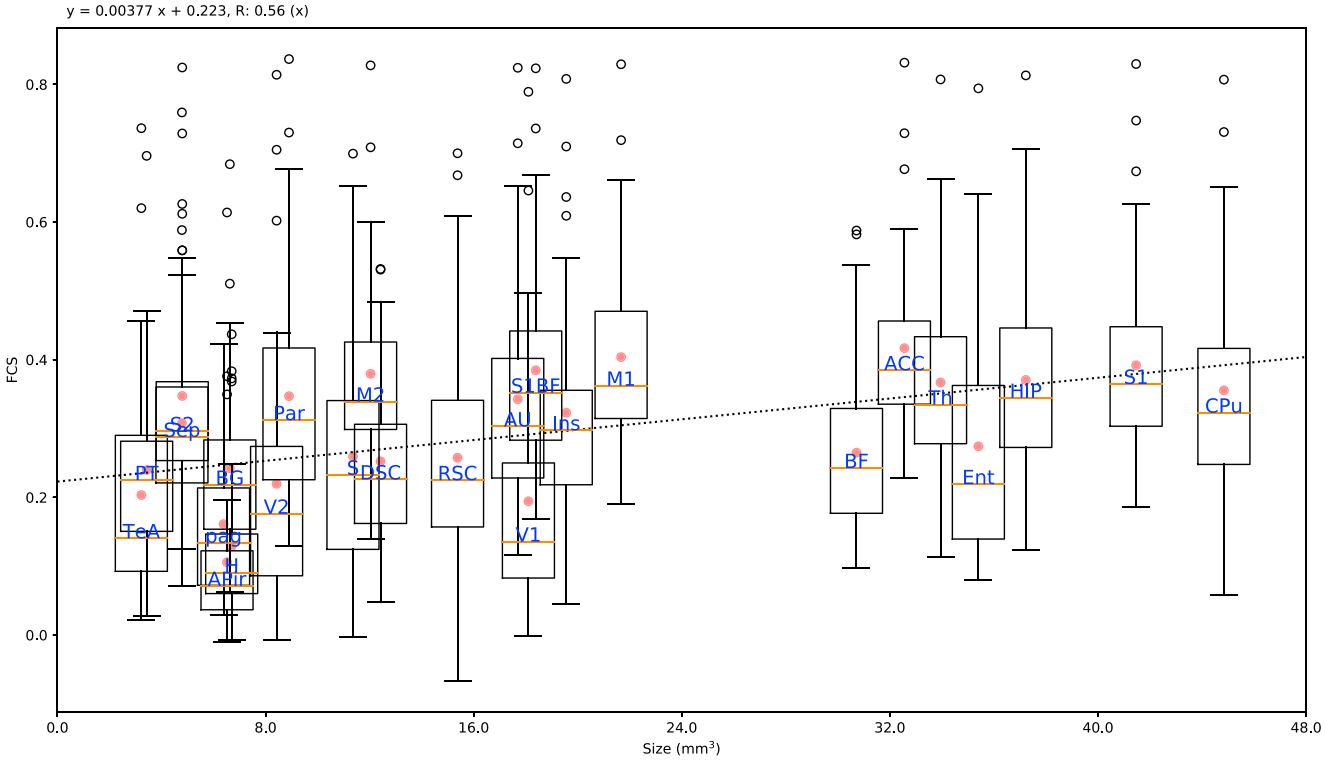


**Fig. H.15.** FCS distributions across rats versus area size. Each box corresponds to one area with left and right areas pooled together. The dotted line corresponds to a linear fit estimated from the average values of the areas represented with red dots.

Mean FCS across animals as a function of area size are shown Fig. H.15. There is a medium correlation ($R = 0.56$, $p < 0.01$) between the area size and the FCS. The slope between these two variables is weak (0.0035 per $mm^3$) and the high variability of the distributions indicates a low influence of the size of the area on FCS.

*Appendix H.3. Influence of distances on pairwise correlations*

The distributions of pairwise correlations in function of pairwise distances between areas are proposed in Fig. H.16 for each rat in each group (top) and for all rats in groups (bottom). Significant correlations are values above thresholds represented with black lines. The distributions are homogeneous within groups except for some individuals, in particular in the Iso groups. Values of correlations above thresholds are observed for all pairwise distances, even at long distances, except for dead rats were only few spurious values are observed at short distances. This indicates that long range correlations in all groups are observed.

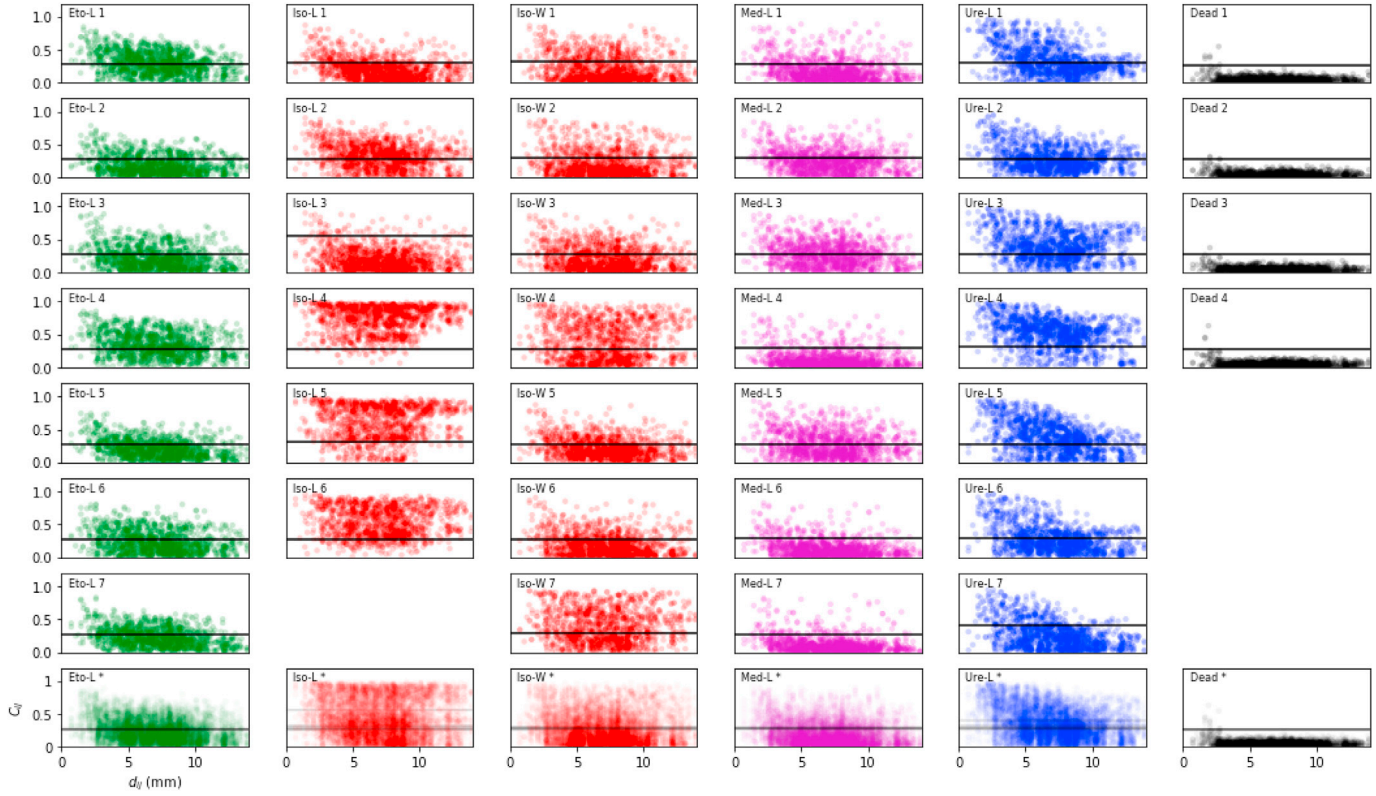


**Fig. H.16.** Correlations between pairs of areas in function of distances between them. Scatters are given for each rat in each group and the total distribution is given in the bottom row indicated by *.

*Appendix H.4. Influence of distances on pairwise FCS*

The distributions of FCS computed on significant correlations, versus the spatial locations of areas are given in Fig. H.17 for the different axis (LR, IS, AP) and in function of the Euclidean distances to the Bregma origin. An area is represented by the coordinates of its center of gravity. Anesthetized rats are pooled together to compute the box and whisker plots. Linear regressions between the median values of FCS and distances are also computed. FCS does not seem to be influenced by medio-lateral positions, even near ears (AU areas). There is a decrease of FCS in function of the position to the sensors put in evidence in the dorso-ventral (IS) representation. There is a decrease of FCS in function of the antero-posterior localization of the areas. These attenuations of FCS are put in evidence with the representation in function of the Euclidean distance to Bregma with a medium significant linear correlation ($R = -0.68$, $p = 3.2e\text{-}8$), a light slope ($-0.02$/mm), and a high variability of distributions for some areas between rats. For all these representations, ranges of values are more or less extended in function of areas.

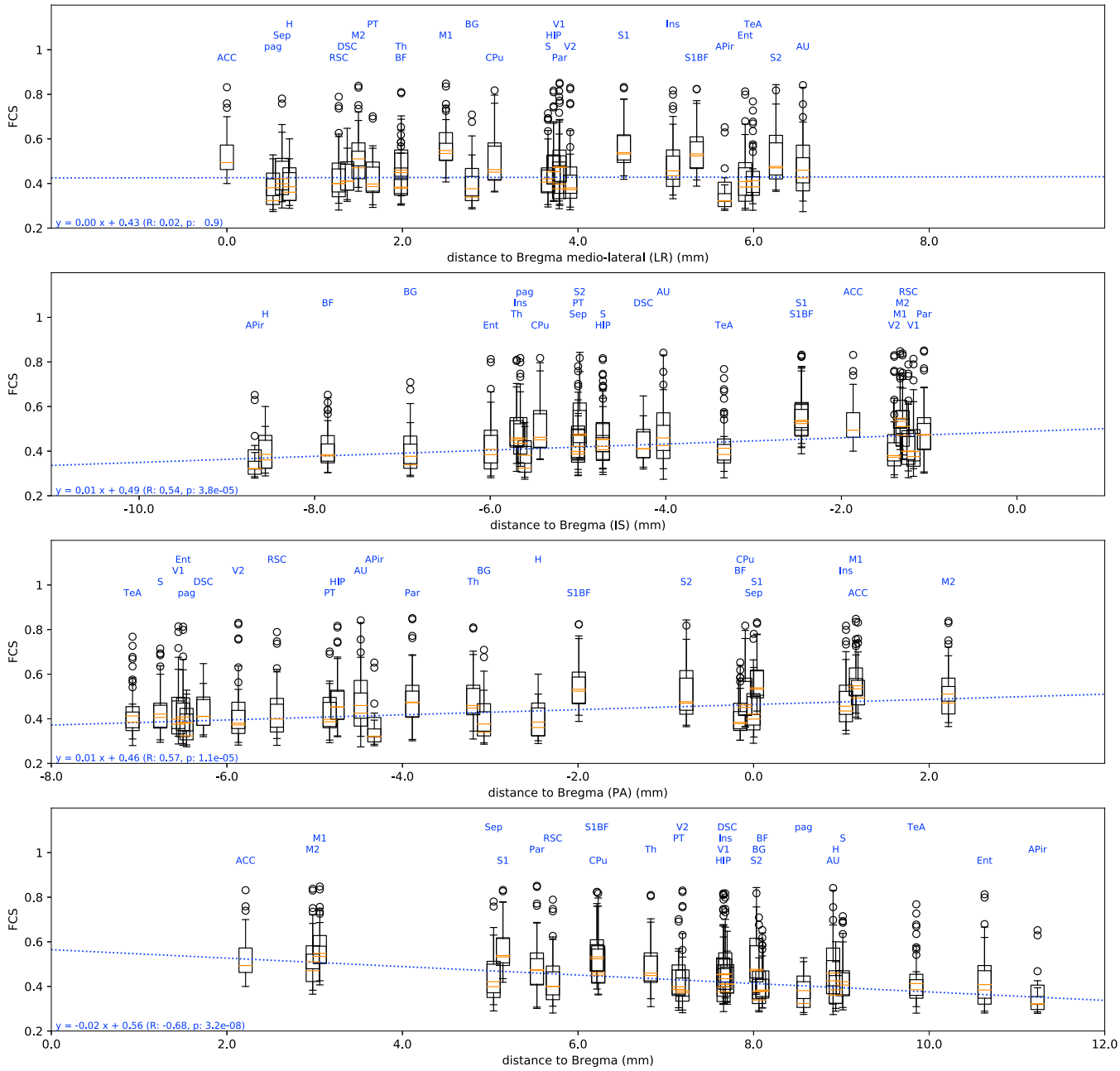


**Fig. H.17.** Distribution of FCS versus spatial position of areas. The origin Bregma is at (0, 0, 0) in the LR, IS, AP coordinate system. A linear regression is fitted with median values of FCS. a) For medio-lateral positions (LR axis). b) For dorso-ventral positions (IS axis). c) For antero-posterior positions (PA axis). d) For Euclidean distances to Bregma.

*Appendix H.5. Average matrices per group*

Average matrices per group of the significant connections are computed. Representations using graphs with nodes represented by the center of gravity of each area, on the 3 projections LR, IF, AP, are proposed in Fig. I.38a. Edges are plotted one over the other with the lowest values plotted first and the highest ones last. Different colors are also retained to show highest connected areas. Highest connections are more or less different from one group to another. All areas are connected on the anesthetized groups except one for Eto-L. Few edges are observed on the Dead group and correspond to edges between close areas in the anatomic template. The average matrices obtained with at least significant values from 4 animals are also represented as graphs in Fig. I.38b. Connections are enhanced, with enhanced differences between groups. No connections are persistent in the Dead group. The number of significant values obtained on each connection is displayed in Fig. I.38c, where a probability of 1 indicates that all rats of the group have this connection significant. Stable networks within groups are enhanced.

The observations that can be made on average graphs across group in Fig. I.38 may also be observed on individual graphs (Fig. I.32 to Fig. I.37):

- For Eto-L, there is a widespread fronto-parietal complex associating frontal and inter-hemispheric sensory communities, with shared connections between left and right cortical areas. The connection with a large subcortical area is preserved with an important role of the thalamus.

- For Iso-L, regarding cortical areas, there are widespread fronto-parietal, ipsi- and inter-hemispheric communities containing the motor area in one hemisphere connected to its contralateral sensory area. There are wide subcortical communities associated to cortical communities. The cortical-subcortical connections mediated by Th and HIP are part of the highly correlated coefficients, and indicate connections with visual areas.
- For Iso-W, only four communities are put in evidence: a widespread cortical, well-connected module; an isolated subcortical interhemispheric Th–HIP; An ACC-CPu module well connected to cortical areas and an Ins module, more or less present in individuals.
- For Med-L, there is a widespread inter-hemispheric fronto-parietal community connected to an inter-hemispheric sensory module connected to HIP and RSC. The subcortical inter-hemispheric communities is weakly connected to cortical areas.
- For Ure-L, large left and right cortical fronto-parietal communities are shown. These two cortical left-right communities are weakly connected. Two subcortical left-right communities are also disconnected. There are few connections between these cortical-subcortical communities. The connections between cortical-subcortical communities, left and right communities are weak. The role of ACC seems weaker than in other groups.

*Appendix H.6. Comparison of graphs at different densities*

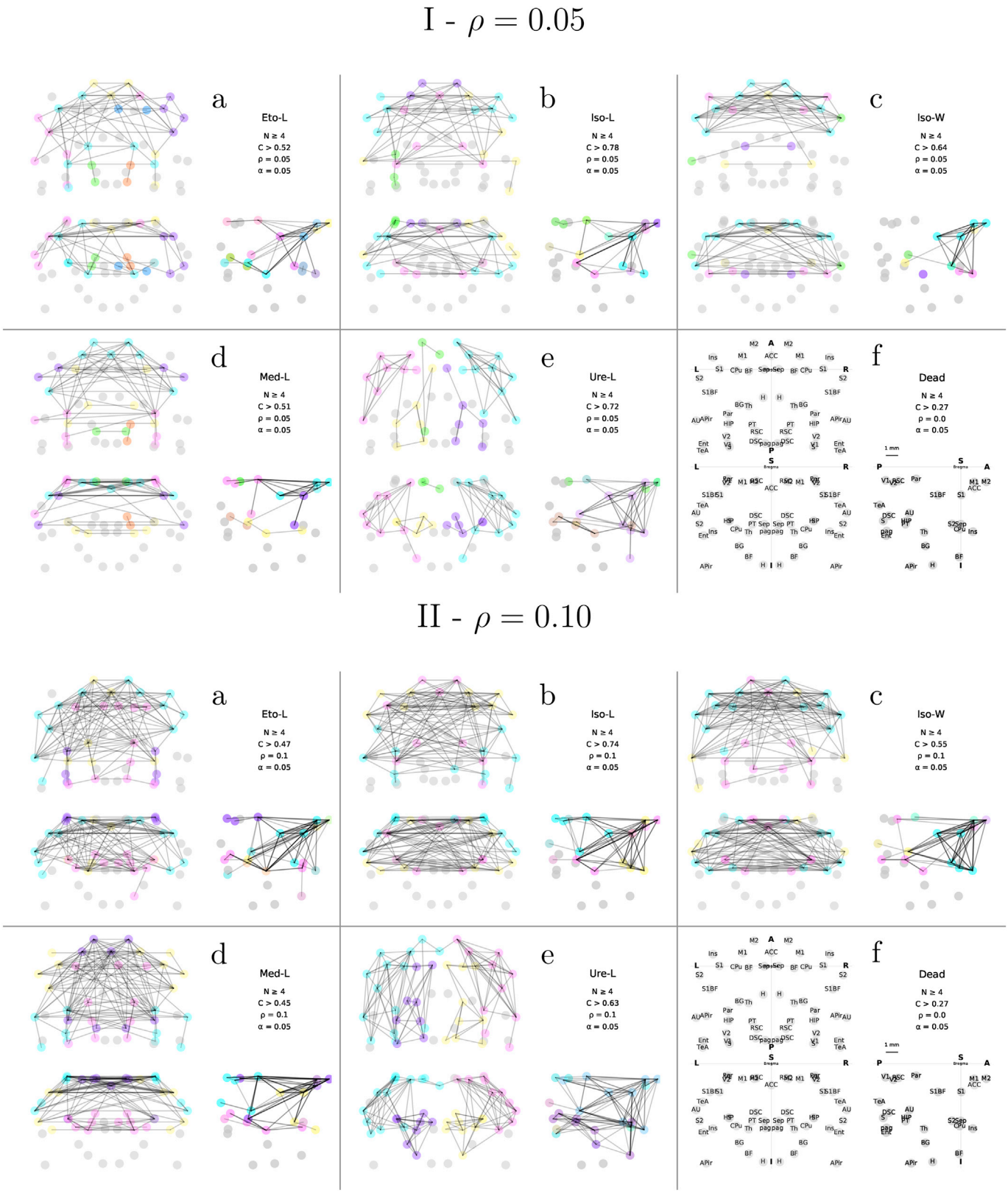


**Fig. H.18.** Graphs based on the average correlation matrices for each group at two density: I) by taking the 63 most significant correlated values (density = 0.05) with at least 4 animals; II) by taking the 127 most significant correlated values (density = 0.1) with at least 4 animals.

Table H.3
Distributions of connections per group.

| | ACC | inter | intra | c – c | s – s | c – s |
|---|---|---|---|---|---|---|
| $\rho = 0.05$ | | | | | | |
| Eto-L | 16 ± 0 | 27 ± 2 | 55 ± 1 | 48 ± 3 | 17 ± 3 | 17 ± 2 |
| Iso-L | 11 ±1 | 40 ±1 | 48 ± 2 | 73 ±4 | 11 ±5 | 2 ± 1 |
| Iso-W | 19 ± 0 | 42 ± 1 | 38 ± 1 | 65 ± 3 | 9 ± 3 | 4 ± 1 |
| Med-L | 13 ±1 | 41 ±1 | 44 ±1 | 73 ±3 | 10 ± 2 | 2 ± 0 |
| Ure-L | 2 ± 0 | 1 ± 0 | 96 ± 1 | 56 ± 4 | 29 ± 4 | 11 ± 3 |
| $\rho = 0.1$ | | | | | | |
| Eto-L | 13 ± 0 | 34 ± 2 | 51 ± 1 | 40 ± 1 | 17 ± 2 | 27 ± 1 |
| Iso-L | 9 ± 0 | 42 ± 1 | 48 ±2 | 66 ±5 | 15 ±5 | 8 ±1 |
| Iso-W | 14 ± 0 | 43 ± 1 | 42 ± 1 | 56 ± 2 | 13 ± 4 | 16 ± 2 |
| Med-L | 12 ± 0 | 41 ± 0 | 46 ± 0 | 61 ± 3 | 16 ± 3 | 10 ± 1 |
| Ure-L | 3 ± 0 | 4 ± 1 | 92 ± 2 | 45 ± 5 | 31 ± 4 | 19 ± 2 |
| Full | 4 | 49 | 47 | 30 | 18 | 48 |

Mean ± SEM are given in %. Notations: interhemispheric (inter), intrahemispheric (intra), cortex (c), subcortical (s).

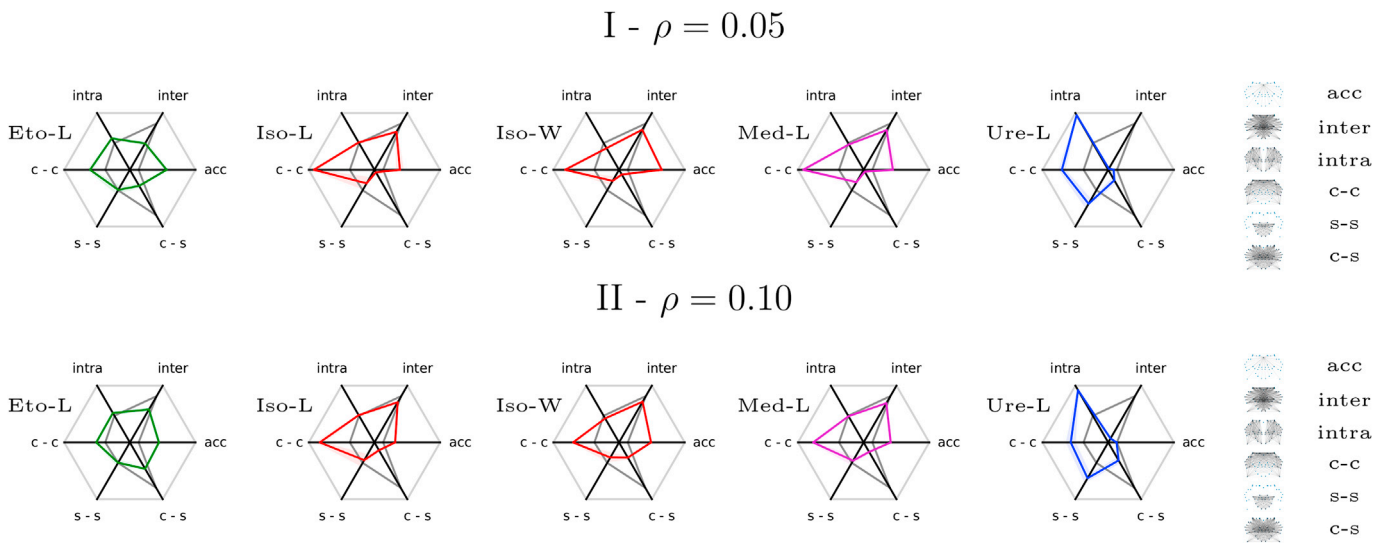


**Fig. H.19.** Radar plots for the distributions of connections for a) ρ = 0.05 and b) $\rho = 0.1$. The gray curve corresponds to the fully connected graph (Full).

Distributions of connections per wide areas are given in Table H.3 and Fig. H.19 for the two densities $\rho = 0.05$ and $\rho = 0.1$. The comparison of values between densities indicates that from the low density graphs at $\rho = 0.05$ to the dense one at $\rho = 0.1$, the ratio of c-s connections increased for all groups, especially for Med-L and Iso-W, towards the ratio of the complete graph. For these groups, the c-c balance decreases and the s-s balance increases. This is also observed on the global patterns observed in Fig. H.18 for $\rho = 0.05$ and $\rho = 0.1$. In vivo graphs differ from the theoretical full-graph, which has a small ACC contribution (4%), and equivalent inter- and intra-hemispheric connections. In vivo, the contribution of ACC is comparable across groups (between 9 and 14%), except for Ure-L for which it barely contributes (3%) (values given for the density $\rho = 0.1$ but same comparisons can be drawn from $\rho = 0.05$). Ure-L also differs by the fact that most connections (92%) are intra-hemispheric rather than inter-hemispheric (4%). For the other groups, the balance between inter-hemispheric and intra-hemispheric proportions are comparable with less intra-hemispheric connections for the Eto-L group. For this group, the cortical-subcortical proportion is the highest one (27%), to the detriment of the cortical-cortical proportion (the lowest one). Iso-L shows the lowest proportion of subcortical-cortical connections (8%) and the highest proportion of cortical connections (66%) and is comparable with Iso-W and Med-L. A graphical comparison using radar profiles is proposed in Fig. H.19, that highlights the similarities and dissimilarities between groups.

## Appendix I. Supplementary figures

*Appendix I.1.1*

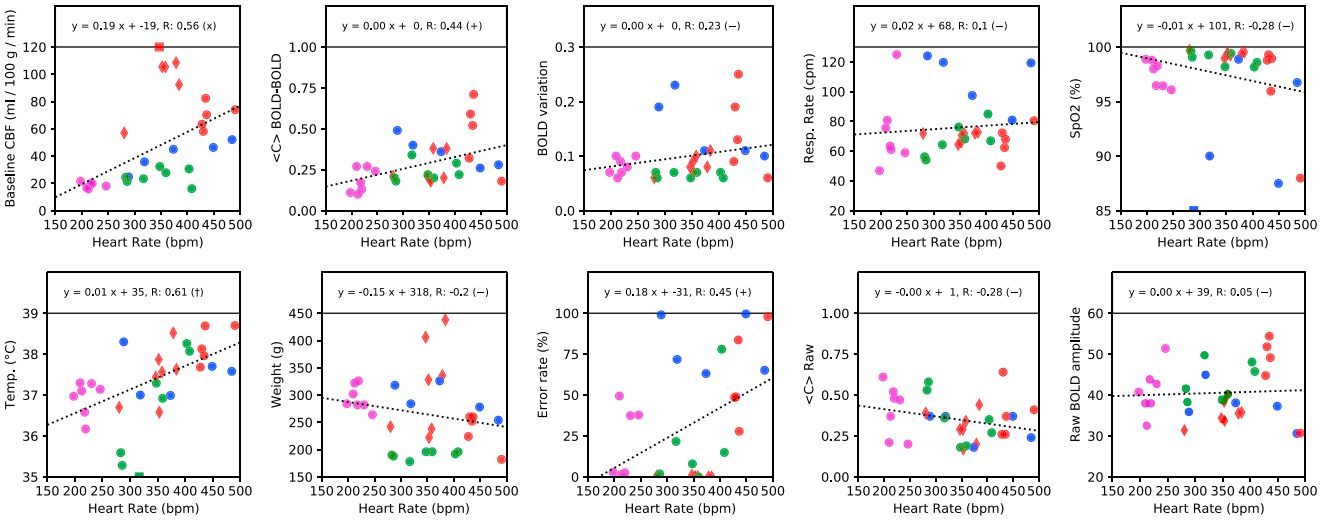


**Fig. I.20.** Distributions of variables per group with scatter plots as a function of HR. Outliers are marked with a square. A linear trend is computed without the outliers. Circle: long evans, Diamond: wistar; Red: isoflurane, Green: etomidate, Magenta: medetomidine, Blue: urethane.

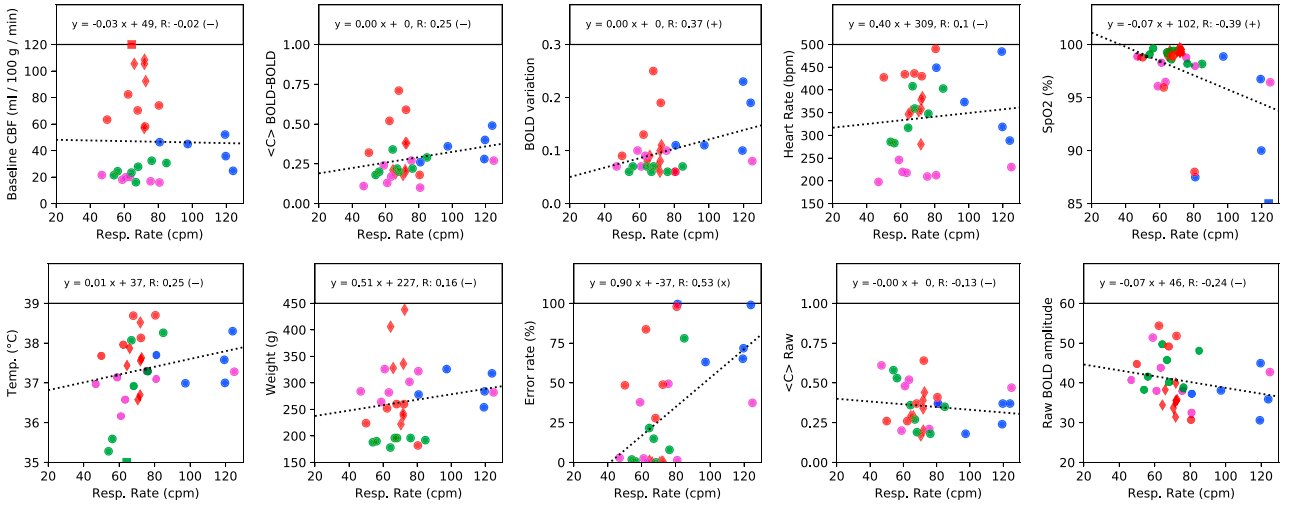


**Fig. I.21.** Distributions — scatter plots — as a function of RR.

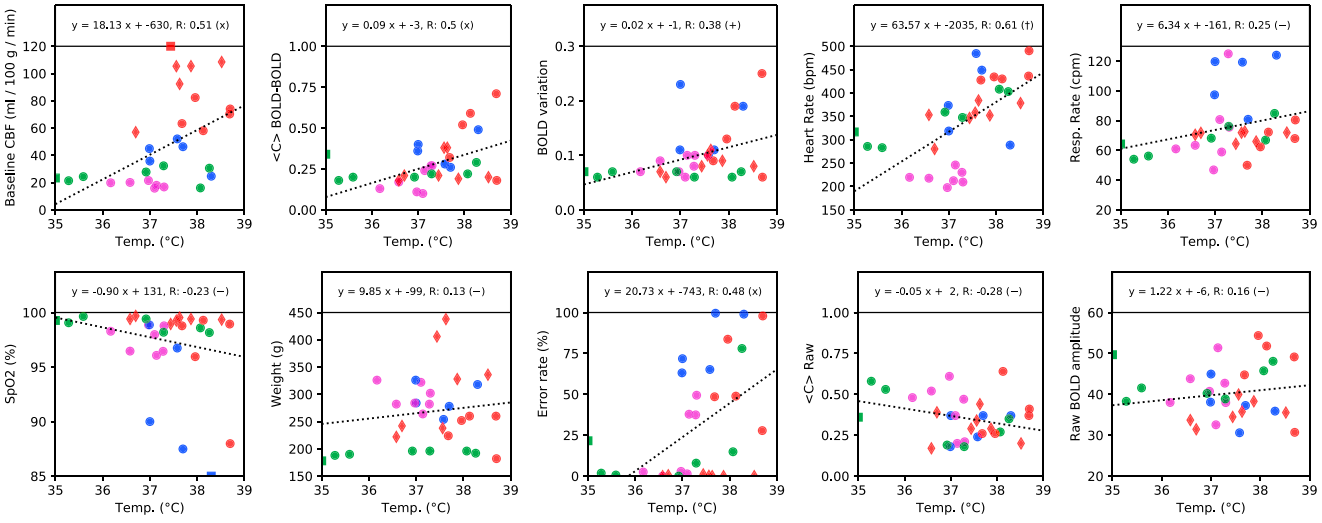


**Fig. I.22.** Distributions — scatter plots — as a function of Temp.

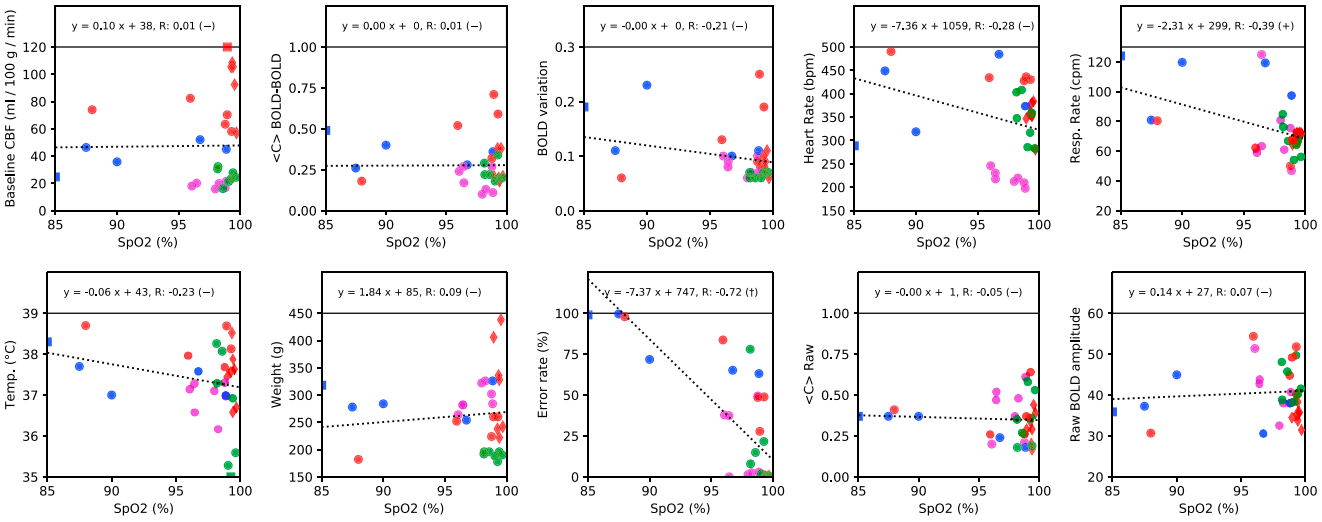


**Fig. I.23.** Distributions — scatter plots — as a function of SpO2.

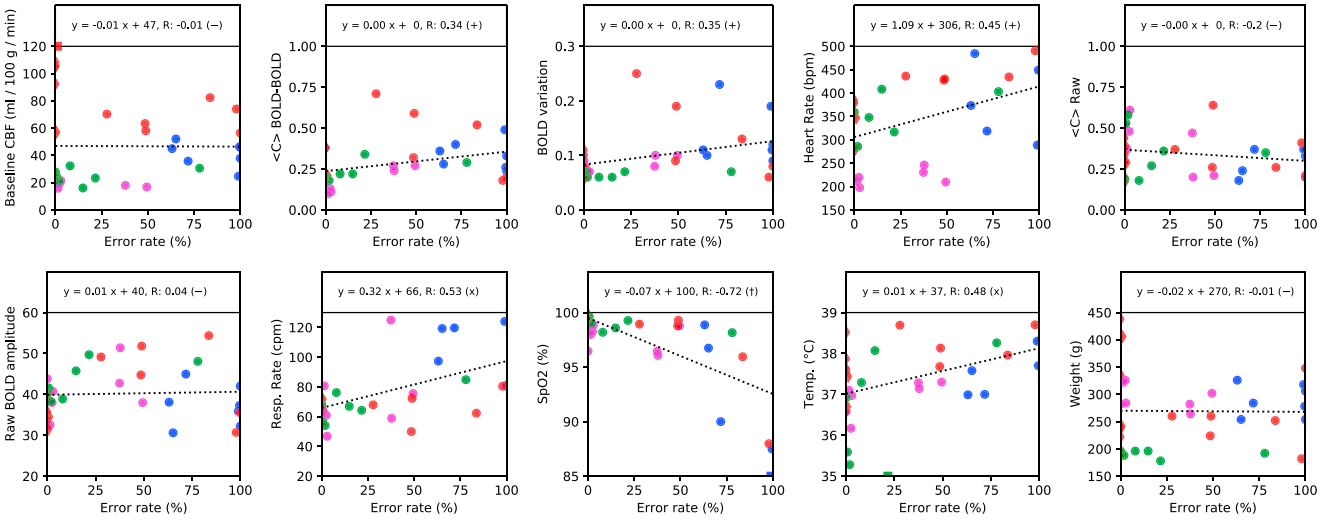


**Fig. I.24.** Distributions — scatter plots — as a function of Error rate.

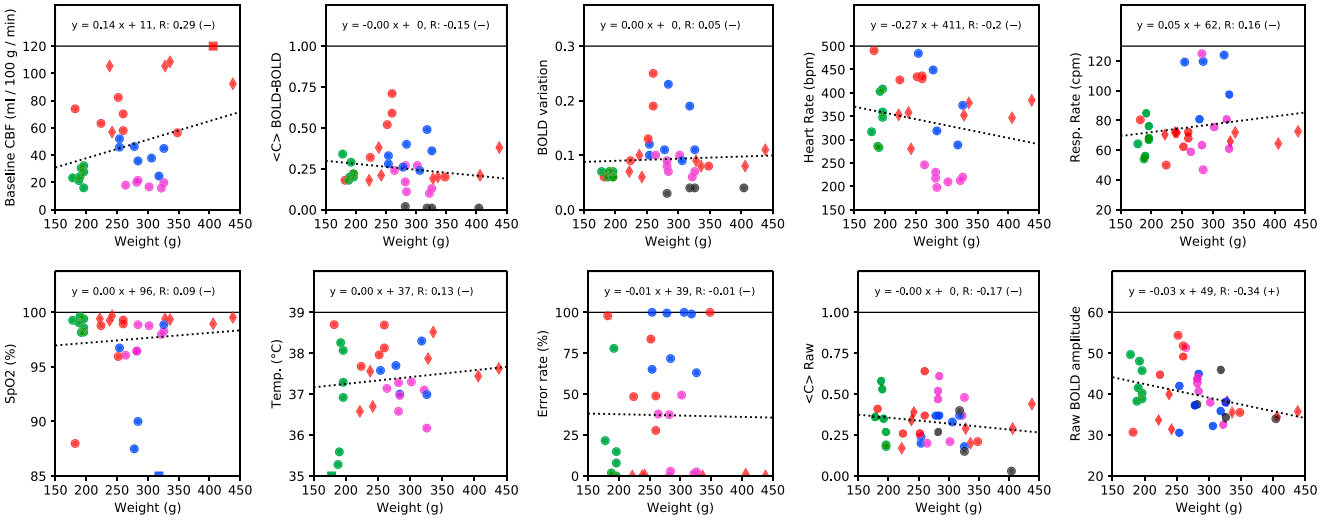


**Fig. I.25.** Distributions — scatter plots — as a function of Weight.

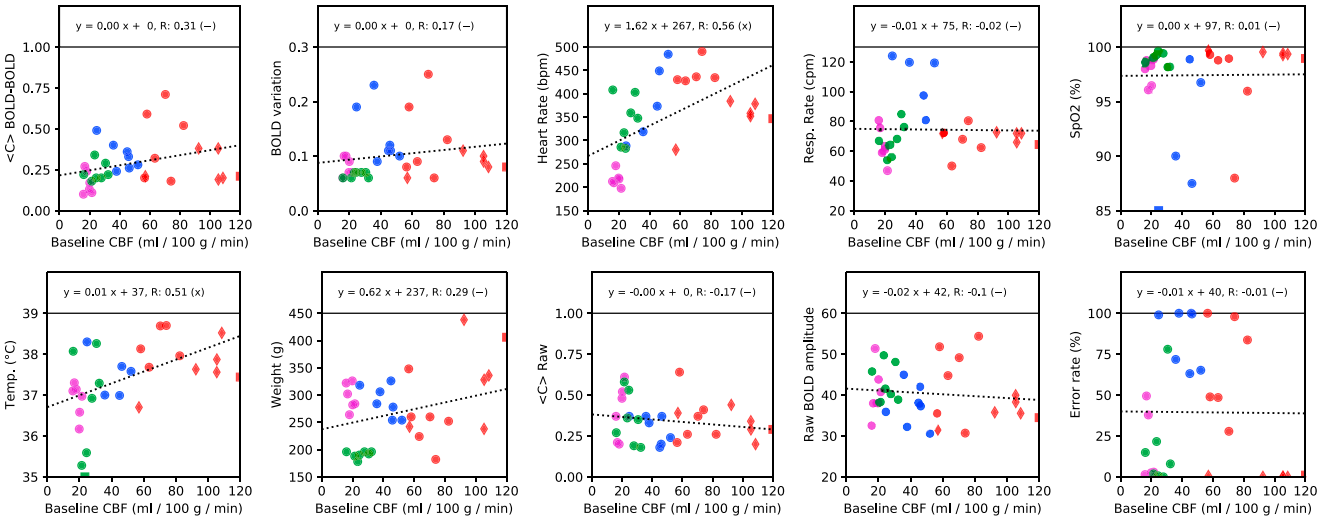


**Fig. I.26.** Distributions — scatter plots — as a function of CBF.

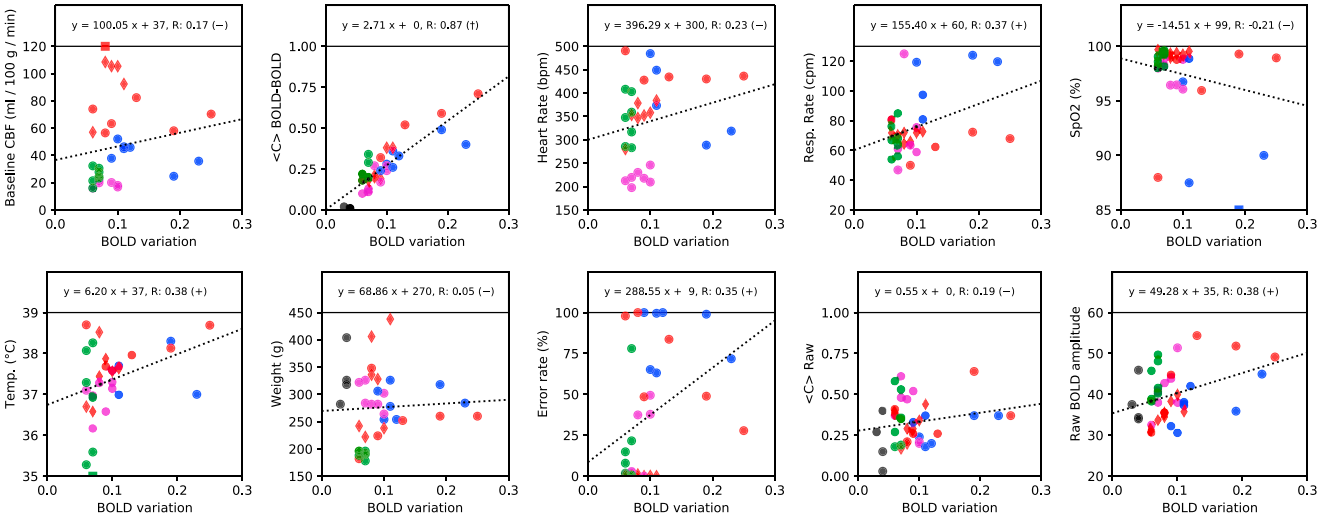


**Fig. I.27.** Distributions — scatter plots — as a function of BOLD variations.

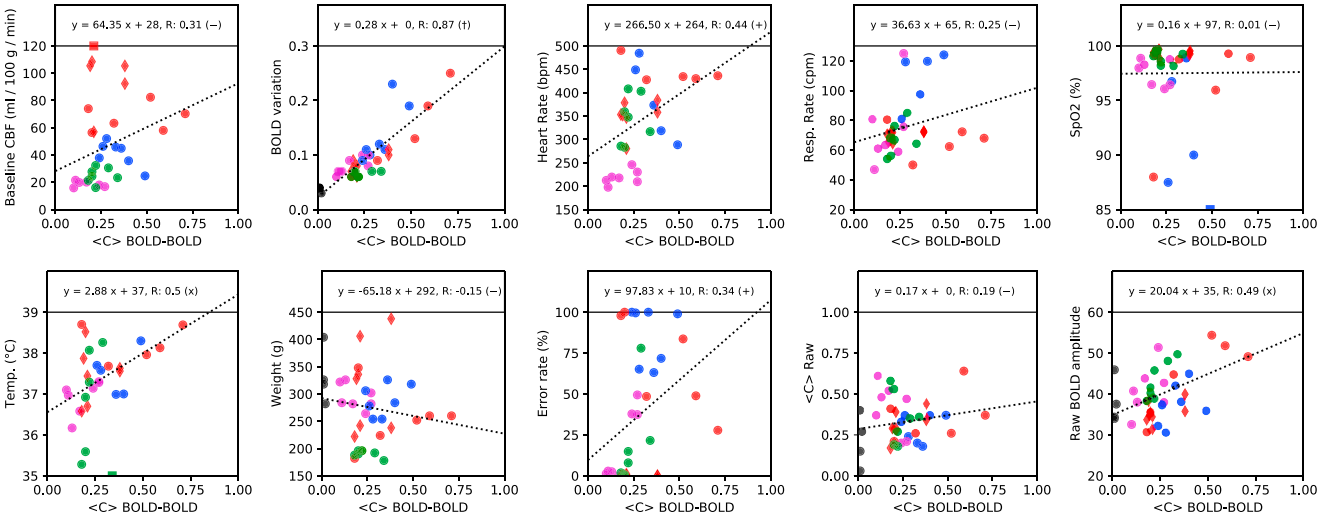


**Fig. I.28.** Distributions — scatter plots — as a function of average correlations $\langle C \rangle$.

*Appendix I.2.2*

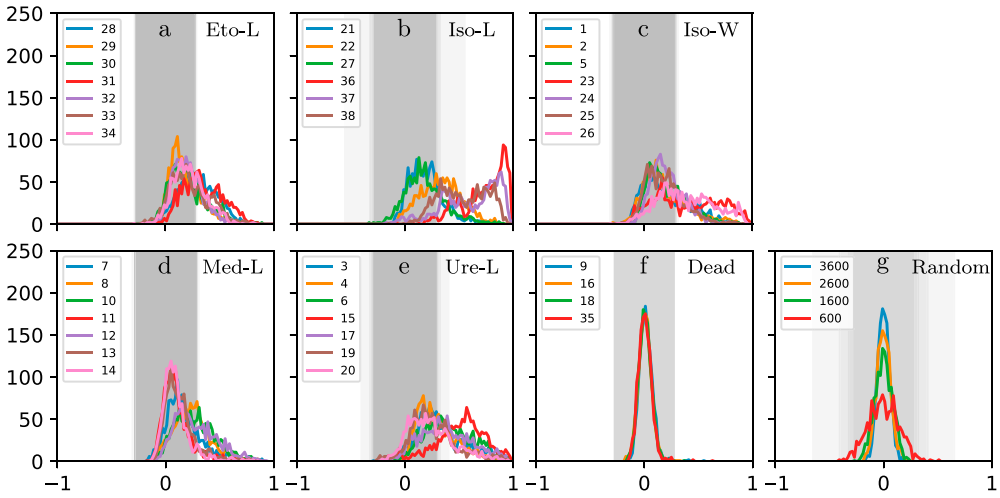


**Fig. I.29.** Histograms of the BOLD-BOLD correlations per group in frequency band cD4. Histograms are estimated on 100 bins between [-1, 1]: a) – f) per anesthetic and for the Dead group with one color per animal; g) for simulated signals obtained with random values with the same number of areas and signal processing methods with different number of samples given in legend. The gray range represents the two-sided distribution of correlations below significance level given by the Bonferroni threshold.

*Appendix I.3.3*

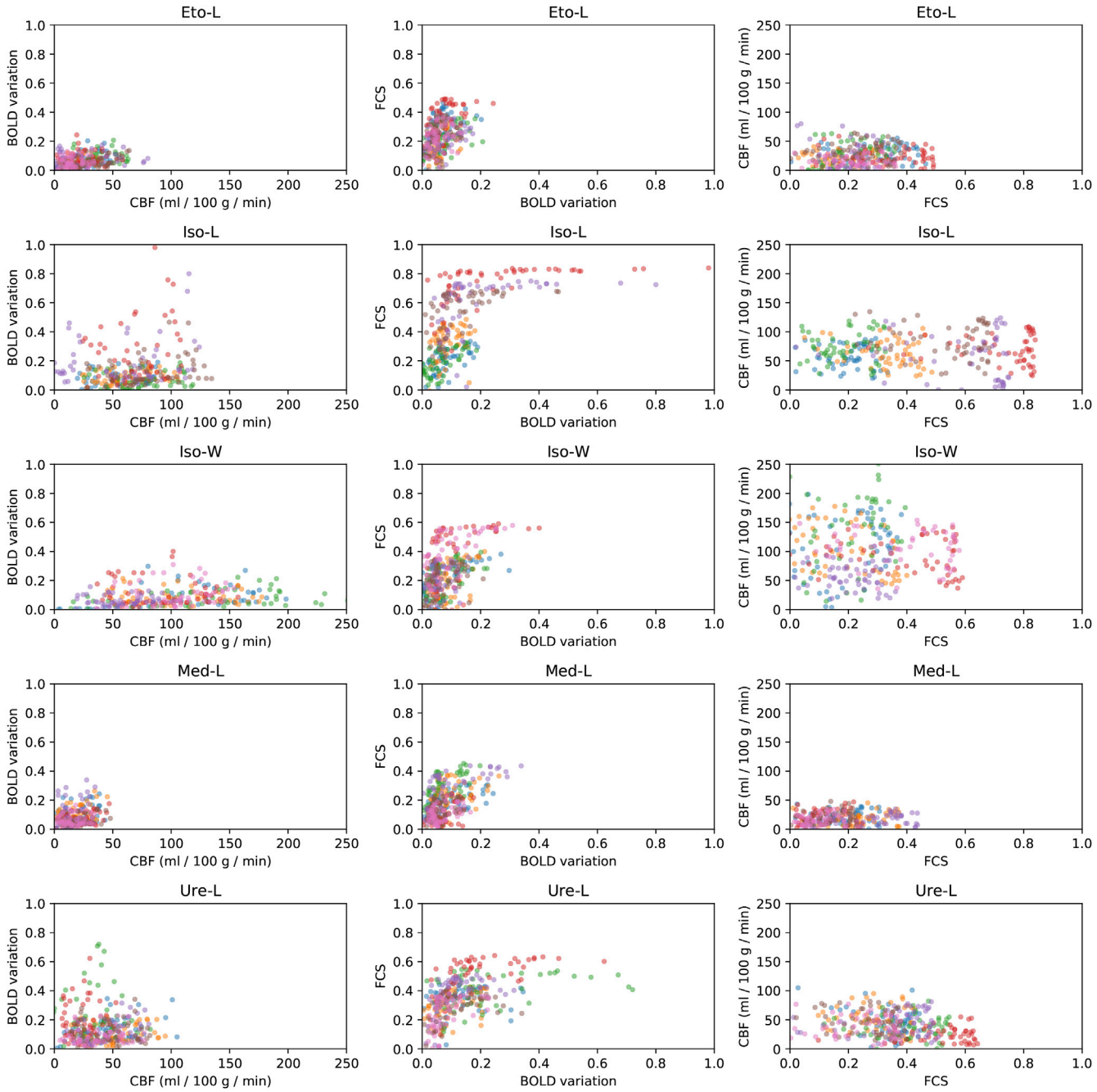


**Fig. I.30.** Scatter plots per group between baseline CBF, BOLD variation and FCS. Dots with the same color belong to the same animal.

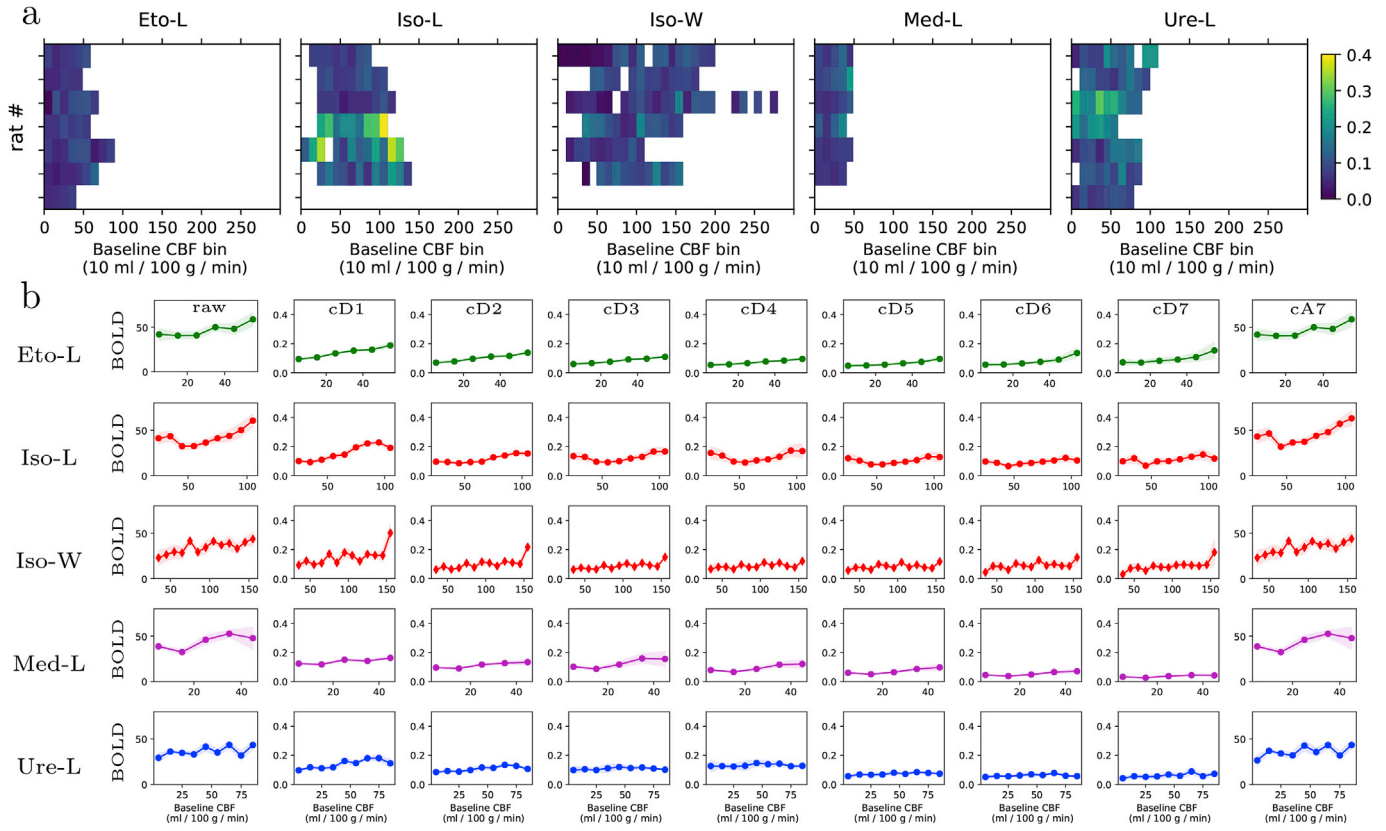


**Fig. I.31.** Influence of population and frequency bands. a) BOLD variation as a function of CBF, for each anesthetized group. Each row represents one animal. BOLD variation is coded using the color scale on the right. b) BOLD amplitude for raw BOLD signal or variations versus CBF per frequency band and anesthetized group. BOLD variation in the cD4 band is presented in the main paper.

*Appendix I.4.4*

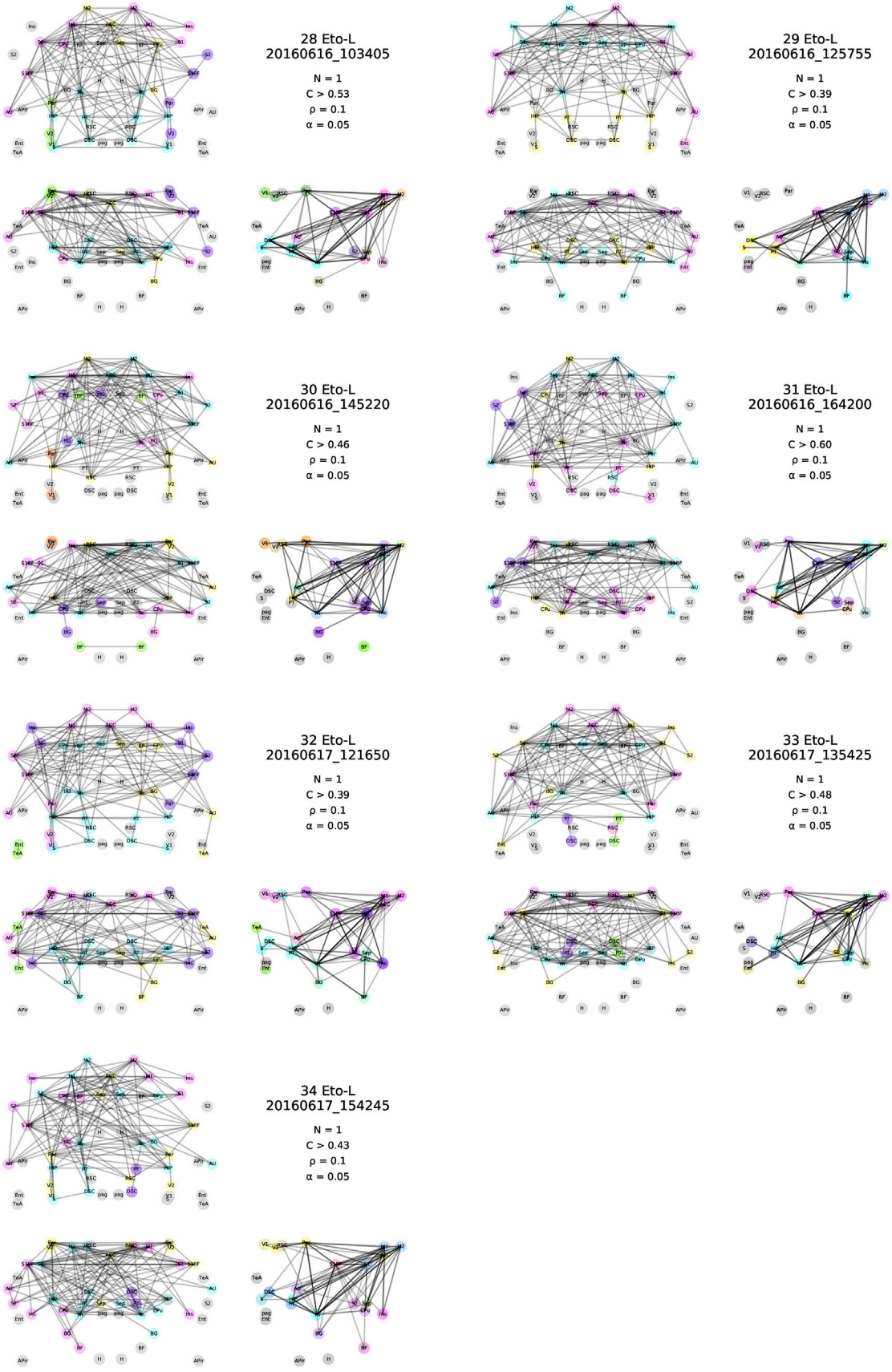


**Fig. I.32.** Individual graphs - Eto-L

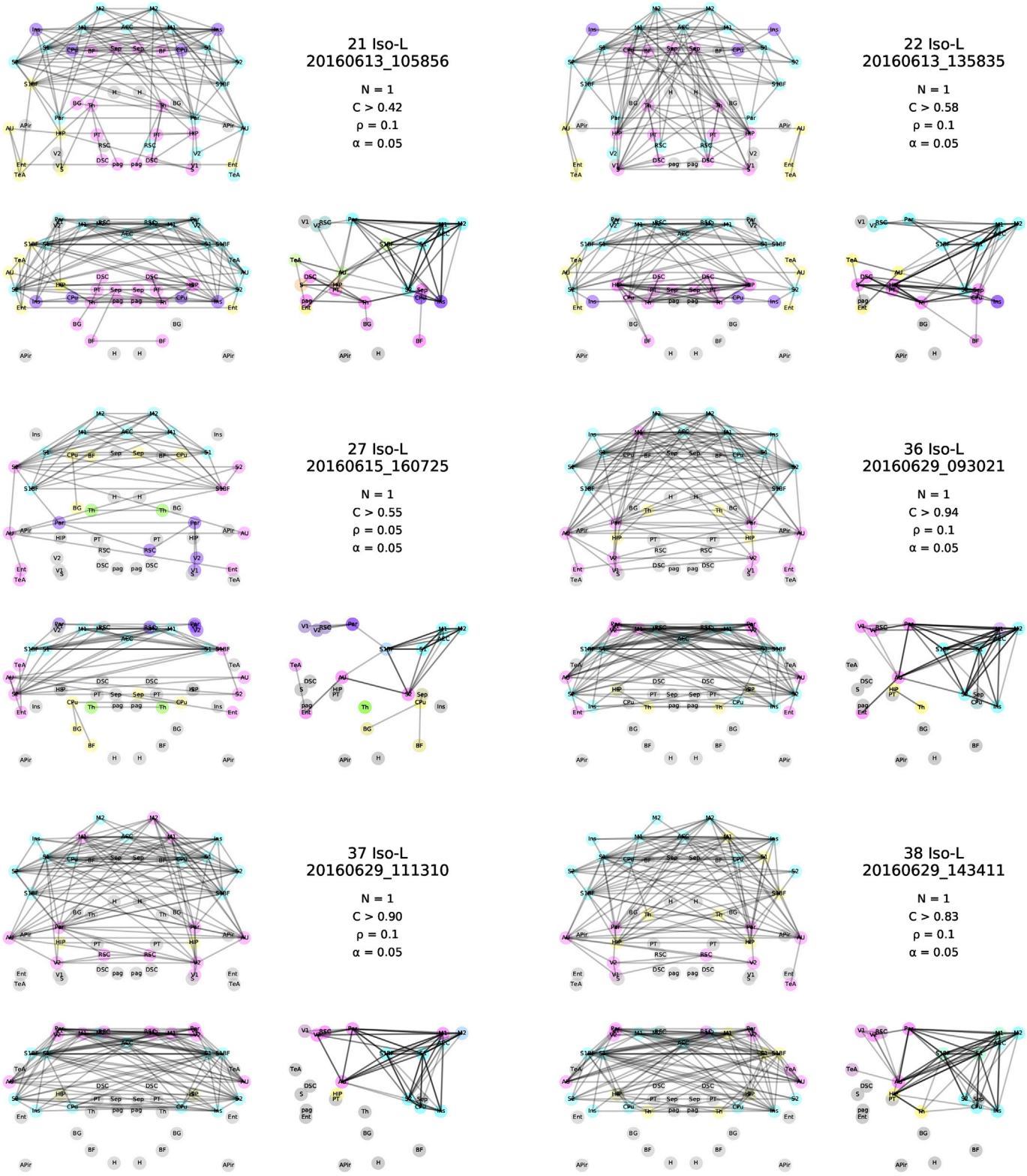


**Fig. I.33.** Individual graphs - Iso-L

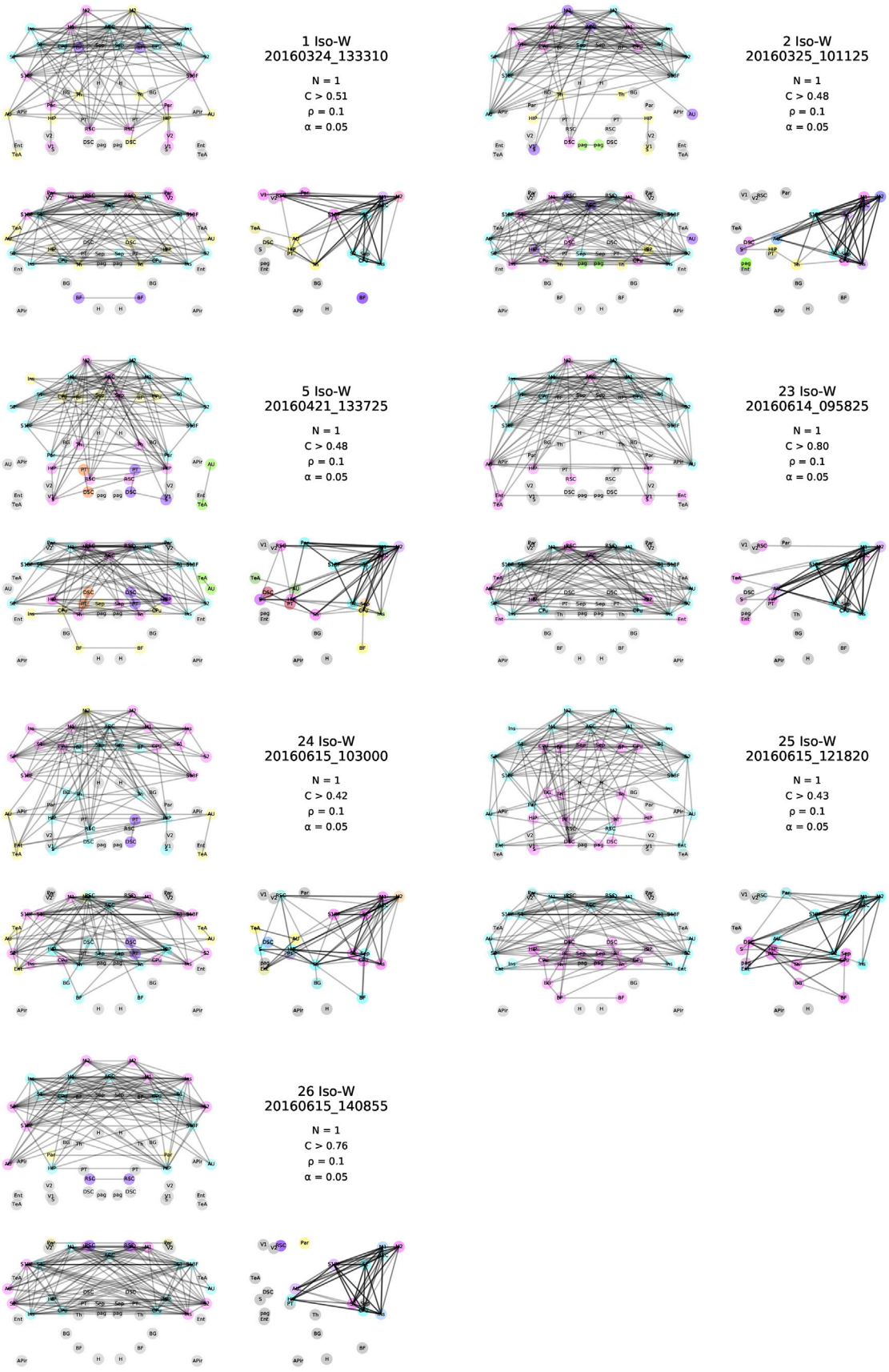


**Fig. I.34.** Individual graphs - Iso-W

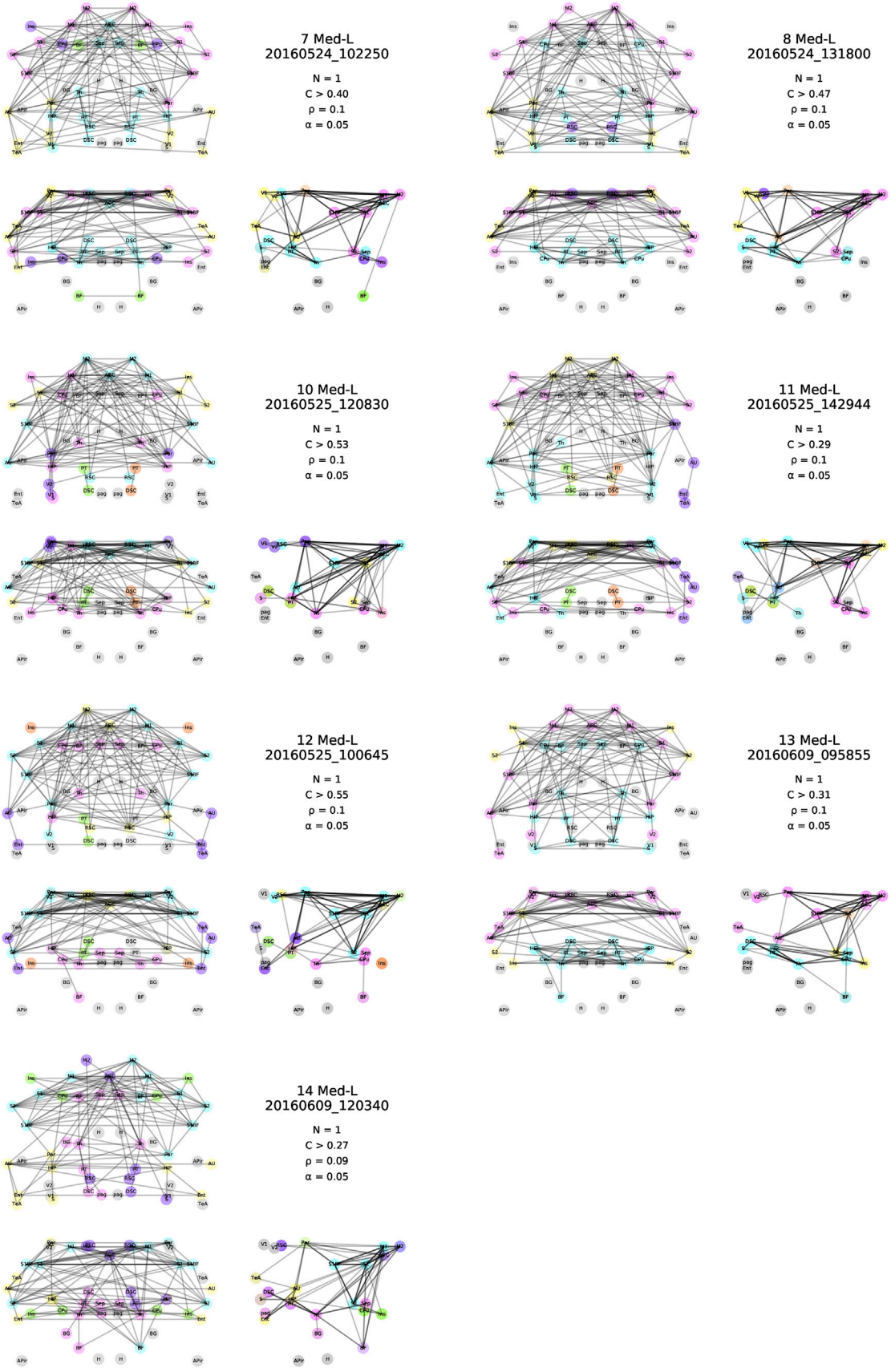


**Fig. I.35.** Individual graphs - Med-L

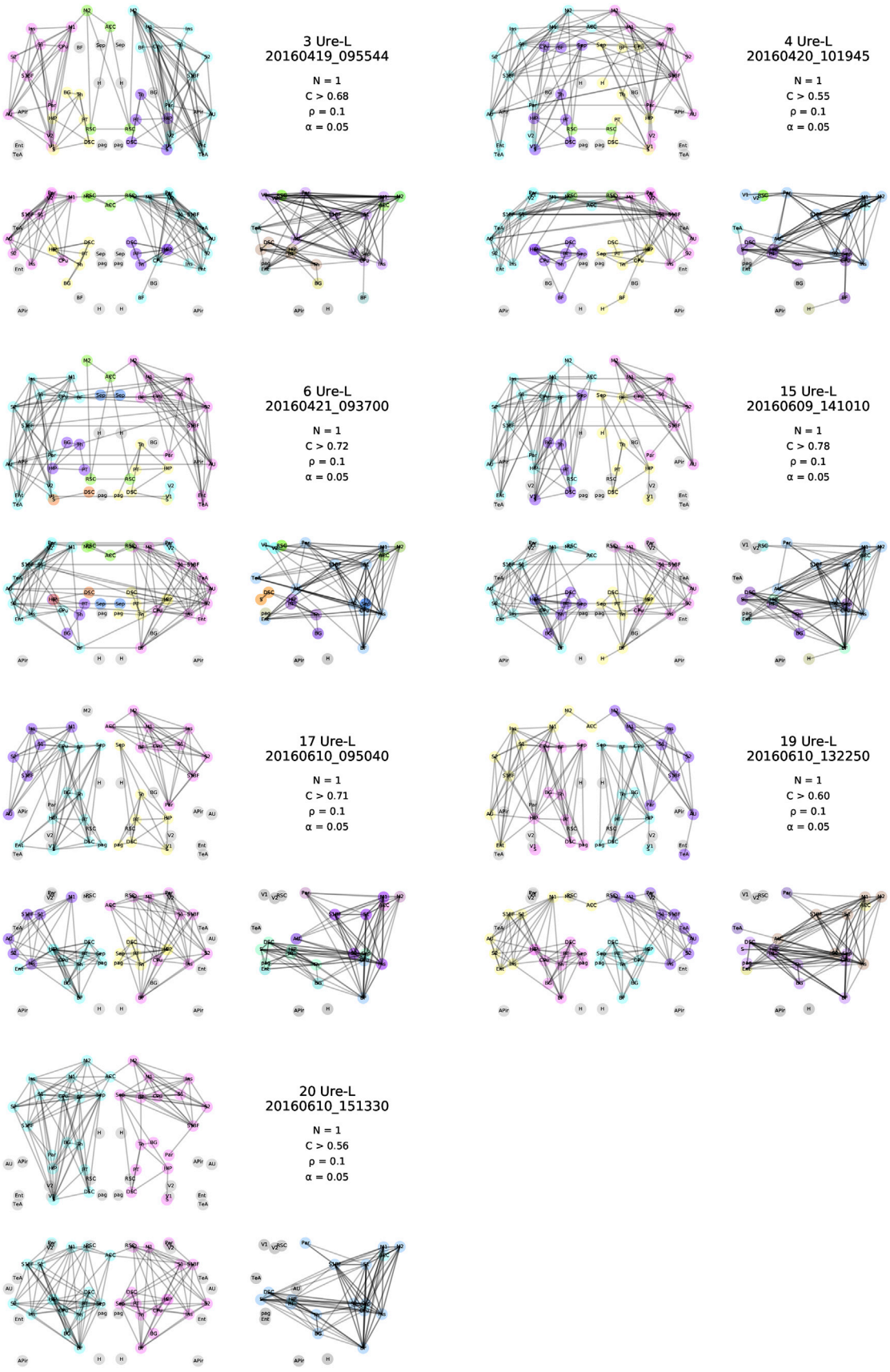


**Fig. I.36.** Individual graphs - Ure-L

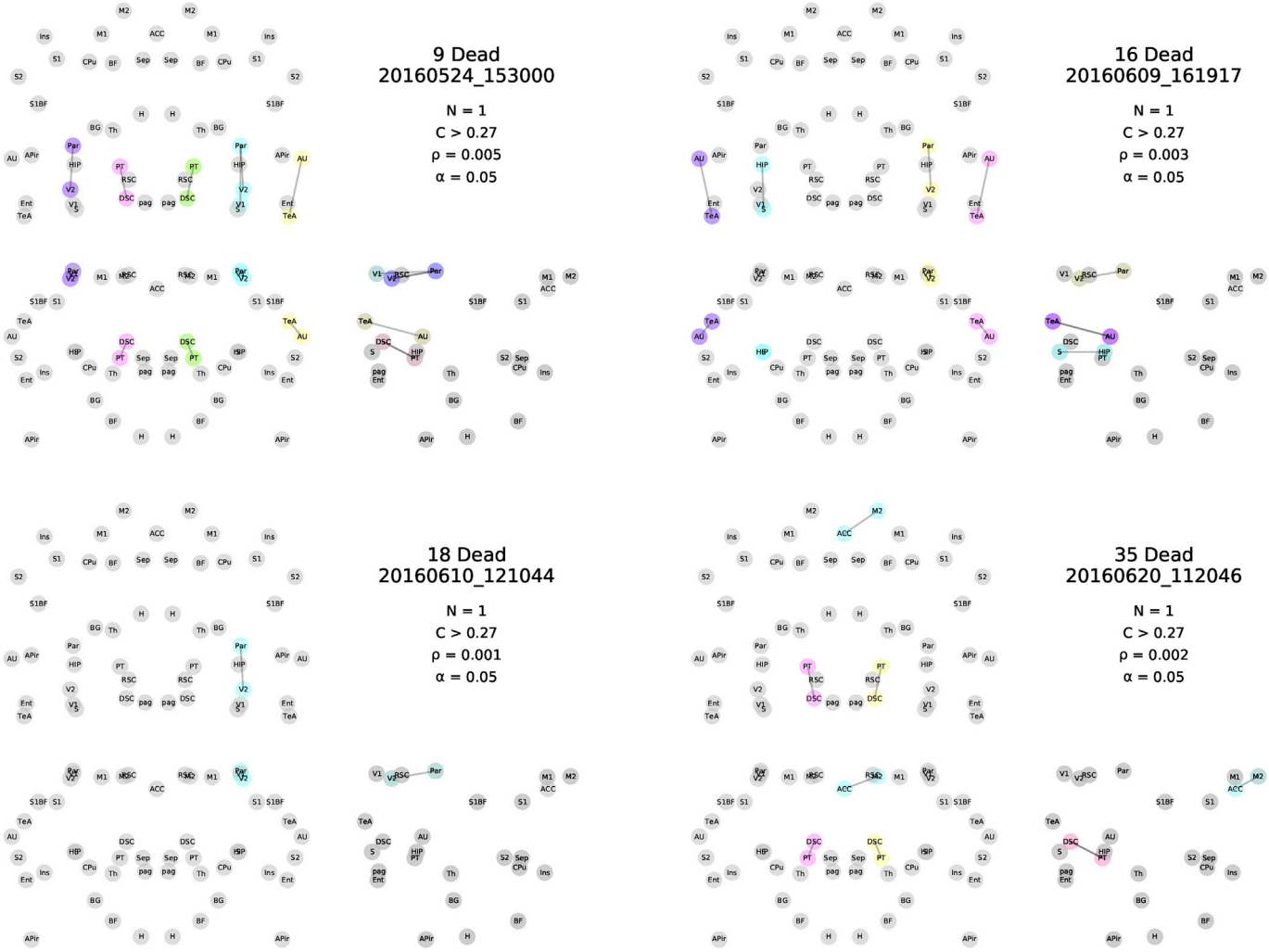


**Fig. I.37.** Individual graphs - Dead

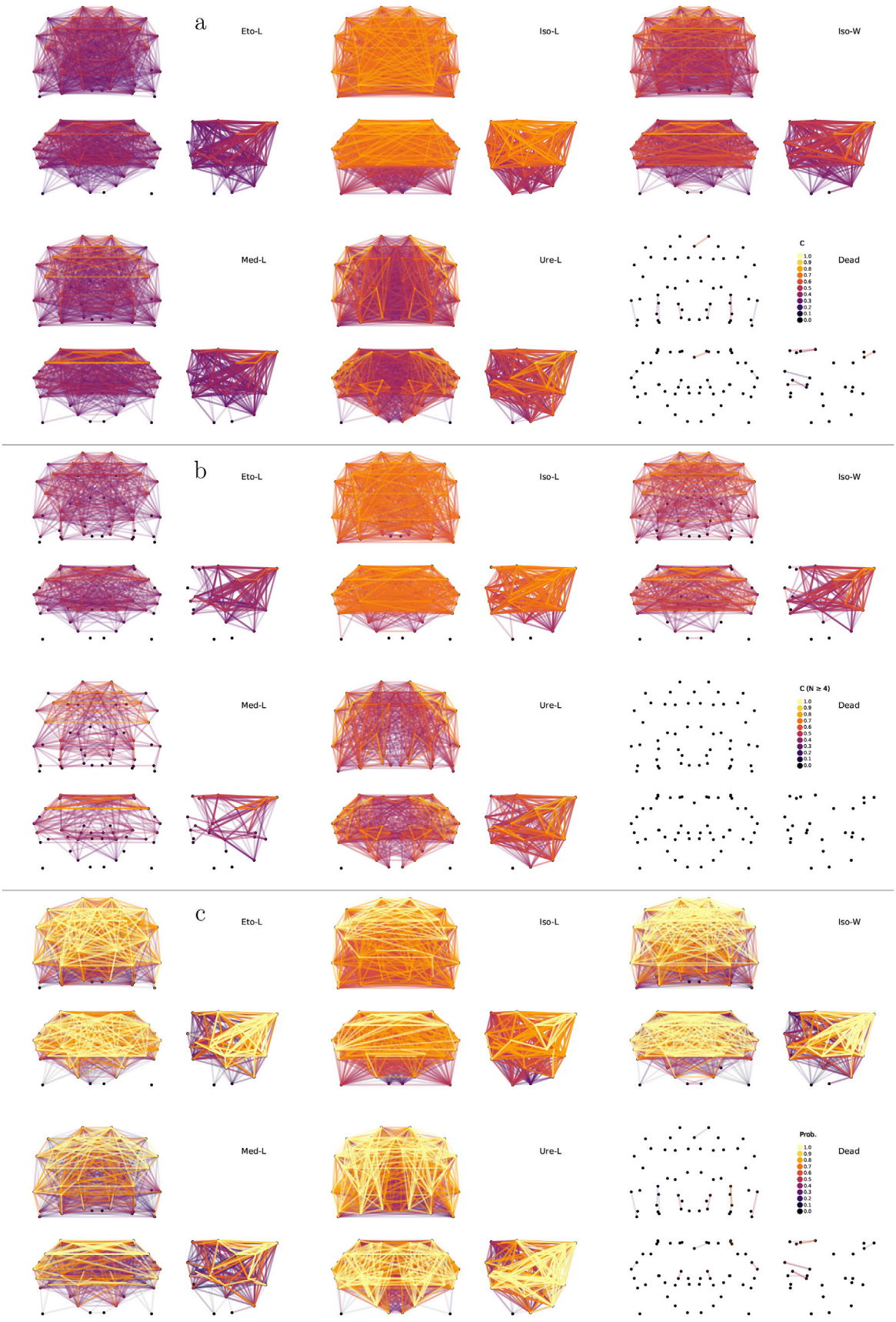


**Fig. I.38.** Sorted Full Graph - Graphs with superimposed edges with the lowest on the background an the highest on the foreground. In these graphs, all available statistically significant edges are plotted for: a) average correlations; b) average correlations with at least 4 animals; c) probability of significant connections. Colors represent weights truncated at one decimal.

## References


Achard, S., Salvador, R., Whitcher, B., Suckling, J., Bullmore, E., 2006. A resilient, low-frequency, small-world human brain functional network with highly connected association cortical hubs. J. Neurosci. 26, 63–72. https://doi.org/10.1523/JNEUROSCI.3874-05.2006.

Akata, T., 2007. General anesthetics and vascular smooth muscle direct actions of general anesthetics on cellular mechanisms regulating vascular tone. Anesthesiology 106, 365–391. https://doi.org/10.1097/00000542-200702000-00026.

Alsop, D., Detre, J., Golay, X.e. a., 2015. Recommended implementation of arterial spin labeled perfusion mri for clinical applications: a consensus of the ISMRM perfusion study group and the european consortium for ASL in dementia. Magn. Reson. Med. 73, 102–116. https://doi.org/10.1002/mrm.25197.

Ashburner, J., Barnes, G., Chen, C., Daunizeau, J., Flandin, G., Friston, K., Kiebel, S., Kilner, J., Litvak, V., Moran, R., et al., 2014. SPM12 Manual. Wellcome Trust Centre for Neuroimaging, London, UK. https://www.fil.ion.ucl.ac.uk/spm/doc/spm12_manual.pdf.

Baek, K., Shim, W.H., Jeong, J., Radhakrishnan, H., Rosen, B.R., Boas, D., Franceschini, M., Biswal, B.B., Kim, Y.R., 2016. Layer-specific interhemispheric functional connectivity in the somatosensory cortex of rats: resting state electrophysiology and fMRI studies. Brain Struct. Funct. 221, 2801–2815. https://doi.org/10.1007/s00429-015-1073-0.

Barrat, A., Barthelemy, M., Pastor-Satorras, R., Vespignani, A., 2004. The architecture of complex weighted networks. Proc. Natl. Acad. Sci. U.S.A. 101, 3747–3752. https://doi.org/10.1073/pnas.0400087101.

Bettinardi, R.G., Tort-Colet, N., Ruiz-Mejias, M., Sanchez-Vives, M.V., Deco, G., 2015. Gradual emergence of spontaneous correlated brain activity during fading of general anesthesia in rats: evidences from fMRI and local field potentials. Neuroimage 114, 185–198. https://doi.org/10.1016/j.neuroimage.2015.03.037.

Biswal, B., Zerrin Yetkin, F., Haughton, V.M., Hyde, J.S., 1995. Functional connectivity in the motor cortex of resting human brain using echo-planar MRI. Magn. Reson. Med. 34, 537–541. https://doi.org/10.1002/mrm.1910340409.

Chan, K.C., Fan, S.-J., Chan, R.W., Cheng, J.S., Zhou, I.Y., Wu, E.X., 2014. In vivo visuotopic brain mapping with manganese-enhanced MRI and resting-state functional connectivity MRI. Neuroimage 90, 235–245. https://doi.org/10.1016/j.neuroimage.2013.12.056.

Chen, L., Mishra, A., Newton, A.T., Morgan, V.L., Stringer, E.A., Rogers, B.P., Gore, J.C., 2011. Fine-scale functional connectivity in somatosensory cortex revealed by high-resolution fMRI. Magn. Reson. Imaging 29, 1330–1337. https://doi.org/10.1016/j.mri.2011.08.001.

Ciobanu, L., Reynaud, O., Uhrig, L., Jarraya, B., Le Bihan, D., 2012. Effects of anesthetic agents on brain blood oxygenation level revealed with ultra-high field MRI. PloS One 7, e32645. https://doi.org/10.1371/journal.pone.0032645.

Cirone, J., Rosahl, T.W., Reynolds, D.S., Newman, R.J., O'meara, G.F., Hutson, P.H., Wafford, K.A., 2004. γ-aminobutyric acid type a receptor β2 subunit mediates the hypothermic effect of etomidate in mice. Anesthesiology 100, 1438–1445. https://anesthesiology.pubs.asahq.org/article.aspx?articleid=1942784.

Clauset, A., Newman, M.E., Moore, C., 2004. Finding community structure in very large networks. Phys. Rev. 70, 066111 https://doi.org/10.1103/PhysRevE.70.066111.

Cohen, E.R., Ugurbil, K., Kim, S.-G., 2002. Effect of basal conditions on the magnitude and dynamics of the blood oxygenation level-dependent fMRI response. J. Cerebr. Blood Flow Metabol. 22, 1042–1053. https://doi.org/10.1097/00004647-200209000-00002.

Csardi, G., Nepusz, T., 2006. The Igraph Software Package for Complex Network Research, InterJournal Complex Systems, p. 1695. http://igraph.org.

De Wildt, D., Hillen, F., Rauws, A., Sangster, B., 1983. Etomidate-anaesthesia, with and without fentanyl, compared with urethane-anaesthesia in the rat. Br. J. Pharmacol. 79, 461–469. https://doi.org/10.1111/j.1476-5381.1983.tb11019.x.

Devor, A., Tian, P., Nishimura, N., Teng, I.C., Hillman, E.M., Narayanan, S., Ulbert, I., Boas, D.A., Kleinfeld, D., Dale, A.M., 2007. Suppressed neuronal activity and concurrent arteriolar vasoconstriction may explain negative blood oxygenation level-dependent signal. J. Neurosci. 27, 4452–4459. https://doi.org/10.1523/JNEUROSCI.0134-07.2007.

Drew, P.J., Shih, A.Y., Kleinfeld, D., 2011. Fluctuating and sensory-induced vasodynamics in rodent cortex extend arteriole capacity. Proc. Natl. Acad. Sci. U.S.A. 108, 8473–8478. https://doi.org/10.1073/pnas.1100428108.

D'Souza, D.V., Jonckers, E., Bruns, A., Künnecke, B., von Kienlin, M., Van der Linden, A., Mueggler, T., Verhoye, M., 2014. Preserved modular network organization in the sedated rat brain. PloS One 9, e106156. https://doi.org/10.1371/journal.pone.0106156.

Franceschini, M.A., Radhakrishnan, H., Thakur, K., Wu, W., Ruvinskaya, S., Carp, S., Boas, D.A., 2010. The effect of different anesthetics on neurovascular coupling. Neuroimage 51, 1367–1377. https://doi.org/10.1016/j.neuroimage.2010.03.060.

Ganjoo, P., Farber, N.E., Hudetz, A., Smith, J.J., Samso, E., Kampine, J.P., Schmeling, W.T., 1998. In vivo effects of dexmedetomidine on laser-Doppler flow and pial arteriolar diameter. Anesthesiology 88, 429–439. https://doi.org/10.1097/00000542-199802000-00022.

Gass, N., Schwarz, A.J., Sartorius, A., Schenker, E., Risterucci, C., Spedding, M., Zheng, L., Meyer-Lindenberg, A., Weber-Fahr, W., 2014. Sub-anesthetic ketamine modulates intrinsic BOLD connectivity within the hippocampal-prefrontal circuit in the rat. Neuropsychopharmacology 39, 895. https://doi.org/10.1038/npp.2013.290.

Golanov, E.V., Yamamoto, S., Reis, D.J., 1994. Spontaneous waves of cerebral blood flow associated with a pattern of electrocortical activity. Am. J. Physiol. Regul. Integr. Comp. Physiol. 266, R204–R214. https://doi.org/10.1038/npp.2013.290.

Gorgolewski, K., Burns, C., Madison, C.e. a., Nipype, 2011. A flexible, lightweight and extensible neuroimaging data processing framework in python. Front. Neuroinf. 5–13. https://doi.org/10.3389/fninf.2011.00013.

Grandjean, J., Schroeter, A., Batata, I., Rudin, M., 2014. Optimization of anesthesia protocol for resting-state fMRI in mice based on differential effects of anesthetics on functional connectivity patterns. Neuroimage 102, 838–847. https://doi.org/10.1016/j.neuroimage.2014.08.043.

Grandjean, J., Canella, C., Anckaerts, C., Ayrancı, G., Bougacha, S., Bienert, T., Buehlmann, D., Coletta, L., Gallino, D., Gass, N., et al., 2020. Common functional networks in the mouse brain revealed by multi-centre resting-state fMRI analysis. Neuroimage 205, 116278. https://doi.org/10.1016/j.neuroimage.2019.116278.

Greicius, M.D., Krasnow, B., Reiss, A.L., Menon, V., 2003. Functional connectivity in the resting brain: a network analysis of the default mode hypothesis. Proc. Natl. Acad. Sci. U.S.A. 100, 253–258. https://doi.org/10.1073/pnas.0135058100. arXiv. http://www.pnas.org/content/100/1/253.full.pdf.

Guilfoyle, D.N., Gerum, S.V., Sanchez, J.L., Balla, A., Sershen, H., Javitt, D.C., Hoptman, M.J., 2013. Functional connectivity fMRI in mouse brain at 7 T using isoflurane. J. Neurosci. Methods 214, 144–148. https://doi.org/10.1016/j.jneumeth.2013.01.019.

Hendrich, K.S., Kochanek, P.M., Melick, J.A., Schiding, J.K., Statler, K.D., Williams, D.S., Marion, D.W., Ho, C., 2001. Cerebral perfusion during anesthesia with fentanyl, isoflurane, or pentobarbital in normal rats studied by arterial spin-labeled MRI. Magn. Reson. Med. 46, 202–206. https://doi.org/10.1002/mrm.1178.

Hirschler, L., Debacker, C.S., Voiron, J., Köhler, S., Warnking, J.M., Barbier, E.L., 2018. Interpulse phase corrections for unbalanced pseudo-continuous arterial spin labeling at high magnetic field. Magn. Reson. Med. 79, 1314–1324. https://doi.org/10.1002/mrm.26767.

Hoffman, W.E., Edelman, G., Kochs, E., Werner, C., Segil, L., Albrecht, R.F., 1991. Cerebral autoregulation in awake versus isoflurane-anesthetized rats. Anesth. Analg. 73, 753–757. https://doi.org/10.1213/00000539-199112000-00013.

Hudetz, A.G., Roman, R.J., Harder, D.R., 1992. Spontaneous flow oscillations in the cerebral cortex during acute changes in mean arterial pressure. J. Cerebr. Blood Flow Metabol. 12, 491–499. https://doi.org/10.1038/jcbfm.1992.67.

Hutchison, R.M., Hutchison, M., Manning, K.Y., Menon, R.S., Everling, S., 2014. Isoflurane induces dose-dependent alterations in the cortical connectivity profiles and dynamic properties of the brain's functional architecture. Hum. Brain Mapp. 35, 5754–5775. https://doi.org/10.1002/hbm.22583.

Jann, K., Gee, D.G., Kilroy, E., Schwab, S., Smith, R.X., Cannon, T.D., Wang, D.J., 2015. Functional connectivity in BOLD and CBF data: similarity and reliability of resting brain networks. Neuroimage 106, 111–122. https://doi.org/10.1016/j.neuroimage.2014.11.028.

Jonckers, E., Van Audekerke, J., De Visscher, G., Van der Linden, A., Verhoye, M., 2011. Functional connectivity fMRI of the rodent brain: comparison of functional connectivity networks in rat and mouse. PloS One 6, e18876. https://doi.org/10.1371/journal.pone.0018876.

Jonckers, E., Delgado y Palacios, R., Shah, D., Guglielmetti, C., Verhoye, M., Linden, A., 2014. Different anesthesia regimes modulate the functional connectivity outcome in mice. Magn. Reson. Med. 72, 1103–1112. https://doi.org/10.1002/mrm.24990.

Kalthoff, D., Seehafer, J.U., Po, C., Wiedermann, D., Hoehn, M., 2011. Functional connectivity in the rat at 11.7 T: Impact of physiological noise in resting state fMRI. Neuroimage 54, 2828–2839. https://doi.org/10.1002/nbm.1815.

Kalthoff, D., Po, C., Wiedermann, D., Hoehn, M., 2013. Reliability and spatial specificity of rat brain sensorimotor functional connectivity networks are superior under sedation compared with general anesthesia. NMR Biomed. 26, 638–650. https://doi.org/10.1002/nbm.2908.

Kilkenny, C., Browne, W.J., Cuthill, I.C., Emerson, M., Altman, D.G., 2010. Improving bioscience research reporting: the ARRIVE guidelines for reporting animal research. PLoS Biol. 8, 1–5. https://doi.org/10.1371/journal.pbio.1000412.

King, J.A., Garelick, T.S., Brevard, M.E., Chen, W., Messenger, T.L., Duong, T.Q., Ferris, C.F., 2005. Procedure for minimizing stress for fMRI studies in conscious rats. J. Neurosci. Methods 148, 154–160. https://doi.org/10.1016/j.jneumeth.2005.04.011.

Liang, X., Zou, Q., He, Y., Yang, Y., 2013. Coupling of functional connectivity and regional cerebral blood flow reveals a physiological basis for network hubs of the human brain. Proc. Natl. Acad. Sci. U.S.A. 110, 1929–1934. https://doi.org/10.1073/pnas.1214900110.

Liang, Z., Li, T., King, J., Zhang, N., 2013. Mapping thalamocortical networks in rat brain using resting-state functional connectivity. Neuroimage 83, 237–244. https://doi.org/10.1371/journal.pone.0032766.

Liang, Z., Liu, X., Zhang, N., 2015. Dynamic resting state functional connectivity in awake and anesthetized rodents. Neuroimage 104, 89–99. https://doi.org/10.1016/j.neuroimage.2014.10.013.

Liska, A., Galbusera, A., Schwarz, A.J., Gozzi, A., 2015. Functional connectivity hubs of the mouse brain. Neuroimage 115, 281–291. https://doi.org/10.1016/j.neuroimage.2015.04.033.

Liu, X., Li, R., Yang, Z., Hudetz, A.G., Li, S.-J., 2012. Differential effect of isoflurane, medetomidine, and urethane on bold responses to acute levo-tetrahydropalmatine in the rat. Magn. Reson. Med. 68, 552–559. https://doi.org/10.1002/mrm.23243.

Liu, X., Zhu, X.-H., Zhang, Y., Chen, W., 2013. The change of functional connectivity specificity in rats under various anesthesia levels and its neural origin. Brain Topogr. 26, 363–377. https://doi.org/10.1007/s10548-012-0267-5.

Liu, X., Pillay, S., Li, R., Vizuete, J.A., Pechman, K.R., Schmainda, K.M., Hudetz, A.G., 2013. Multiphasic modification of intrinsic functional connectivity of the rat brain during increasing levels of propofol. Neuroimage 83, 581–592. https://doi.org/10.1016/j.neuroimage.2013.07.003.

Lu, H., Zuo, Y., Gu, H., Waltz, J.A., Zhan, W., Scholl, C.A., Rea, W., Yang, Y., Stein, E.A., 2007. Synchronized delta oscillations correlate with the resting-state functional MRI signal. Proc. Natl. Acad. Sci. U.S.A. 104, 18265–18269. https://doi.org/10.1073/pnas.0705791104.

Lu, H., Zou, Q., Gu, H., Raichle, M.E., Stein, E.A., Yang, Y., 2012. Rat brains also have a default mode network. Proc. Natl. Acad. Sci. U.S.A. 109, 3979–3984. https://doi.org/10.1073/pnas.1200506109.

Lv, H., Wang, Z., Tong, E., Williams, L.M., Zaharchuk, G., Zeineh, M., Goldstein-Piekarski, A.N., Ball, T.M., Liao, C., Wintermark, M., 2018. Resting-state functional MRI: everything that nonexperts have always wanted to know. Am. J. Neuroradiol. 39, 1390–1399. https://doi.org/10.3174/ajnr.A5527.

Ma, Z., Perez, P., Ma, Z., Liu, Y., Hamilton, C., Liang, Z., Zhang, N., 2016. Functional atlas of the awake rat brain: a neuroimaging study of rat brain specialization and integration. Neuroimage 170, 95–112. https://doi.org/10.1016/j.neuroimage.2016.07.007.

Magnuson, M., Majeed, W., Keilholz, S.D., 2010. Functional connectivity in blood oxygenation level-dependent and cerebral blood volume-weighted resting state functional magnetic resonance imaging in the rat brain. J. Magn. Reson. Imag. 32, 584–592. https://doi.org/10.1002/jmri.22295.

Magnuson, M.E., Thompson, G.J., Pan, W.-J., Keilholz, S.D., 2014. Time-dependent effects of isoflurane and dexmedetomidine on functional connectivity, spectral characteristics, and spatial distribution of spontaneous bold fluctuations. NMR in biomedicine 27, 291–303. https://doi.org/10.1002/nbm.3062.

Markov, N.T., Ercsey-Ravasz, M., Van Essen, D.C., Knoblauch, K., Toroczkai, Z., Kennedy, H., 2013. Cortical high-density counterstream architectures. Science 342, 1238406. https://doi.org/10.1126/science.1238406.

Masamoto, K., Kanno, I., 2012. Anesthesia and the quantitative evaluation of neurovascular coupling. J. Cerebr. Blood Flow Metabol. 32, 1233–1247. https://doi.org/10.1038/jcbfm.2012.50.

Masamoto, K., Fukuda, M., Vazquez, A., Kim, S.-G., 2009. Dose-dependent effect of isoflurane on neurovascular coupling in rat cerebral cortex. Eur. J. Neurosci. 30, 242–250. https://doi.org/10.1111/j.1460-9568.2009.06812.x.

Mateo, C., Knutsen, P.M., Tsai, P.S., Shih, A.Y., Kleinfeld, D., 2017. Entrainment of arteriole vasomotor fluctuations by neural activity is a basis of blood-oxygenation-level-dependent "resting-state" connectivity. Neuron 96, 936–948. https://doi.org/10.1016/j.neuron.2017.10.012.

Maximilian, V.A., Prohovnik, I., Risberg, J., 1980. Cerebral hemodynamic response to mental activation in normo-and hypercapnia. Stroke 11, 342–347. https://www.ahajournals.org/doi/pdf/10.1161/01.str.11.4.342.

Mechling, A.E., Hübner, N.S., Lee, H.-L., Hennig, J., von Elverfeldt, D., Harsan, L.-A., 2014. Fine-grained mapping of mouse brain functional connectivity with resting-state fMRI. Neuroimage 96, 203–215. https://doi.org/10.1016/j.neuroimage.2014.03.078.

Murphy, K., Fox, M.D., 2017. Towards a consensus regarding global signal regression for resting state functional connectivity MRI. Neuroimage 154, 169–173. https://doi.org/10.1016/j.neuroimage.2016.11.052.

Nasrallah, F.A., Tay, H.-C., Chuang, K.-H., 2014. Detection of functional connectivity in the resting mouse brain. Neuroimage 86, 417–424. https://doi.org/10.1016/j.neuroimage.2013.10.025.

Ogawa, S., Lee, T.M., Kay, A.R., Tank, D.W., 1990. Brain magnetic resonance imaging with contrast dependent on blood oxygenation. Proc. Natl. Acad. Sci. U.S.A. 87, 9868–9872. https://doi.org/10.1073/pnas.87.24.9868.

Oh, S.W., Harris, J.A., Ng, L., Winslow, B., Cain, N., Mihalas, S., Wang, Q., Lau, C., Kuan, L., Henry, A.M., et al., 2014. A mesoscale connectome of the mouse brain. Nature 508, 207. https://doi.org/10.1038/nature13186.

Otte, W.M., van der Marel, K., Braun, K.P., Dijkhuizen, R.M., 2014. Effects of transient unilateral functional brain disruption on global neural network status in rats: a methods paper. Front. Syst. Neurosci. 8, 40. https://doi.org/10.3389/fnsys.2014.00040.

Paasonen, J., Stenroos, P., Salo, R.A., Kiviniemi, V., Gröhn, O., 2018. Functional connectivity under six anesthesia protocols and the awake condition in rat brain. Neuroimage 172, 9–20. https://doi.org/10.1016/j.neuroimage.2018.01.014.

Pan, W.-J., Thompson, G.J., Magnuson, M.E., Jaeger, D., Keilholz, S., 2013. Infraslow LFP correlates to resting-state fMRI BOLD signals. Neuroimage 74, 288–297. https://doi.org/10.1016/j.neuroimage.2013.02.035.

Papp, E.A., Leergaard, T.B., Calabrese, E., Johnson, G.A., Bjaalie, J.G., 2014. Waxholm space atlas of the Sprague Dawley rat brain. Neuroimage 97, 374–386. https://doi.org/10.1016/j.neuroimage.2014.04.001.

Paus, T., 2001. Primate anterior cingulate cortex: where motor control, drive and cognition interface. Nat. Rev. Neurosci. 2, 417–424. https://doi.org/10.1038/35077500.

Pawela, C.P., Biswal, B.B., Cho, Y.R., Kao, D.S., Li, R., Jones, S.R., Schulte, M.L., Matloub, H.S., Hudetz, A.G., Hyde, J.S., 2008. Resting-state functional connectivity of the rat brain. Magn. Reson. Med. 59, 1021–1029. https://doi.org/10.1002/mrm.21524.

Pawela, C.P., Biswal, B.B., Hudetz, A.G., Schulte, M.L., Li, R., Jones, S.R., Cho, Y.R., Matloub, H.S., Hyde, J.S., 2009. A protocol for use of medetomidine anesthesia in rats for extended studies using task-induced BOLD contrast and resting-state functional connectivity. Neuroimage 46, 1137–1147. https://doi.org/10.1016/j.neuroimage.2009.03.004.

Petrinovic, M.M., Hankov, G., Schroeter, A., Bruns, A., Rudin, M., von Kienlin, M., Künnecke, B., Mueggler, T., 2016. A novel anesthesia regime enables neurofunctional studies and imaging genetics across mouse strains. Sci. Rep. 6, 2045–2322. https://doi.org/10.1038/srep24523.

Power, J.D., Barnes, K.A., Snyder, A.Z., Schlaggar, B.L., Petersen, S.E., 2012. Spurious but systematic correlations in functional connectivity MRI networks arise from subject motion. Neuroimage 59, 2142–2154. https://doi.org/10.1016/j.neuroimage.2011.10.018.

Ribeiro de Paula, D., Ziegler, E., Abeyasinghe, P.M., Das, T.K., Cavaliere, C., Aiello, M., Heine, L., Di Perri, C., Demertzi, A., Noirhomme, Q., et al., 2017. A Method for Independent Component Graph Analysis of Resting-State Fmri, Brain and Behavior 7, e00626. https://onlinelibrary.wiley.com/doi/pdf/10.1002/brb3.626.

Rolland, M., Carcenac, C., Overton, P., Savasta, M., Coizet, V., 2013. Enhanced visual responses in the superior colliculus and subthalamic nucleus in an animal model of Parkinson's disease. Neuroscience 252, 277–288. https://doi.org/10.1016/j.neuroscience.2013.07.047.

Rubinov, M., Sporns, O., 2010. Complex network measures of brain connectivity: uses and interpretations. Neuroimage 52, 1059–1069. https://doi.org/10.1016/j.neuroimage.2009.10.003.

Schlegel, F., Schroeter, A., Rudin, M., 2015. The hemodynamic response to somatosensory stimulation in mice depends on the anesthetic used: implications on analysis of mouse fMRI data. Neuroimage 116, 40–49. https://doi.org/10.1016/j.neuroimage.2015.05.013.

Schroeter, A., Schlegel, F., Seuwen, A., Grandjean, J., Rudin, M., 2014. Specificity of stimulus-evoked fMRI responses in the mouse: the influence of systemic physiological changes associated with innocuous stimulation under four different anesthetics. Neuroimage 94, 372–384. https://doi.org/10.1016/j.neuroimage.2014.01.046.

Schwarz, A.J., Gass, N., Sartorius, A., Zheng, L., Spedding, M., Schenker, E., Risterucci, C., Meyer-Lindenberg, A., Weber-Fahr, W., 2013. The low-frequency blood oxygenation level-dependent functional connectivity signature of the hippocampal–prefrontal network in the rat brain. Neuroscience 228, 243–258. https://doi.org/10.1016/j.neuroscience.2012.10.032.

Sforazzini, F., Schwarz, A.J., Galbusera, A., Bifone, A., Gozzi, A., 2014. Distributed BOLD and CBV-weighted resting-state networks in the mouse brain. Neuroimage 87, 403–415. https://doi.org/10.1016/j.neuroimage.2013.09.050.

Shim, W.H., Baek, K., Kim, J.K., Chae, Y., Suh, J.-Y., Rosen, B.R., Jeong, J., Kim, Y.R., 2012. Frequency distribution of causal connectivity in rat sensorimotor network: resting-state fMRI analyses. J. Neurophysiol. 109, 238–248. https://doi.org/10.1152/jn.00332.2012.

Sicard, K., Shen, Q., Brevard, M.E., Sullivan, R., Ferris, C.F., King, J.A., Duong, T.Q., 2003. Regional cerebral blood flow and BOLD responses in conscious and anesthetized rats under basal and hypercapnic conditions: implications for functional MRI studies. J. Cerebr. Blood Flow Metabol. 23, 472–481. https://doi.org/10.1097/01.WCB.0000054755.93668.20.

Sinclair, M.D., 2003. A review of the physiological effects of α2-agonists related to the clinical use of medetomidine in small animal practice. Can. Vet. J. 44, 885. https://www.ncbi.nlm.nih.gov/pmc/articles/PMC385445/.

Sloan, H., Austin, V., Blamire, A., Schnupp, J.W., Lowe, A.S., Allers, K., Matthews, P.M., Sibson, N.R., 2010. Regional differences in neurovascular coupling in rat brain as determined by fMRI and electrophysiology. Neuroimage 53, 399–411. https://doi.org/10.1016/j.neuroimage.2010.07.014.

Smith, J.B., Liang, Z., Watson, G.D., Alloway, K.D., Zhang, N., 2017. Interhemispheric resting-state functional connectivity of the claustrum in the awake and anesthetized states. Brain Struct. Funct. 222, 2041–2058. https://doi.org/10.1007/s00429-016-1323-9.

Stafford, J.M., Jarrett, B.R., Miranda-Dominguez, O., Mills, B.D., Cain, N., Mihalas, S., Lahvis, G.P., Lattal, K.M., Mitchell, S.H., David, S.V., et al., 2014. Large-scale topology and the default mode network in the mouse connectome. Proc. Natl. Acad. Sci. U.S.A. 111, 18745–18750. https://doi.org/10.1073/pnas.1404346111.

Thompson, G.J., Pan, W.-J., Billings, J.C., Grooms, J.K., Shakil, S., Jaeger, D., Keilholz, S.D., 2014. Phase-amplitude coupling and infraslow (< 1 hz) frequencies in the rat brain: relationship to resting state fMRI. Front. Integr. Neurosci. 8, 41. https://doi.org/10.3389/fnint.2014.00041.

Valdes Hernandez, P.A., Sumiyoshi, A., Nonaka, H., Haga, R., Aubert Vasquez, E., Ogawa, T., Iturria Medina, Y., Riera, J.J., Kawashima, R., 2011. An in vivo MRI template set for morphometry, tissue segmentation, and fMRI localization in rats. Front. Neuroinf. 5, 26. https://doi.org/10.3389/fninf.2011.00026.

Vogt, B.A., 2005. Pain and emotion interactions in subregions of the cingulate gyrus. Nat. Rev. Neurosci. 6, 533–544. https://doi.org/10.1038/nrn1704.

Vogt, B.A., Miller, M.W., 1983. Cortical connections between rat cingulate cortex and visual, motor, and postsubicular cortices. J. Comp. Neurol. 216, 192–210. https://doi.org/10.1002/cne.902160207.

Wang, K., van Meer, M.P., van der Marel, K., van der Toorn, A., Xu, L., Liu, Y., Viergever, M.A., Jiang, T., Dijkhuizen, R.M., 2011. Temporal scaling properties and spatial synchronization of spontaneous blood oxygenation level-dependent (bold) signal fluctuations in rat sensorimotor network at different levels of isoflurane anesthesia. NMR Biomed. 24, 61–67. https://doi.org/10.1002/nbm.1556.

Wang, H.E., Bénar, C.G., Quilichini, P.P., Friston, K.J., Jirsa, V.K., Bernard, C., 2014. A systematic framework for functional connectivity measures. Front. Neurosci. 8, 405. https://doi.org/10.3389/fnins.2014.00405.

Weber, R., Ramos-Cabrer, P., Wiedermann, D., van Camp, N., Hoehn, M., 2006. A fully noninvasive and robust experimental protocol for longitudinal fMRI studies in the rat. Neuroimage 29, 1303–1310. https://doi.org/10.1016/j.neuroimage.2005.08.028.

Whitcher, B.J., 1998. Assessing Nonstationary Time Series Using Wavelets. Citeseer. http://citeseerx.ist.psu.edu/viewdoc/download?doi=10.1.1.29.5644&rep=rep1&type=pdf.

Whitcher, B., Guttorp, P., Percival, D.B., 2000. Wavelet analysis of covariance with application to atmospheric time series. J. Geophys. Res.: Atmosphere 105, 14941–14962. https://doi.org/10.1029/2000JD900110.

Williams, K.A., Magnuson, M., Majeed, W., LaConte, S.M., Peltier, S.J., Hu, X., Keilholz, S.D., 2010. Comparison of α-chloralose, medetomidine and isoflurane

anesthesia for functional connectivity mapping in the rat. Magn. Reson. Imaging 28, 995–1003. https://doi.org/10.1016/j.mri.2010.03.007.

Yan, C.-G., Cheung, B., Kelly, C., Colcombe, S., Craddock, R.C., Di Martino, A., Li, Q., Zuo, X.-N., Castellanos, F.X., Milham, M.P., 2013. A comprehensive assessment of regional variation in the impact of head micromovements on functional connectomics. Neuroimage 76, 183–201. https://doi.org/10.1016/j.neuroimage.2013.03.004.

Zalesky, A., Fornito, A., Bullmore, E., 2012. On the use of correlation as a measure of network connectivity. Neuroimage 60, 2096–2106. https://doi.org/10.1016/j.neuroimage.2012.02.001.

Zerbi, V., Grandjean, J., Rudin, M., Wenderoth, N., 2015. Mapping the mouse brain with rs-fMRI: an optimized pipeline for functional network identification. Neuroimage 123, 11–21. https://doi.org/10.1016/j.neuroimage.2015.07.090.

Zhang, N., Rane, P., Huang, W., Liang, Z., Kennedy, D., Frazier, J.A., King, J., 2010. Mapping resting-state brain networks in conscious animals. J. Neurosci. Methods 189, 186–196. https://doi.org/10.1016/j.jneumeth.2010.04.001.

Zhurakovskaya, E., Leikas, J., Pirttimäki, T., Mon, F.C., Gynther, M., Aliev, R., Rantamäki, T., Tanila, H., Forsberg, M.M., Gröhn, O., et al., 2019. Sleep-state dependent alterations in brain functional connectivity under urethane anesthesia in a rat model of early-stage Parkinson's disease. eNeuro 6. https://doi.org/10.1523/ENEURO.0456-18.2019.